

DEPARTMENT OF PHYSICS  
UNIVERSITY OF JYVÄSKYLÄ  
RESEARCH REPORT No. 10/2001

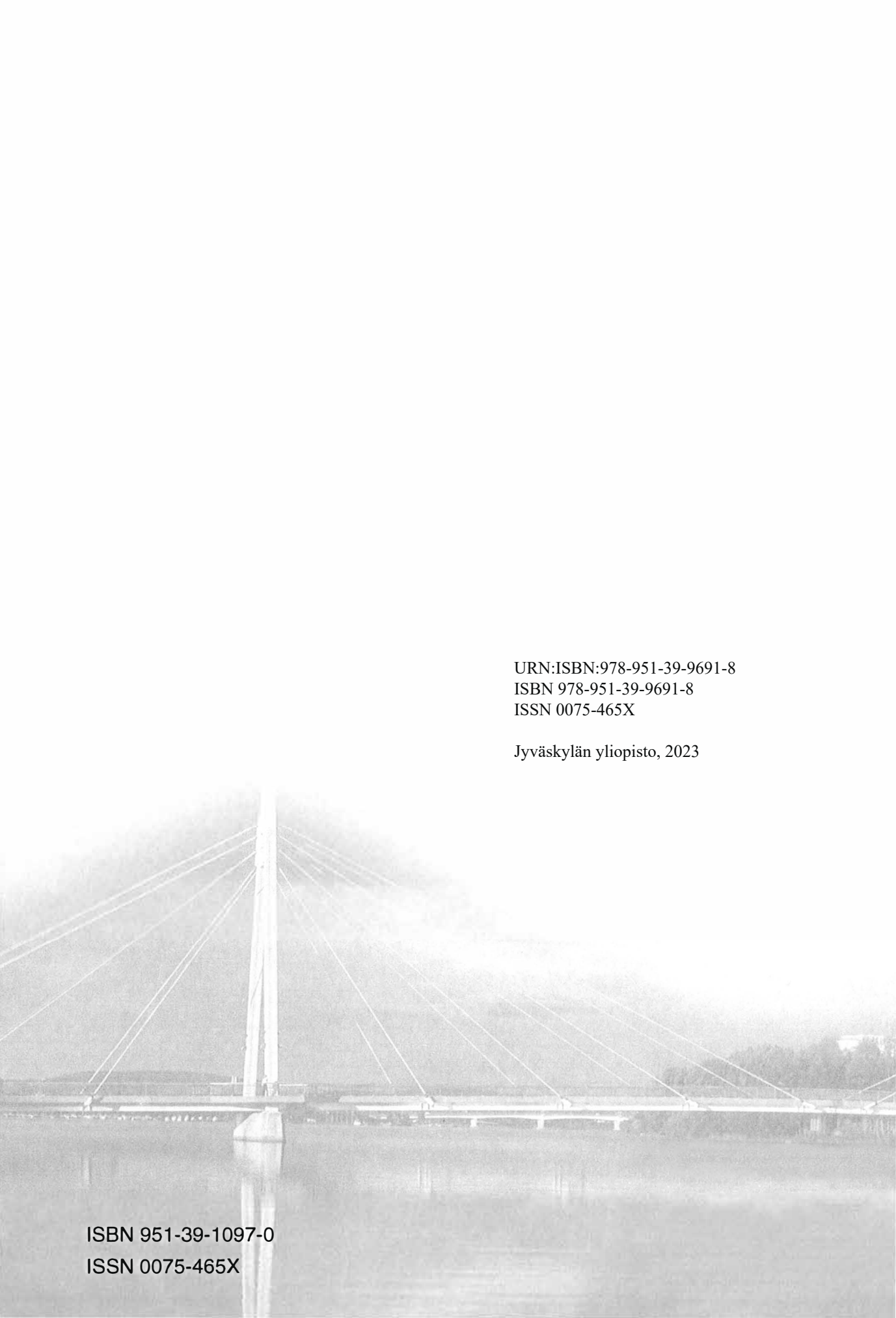
# PRODUCTION AND SPECTROSCOPY OF VERY NEUTRON-RICH NUCLEI

BY  
ZORAN RADIVOJEVIC

Academic Dissertation  
for the Degree of  
Doctor of Philosophy



Jyväskylä, Finland  
November 2001



URN:ISBN:978-951-39-9691-8  
ISBN 978-951-39-9691-8  
ISSN 0075-465X

Jyväskylän yliopisto, 2023

ISBN 951-39-1097-0

ISSN 0075-465X

DEPARTMENT OF PHYSICS,  
UNIVERSITY OF JYVÄSKYLÄ  
RESEARCH REPORT No. 10/2001

**PRODUCTION AND SPECTROSCOPY OF  
VERY NEUTRON-RICH NUCLEI**

**BY  
ZORAN RADIVOJEVIC**

Academic Dissertation  
for the Degree of  
Doctor of Philosophy

*To be presented, by permission of the  
Faculty of Mathematics and Natural Sciences  
of the University of Jyväskylä,  
for public examination in Auditorium FYS-1 of the  
University of Jyväskylä on November 16, 2001  
at 12 o'clock noon*



Jyväskylä, Finland  
November 2001

## Contents

<b>1. Introduction</b>	6
<b>2. Production and spectroscopy of n-rich nuclei</b>	8
2.1 Fast neutron induced fission	10
2.2 Significance of neutron spectroscopy	12
2.3 Neutron detection techniques	17
<b>3. Design and construction of the spectroscopic set-up</b>	19
3.1 Triggering detectors for <i>TOF</i> measurements	19
3.2 Position Sensitive Neutron Detector	24
3.3 Low-threshold neutron detector array	31
3.4 $^6\text{Li}$ -glass detector for low-energy neutrons	33
3.5 Small NE213 detector for noise minimisation	35
<b>4. Monte-Carlo simulations of neutron detector properties</b>	36
4.1 Simulation of neutron interaction with scintillators	36
4.2 Nuclear data base as input for the EFEN simulation	40
4.3 Modelling and sampling	42
4.4 Results of EFEN simulations	45
4.5 Threshold, efficiency and energy resolution evaluations	55
<b>5. Experimental arrangements</b>	59
5.1 HENDES	59
5.2 Set-up for neutron yield measurements	63
5.3 IGISOL	65
5.4 Set-up for beta-delayed neutron spectroscopy	67
5.5 On-line calibration with well-known neutron sources $^{94,95}\text{Rb}$	68
5.6 Data acquisition system	74
<b>6. Experimental results</b>	76
6.1 Neutron yields from thick targets and fast-neutron induce fission of $^{238}\text{U}$	76
6.1.1 Neutron energy spectra and yield	77
6.1.2 Mass distribution and yield in fast-neutron induced fission of $^{238}\text{U}$	83
6.1.3 Absolute cross-sections of fast neutron induced fission of $^{238}\text{U}$	86
6.2 Beta-delayed neutron decay of $^{33}\text{Na}$	89
6.2.1 Half-life of $^{33}\text{Na}$	91
6.2.2 Determination of $P_n$ value	94
6.2.3 Beta delayed neutron energy spectra	95
6.2.4 Triple coincidence analysis	97
6.2.5 Level of accidentals at low neutron counting rates	100
<b>7. High-efficient systems and further improvements</b>	102
<b>8. Conclusions</b>	106
Appendix 1	111
Appendix 2	113
Appendix 3	116
<b>References</b>	122



## **Preface**

The work reviewed in this thesis has been carried out during the years 1997-2001 at the Department of Physics in the University of Jyväskylä.

First of all, I want to thank my supervisor Dr. Wladyslaw Trzaska for his efficient and persistent guidance, and Prof. Juha Äystö for his irreplaceable assistance in all turns of this work. All the members of our research groups are warmly acknowledged for extremely pleasant collaboration. I wish to express my gratitude to the staff of the Accelerator Laboratory at Department of Physics for good and co-operative atmosphere.

Finally, I want to thank my friends for inspiration and challenging atmosphere throughout my studies. I wish to express my thanks to my wife Vesna and my son Oggy for their patience and encouraging.

Jyväskylä, November 2001.

Zoran Radivojevic

A part of the results in this work has been reported also in the following publications:

- [1] ***Neutron yields from thick  $^{12}\text{C}$  and  $^9\text{Be}$  targets irradiated by 50 and 65 MeV deuterons***  
Z. Radivojevic, A. Honkanen, J. Äystö, V. Lyapin, V. Rubchenya, W.H. Trzaska, D. Vakhtin, and G. Walter, Nucl. Inst. and Meth. B 183 (2001) 212-220  
[https://doi.org/10.1016/S0168-583X\(01\)00729-7](https://doi.org/10.1016/S0168-583X(01)00729-7)
- [2] ***Beta-delayed neutron decay of  $^{33}\text{Na}$***   
Z. Radivojevic, P. Baumann, E. Caurier, J. Cederkäll, S. Courtin, Ph. Dessagne, A. Jokinen, A. Knipper, G. Le Scornet, V. Lyapin, Ch. Miehé, F. Nowacki, , M. Oinonen, E. Poirier, M. Ramdhane, W. H. Trzaska, G. Walter, J. Äystö and the ISOLDE collaboration, Nucl. Inst. and Meth. A (2001), #41158.  
[https://doi.org/10.1016/S0168-9002\(01\)01347-X](https://doi.org/10.1016/S0168-9002(01)01347-X)
- [3] ***Neutron yields from thick  $^{13}\text{C}$  target irradiated by 30 MeV protons***  
Z. Radivojevic, F. Brandolini, P. Dendooven, V. Lyapin, L. Stroe, L. Tecchio, W.H. Trzaska and D. Vakhtin, Nucl Inst. and Meth. A (2001), submitted.  
[https://doi.org/10.1016/S0168-583X\(02\)00696-1](https://doi.org/10.1016/S0168-583X(02)00696-1)
- [4] ***Production of neutron-rich isotopes in fission of uranium induced by neutrons of 20 MeV average energy***  
G. Lhersonneau, Dendooven ,G.Canchel, J.Huikari, P. Jardin, A. Jokinen , V.Kolhinen , C.Lau , L. Lebreton , A.C. Mueller, A. Nieminen, S. Nummela, H. Penttila , K.Peräjärvi, Z. Radivojevic, V. Rubchenya, M.-G. Saint-Laurent, W.H. Trzaska, D. Vakhtin, J. Vervier, A.C.C. Villari, J.C. Wang and J. Äystö, Eur. Phys. J. A 9, 385-396 (2000).  
<https://doi.org/10.1007/s100500070023>
- [5] ***Intruder features in the island of inversion: The  $^{33}\text{Mg}$  case***  
S. Nummela, F. Nowacki, P. Baumann, E. Caurier, J. Cederkäll, S. Courtin, Ph. Dessagne, A. Jokinen, A. Knipper, G. Le Scornet, V. Lyapin, Ch. Miehé, M. Oinonen, E. Poirier, Z. Radivojevic, M. Ramdhane, W.H. Trzaska, G. Walter, J. Äystö and the ISOLDE collaboration., Phys. Rev. C 64 (2001) 054313  
<https://doi.org/10.1103/PhysRevC.64.054313>
- [6] ***Beta-delayed neutron spectroscopy by the TOF technique at IGISOL:  $^{94,95}\text{Rb}$  as test case***  
Z. Radivojevic, P. Dendooven, V. Lyapin, S. Nummela, A. Jokinen, W.H. Trzaska, G. Walter and J. Äystö, Proceedings of the 3rd International Conference on Exotic Nuclei and Atomic Masses (ENAM2001), Hämeenlinna, 2001, edited by J. Äystö et al., (Springer-Verlag, Heidelberg, to be published)  
[https://doi.org/10.1007/978-3-642-55560-2\\_133](https://doi.org/10.1007/978-3-642-55560-2_133)

- [7] ***Neutron and fragment yields in proton-induced fission of  $^{238}\text{U}$  at intermediate energy***  
 V.A. Rubchenya, W.H. Trzaska, D.N. Vakhtin, J. Äystö, P. Dendooven, S. Honkanen, A. Jokinen, Z. Radivojevic, J.C. Wang, I.D. Alkhozov, A. Evsenin, S.V. Khlebnikov, A.V. Kuznetsov, V.G. Lyapin, I.O. Osetrov, G. P. Tiourin, A.A. Alexandrov, Yu.E. Penionzkievich, Nucl. Inst. and Meth. A (2001) 653-662.  
[https://doi.org/10.1016/S0168-9002\(01\)00176-0](https://doi.org/10.1016/S0168-9002(01)00176-0)
- [8] ***Position-sensitive neutron detector***  
 A.V. Kuznetsov, D.N. Vakhtin, Z. Radivojevic, I.D. Alkhozov, V.G. Lyapin, W. H. Trzaska, Nucl. Inst. and Meth. A (2001), 16565.  
[https://doi.org/10.1016/S0168-9002\(01\)01833-2](https://doi.org/10.1016/S0168-9002(01)01833-2)
- [9] ***Fragment mass distribution in superasymmetric region in proton-induced fission of U & Th***  
 W.H. Trzaska, V.A. Rubchenya, D.N. Vakhtin, I.D. Alkhozov, A. Evsenin, S.V. Khlebnikov, A.V. Kuznetsov, V.G. Lyapin, Z. Radivojevic, G.P. Turin and J. Äystö, Nuvo Cimento 1998., Vol 11 A, No, 8-9, P. 1055.  
<https://doi.org/10.1007/BF03035992>
- [10] ***Particle emission as a probe for dynamics of fission of heated nuclei***  
 W.H. Trzaska, J. Äystö, Z. Radivojevic, V.A. Rubchenya, D.N. Vakhtin, I.D. Alkhozov, A. Evsenin, S.V. Khlebnikov, A.V. Kuznetsov, V.G. Lyapin, G.P. Turin, I.O. Osetrov, A.A. Alexandrov, Yu.E. Penionzkievich, Yu.V. Pyatkov, Yu.G. Sobolev, M. Mutterer, J. von Kalben, K. Brinkmann. Acta Physica Slovaca 1999. vol. 49, No. 1, p. 987  
<https://www.researchgate.net/publication/228605818>
- [11] ***Current research at HENDES***  
 W. H. Trzaska, V. A. Rubchenya, J. Äystö, Z. Radivojevic, D.N. Vakhtine, I.D. Alkhozov, A. Evsenin, S.V. Khlebnikov, A.V. Kuznetsov, V.G. Lyapin, O.I. Ossetrov, G.P. Tiourine, A.A. Alexadrov, Yu. E. Penionzkevich, Yu.V. Pyatkov, Yu.G. Sobolev, M. Mutterer, K. Brinkman, V. Makarenko, Nukleonika 1998., vol. 43 No. 3, p. 291.  
<https://www.researchgate.net/publication/291815985>

### **Author's contribution**

Author of this thesis has written papers 1,2,3 and 6 and participated in writing of the rest of the papers. Author has made a significant contribution in the detector design, construction and measurement in the all experiments providing basis for publication of the papers. The author provided the data analysis in papers 1,2,3,6 and made significant contribution in papers 4,5 and 8.

The detector properties have been investigated by extensive measurements and Monte-Carlo simulations, which has been developed by the author. Helpful data analysis routines and methods for this work have been written by the author.

## 1. Introduction

One of the great challenges of nuclear physics today is the use of radioactive nuclear beams (RNB), especially for the production and spectroscopy of exotic nuclei. Neutron-rich nuclei (n-rich) are less known than their neutron-deficient partners at the same distance from the valley of stability. Moreover, there are many more neutron-rich nuclei than neutron deficient ones. It has been established that n-rich beams with energies around the Coulomb barrier will provide a wealth of new opportunities in nuclear structure physics [Sie93].

The first difficulty of any experimental study in this field is low production yields of n-rich nuclei. Many products are formed with such small yields that only the simplest properties are measurable. There are several techniques to produce and select n-rich nuclei. The fragmentation technique with heavy-ion beams requires large accelerators and is thus restricted to the biggest laboratories (GSI, GANIL). Fission is a very promising mechanism to produce such beams. For example, proton induced fission has been used for many years [Rav89] at the ISOLDE facility with 1 GeV of bombarding energy and at medium proton energies at IGISOL in Jyväskylä [Äys01]. However, methods using charged particle induced reactions for the production of n-rich nuclei are limited by the heat load deposited in the target by high intensity beams. In other words, the heat load is a severe limitation for the present and future facilities where fast extraction of exotic nuclei demands well-controlled temperature of the target. Furthermore, short range of charged particles in the fissile target makes additional constraints. The short range makes limitation for the absolute amount of available centres for nuclear reactions. Consequently the total number of produced fission events is limited. One alternative to solve these problems is to use fast-neutron induced fission. Relatively high intensity neutron beams can be produced by using a beam of light charged particles converted to neutrons in thick targets. This concept was originally introduced by J. Nolen [Nol93] where the beam heat-load is shifted to the converter which is separated from the target and may easily be cooled. The optimal beam energies are less than 100 MeV and thus suitable for middle-size laboratories like the Accelerator Laboratory in Jyväskylä. These facts contributed to the interest in fast neutron induced fission as a promising driving process in the production of n-rich nuclei. In addition, there were some indications that the

distribution of fission fragments induced by fast neutrons favours the n-rich side [Kudo98] if compared with proton induced fission.

The first part of this work is devoted to fast neutron induced fission of  $^{238}\text{U}$  where precise determination of the absolute neutron yields emerging from the converters allows the determination of the absolute fission cross-section. It will be explained what makes fast neutron induced fission attractive and how it compares with other possible production mechanisms. Furthermore, a comparison with results obtained earlier with proton-induced fission as the primary reaction will be presented. It will be shown that light-particle and especially fast-neutron induced fission is a promising tool for the production of radioactive n-rich nuclei far from stability.

The second difficulty in the study of exotic n-rich nuclei is necessity for efficient and selective detection techniques because production cross-sections of exotic neutron-rich nuclei are generally low and detector techniques have to be very efficient and sophisticated. It is certain that a very large number of unexplored n-rich isotopes exist, but we still lack experimental tools for producing and observing them all. Alpha particle spectroscopy has been successfully used for selection and identification of super-heavy elements. An important reason for success was relatively high detection efficiency for alpha particles. Gamma ray spectroscopy is often considered the most selective detection technique. However, as the production and selection techniques of exotic nuclei are not always sufficiently selective, high background conditions may hamper  $\gamma$ -ray spectroscopy. When fission is the primary reaction for the production of n-rich nuclei, the reaction cross-sections are higher for nuclei relatively close to the line of stability. As a result of this beta-gated gamma spectroscopy suffers from the background generated by other short-lived nuclei. Neutron detection has been used for selection of the most exotic nuclei. New techniques developed within the last few years promise that we will be able to approach problems that offer some qualitatively new features. Neutron spectroscopy has given many new physics results of peculiar properties of n-rich nuclei such as beta-delayed emission of one, two or more neutrons. Studies of n-rich nuclei began with measuring their gross properties;  $\beta$ -decay half life  $T_{1/2}$  and delayed neutron-emission probability  $P_n$  being the easiest measurable quantities. Later measurements of energy spectra of neutrons emitted from excited states fed in  $\beta$ -decay were successful providing new information about the structure of the nuclide and details of

the decay process. In this work neutron spectroscopy has been applied to the study of  $^{33}\text{Na}$  (light) and  $^{95}\text{Rb}$  (heavy) n-rich nuclei. Neutron energy spectra were measured (but also  $P_n$  and  $T_{1/2}$ ) allowing precise determination of the energy level scheme of the daughter nuclei ( $^{33}\text{Mg}$ ). The spectroscopy of beta delayed neutrons yielded new spectroscopic information. Also, these experiments helped understanding how improve our detection techniques in case of small yields and low count rates. In the case of heavier n-rich nuclei ( $^{95}\text{Rb}$ ) where the level density parameter is relatively high, neutron spectroscopy demands excellent energy resolution as well as high detection efficiency at low energies (1 keV–2 MeV). In these conditions our primary goal was to test the use of the time-of-flight (*TOF*) technique for beta-delayed neutron spectroscopy of mass separated isobars.

All of these facts underline the need for further improvements in neutron spectroscopy which provides a powerful and promising tool to study n-rich nuclei. Therefore this work suggests further improvements in high-resolution neutron spectroscopy. Precise description of the all used neutron detectors has been obtained not only experimentally but also by new Monte-Carlo simulation programme especially developed for the work described in this thesis.

This work deals with both production and spectroscopy of exotic phenomena by using neutrons. It combines spectroscopy of fission-fragments, light-particles and  $\gamma$ -rays in experiments performed at HENDES and IGISOL in Jyväskylä and also at ISOLDE-CERN facilities.

## 2. Production and spectroscopy of n-rich nuclei

Several basic methods for production of RNB are schematically shown in Fig. 1. In Flight Separation (IFS) uses fragmentation as a primary reaction where identification of every reaction product is made during its flight prior to  $\beta$ -decay. Thanks to the high initial momentum of the beam, fragments leave the target with high velocity, and their velocity spectrum can be measured [Sch00]. There is no limitation due to chemical properties and lifetimes can be as short as micro seconds. However, the target thickness is limited by the acceptance of the magnetic spectrometer applied, since the momentum spread of the fragments increases with the target thickness.

Isotopic Separation On-Line (ISOL) technique uses fission and spallation of a heavy target such as uranium. The ISOL approach has the advantage of employing thick targets, so isotopes with very low formation cross-sections can be produced. The products of a nuclear reaction formed in the target (kept at high well-controlled temperature to emphasize diffusion) are continuously transferred to the ion source then extracted by a high-voltage in order to be mass-analysed by means of a magnet.

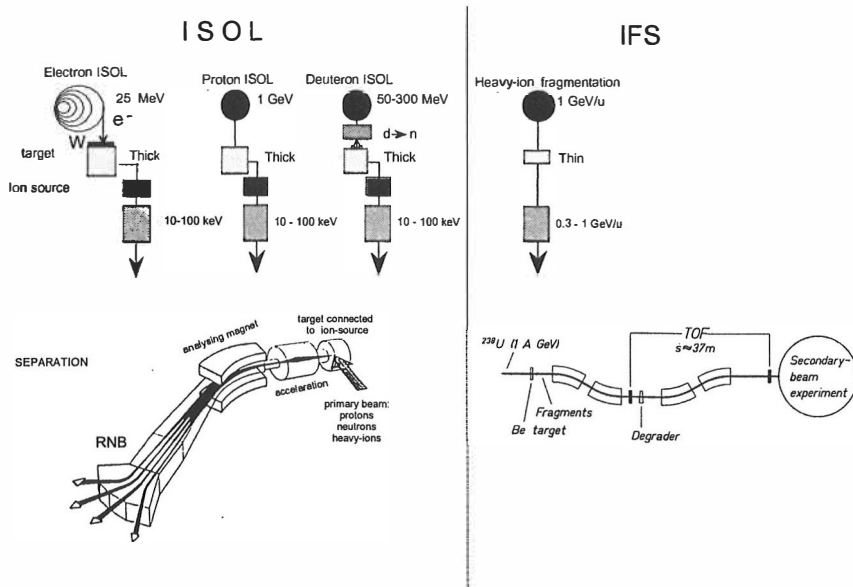


Figure 1. Basic techniques for the production and extraction of exotic beams. The two figures at the bottom represent principles of separation. The conversion of the nuclear reaction products into mono-isotopic ion beams is provided by means of electromagnetic mass-separation.

As mentioned both techniques use primary charged particles causing severe limitations due to a huge power load directly deposited in the production target. To solve this problem two alternatives are depicted in Fig. 1. The first one uses a strong flux of  $\gamma$ -rays and photo-fission reaction [Dub99]. The  $\gamma$ -rays are created by intensive ( $\sim 20 \mu\text{A}$ ) electron beam which produces bremsstrahlung. The yield of  $^{238}\text{U}$  fission is determined by the absorption of  $\gamma$ -rays by a  $^{238}\text{U}$  nucleus in the region of the giant dipole resonance located at energy of 13.5 MeV. The second alternative is to use fast neutrons produced in a converter target, which allows that the primary beam load is shifted to the converter and production target is activated only by neutrons.

To explore and elaborate the idea of fast-neutron induced fission a series of measurements [1,3,4] at several facilities has been performed. The first mass-yield measurements were carried out for various neutron energies by taking advantage of (d,pf) reaction at the HENDES facility. There the neutron yield from several thick light targets ( $^{12,13}\text{C}$ ,  $^9\text{Be}$ ) was precisely measured to optimize combination of targets, projectiles and bombarding energies. Several sets of neutron detectors were used to perform precise absolute measurements. Finally, Z-distributions for mass selected ions by IGISOL were obtained. The combination of these data subsequently yields cross-sections for individual nuclides.

## 2.1 Fast neutron induced fission

The intensity of radioactive beam  $I$  is given by the product of the formation cross-section  $\sigma_f$ , the primary-beam intensity  $\Phi$ , the target-area density  $n_t$ , the production release and transfer efficiency  $\varepsilon_1$ , the ion-source efficiency  $\varepsilon_2$  and the delay-transfer efficiency  $\varepsilon_3$  due to radioactive decay losses during the process.

$$I = \sigma_f \Phi n_t \varepsilon_1 \varepsilon_2 \varepsilon_3. \quad (1)$$

The formation cross-section  $\sigma_f$  is clearly a crucial parameter. Therefore, the present work concentrates on determination of absolute cross-sections for fission products induced by fast neutrons. This type of reaction is favoured for studying due to several reasons. As mentioned previously power dissipation is a serious limitation for present and future facilities. Furthermore, while there are numerous studies with protons, fast-neutron induced fission data are very scarce. More precisely, total fission cross-sections are well-known (see Fig. 2) but fission products mass and charge distributions are scarce. The concept for production of n-rich nuclei by fast neutrons is illustrated in Fig. 3. Energetic neutrons are generated by interaction of a deuteron beam with a thick target, the so-called converter, in which deuterons are eventually stopped. Natural uranium target, placed close to the converter in the forward direction, is exposed to the high-flux of fast neutrons, as shown in Fig. 3. Fission products are further extracted and selected by the ISOL technique. In contrast to using



neutrons as secondary particles the method has several advantages. A separation of converter and target allows the converter to be cooled and thus to be able to stand very high primary beam intensities. Efficient cooling is also safety factor.

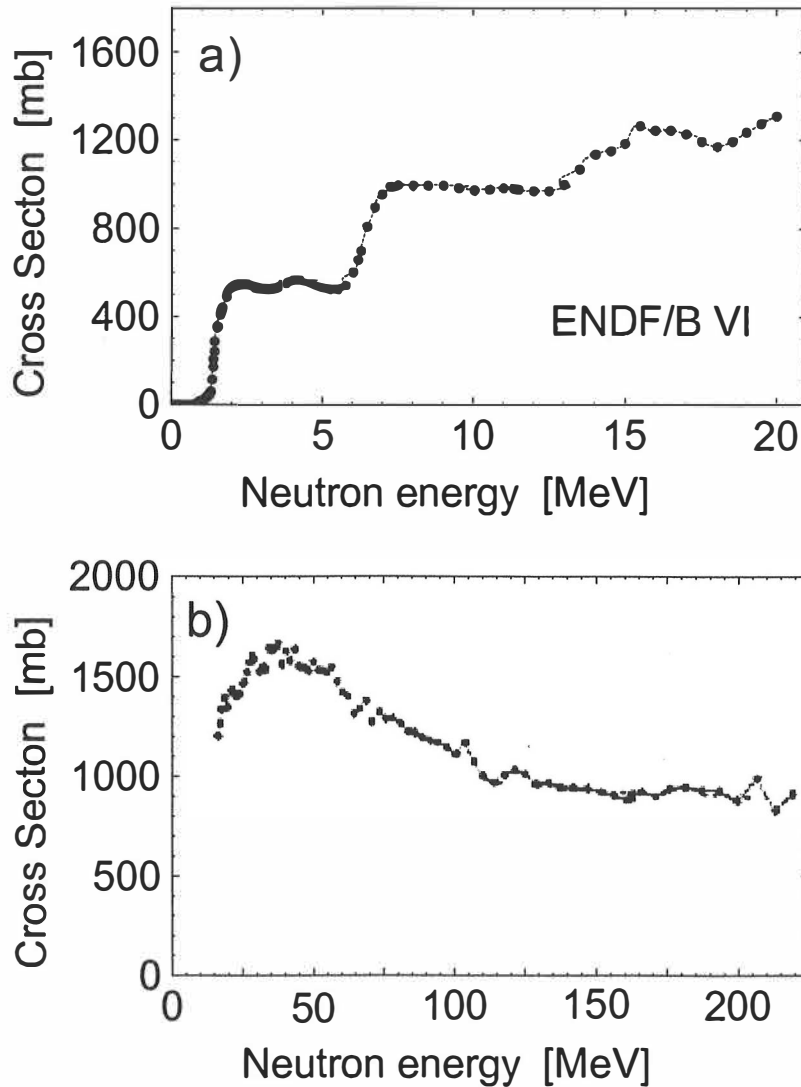


Figure 2. (a) Total cross sections for neutron induced fission of  $^{238}\text{U}$  as reported in ENDF/B VI data library and (b) in ref. [Lis91].

As far as extraction time is not prohibitive, the uranium target size can be made very large to benefit from the high penetrating power of neutrons.

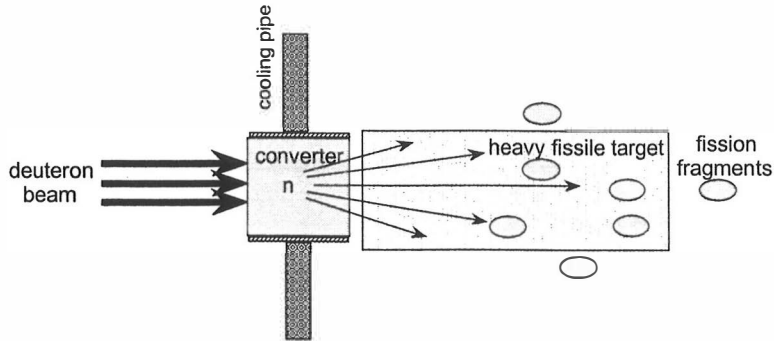


Figure 3. A schematic presentation of production of exotic nuclei via fast neutron induced fission of heavy uranium target.

## 2.2 Significance of neutron spectroscopy

As mentioned earlier several experiments have been carried out to characterize the neutron field emerging from thick targets. The crucial point in these measurements is thorough knowledge of the detector properties to allow precise determination of absolute neutron intensities. As in any absolute measurement it is very important to have crucial detector features, such as intrinsic efficiency and detection threshold, well determined. Therefore, I have put an effort for precise evaluation of the n-detector properties by extensive measurements and Monte-Carlo numerical simulations. Optimisation of the n-detector energy resolution and the ability to detect low-energy neutrons are important for precise determination of the peak-to-valley ( $P/V$ ) ratio in fission fragment mass distribution. It is well known that the  $P/V$  ratio is very sensitive even to a small number of low-energy neutrons, which may drastically change the shape of the mass distribution of fission fragments.

In the second part of this work neutron spectroscopy was applied to characterisation of n-rich nuclei. Since the probability of neutron emission tends to increase with the neutron number, neutron spectroscopy has an important role in the investigation and

search for the most exotic n-rich nuclei. For that reason neutron spectroscopy was applied to the study of  $^{33}\text{Na}$  and  $^{95}\text{Rb}$  n-rich nuclei. They were produced in fission of  $^{238}\text{U}$  either at high-energy (ISOLDE-CERN) or low-energy (IGISOL-Jyvaskylä). The aim of the study of  $\beta$ -delayed neutrons from  $^{33}\text{Na}$ , is to identify discrete structures in nuclear spectra and draw conclusions about their meaning for nuclear physics. In other words it provides information about structure of the nuclide and details of the decay process. For this determination both partial neutron emission probabilities  $P_n^f$  to different final states and corresponding neutron energies  $E_n$  are required.

$\beta$ -delayed neutron emission becomes competitive to  $\gamma$ -decay and occurs when isobaric mass difference ( $Q_\beta$ ) becomes larger than one neutron binding energy ( $S_{1n}$ ). The process takes place in two steps. In the case of  $^{33}\text{Na}$  the precursor nuclide first decays by beta emission to states above the neutron binding energy of the daughter, and the neutron is subsequently emitted in competition with gamma rays.

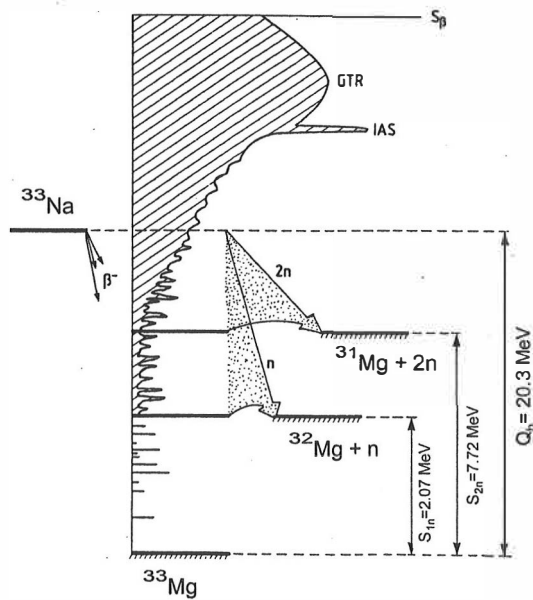


Figure 4. One and two beta-delayed neutron emission scheme for  $\beta$ -delayed neutron decay of  $^{33}\text{Na}$ . The illustration is only schematical and detailed description can be found in ref. [5].

$\beta$ -delayed neutron emission probability ( $P_n$ ) is defined as the number of neutrons emitted per 100  $\beta$ -disintegrations.  $\beta$ -decay half-life  $T_{1/2}$  and  $\beta$ -delayed neutron emission probability  $P_n$  are the easiest measurable  $\beta$ -decay properties and often the only ones observable for n-rich nuclei far from stability and with low production yields. They contain important nuclear-structure information:  $T_{1/2}$  is sensitive to low-lying  $\beta$ -strength while  $P_n$  is proportional to the fraction of  $\beta$  feeding for levels higher than the neutron separation energy. When  $Q_\beta > S_{2n}$ ,  $\beta$ -delayed two-neutron emission may occur, as shown in Fig. 4.

In order to determine the cascade relations in the decay scheme and to determine high energy levels in the daughter ( $^{33}\text{Na} \rightarrow ^{33}\text{Mg}$ ) nuclei, beta-gamma-neutron triple coincident detection technique is necessary. The number of  $\beta$ -delayed neutrons diminishes with the beta half-life of the mother isotope ( $^{33}\text{Na}$  -precursor), and neutron emission occurs from excited states in the daughter nucleus ( $^{33}\text{Mg}$  -emitter). These processes for the decay of  $^{33}\text{Na}$  are schematically illustrated in Fig. 4. In the case of n-rich light nuclei such as  $^{33}\text{Na}$ , neutron emitting states often have an appreciable fraction of the single-particle strength and, hence, large widths, resulting in a good separation of the emitting levels. To better explain experimental conditions in the spectroscopy of  $^{33}\text{Na}$  a schematic representation of  $\beta$ -delayed neutron emission is given in Fig. 5. Beta-decay of the  $^{33}\text{Na}$  precursor to neutron-unbound states in the emitter  $^{33}\text{Mg}$  is followed by emission of a neutron and formation of the final  $^{32}\text{Mg}$  nucleus in the neighbouring isobaric chain. Moreover, neutron energy spectra provide information on the excited states in the daughter nuclei  $^{33}\text{Mg}$  populated in  $\beta$ -decay as well as in  $\beta$ -n-decay ( $^{32,31}\text{Mg}$ ). Above the neutron separation energy  $S_{1n}$ , excited states can decay by electromagnetic transitions and neutron emission, therefore the total decay width of such a level is the sum of the neutron and gamma widths [Bla79]. For neutrons this probability depends on the transmission through the potential barrier. Since a neutron possesses no charge, it does not feel any effects due to the Coulomb interaction but it is sensitive to the centrifugal barrier, which depends on the angular momentum  $l$  of the neutron.

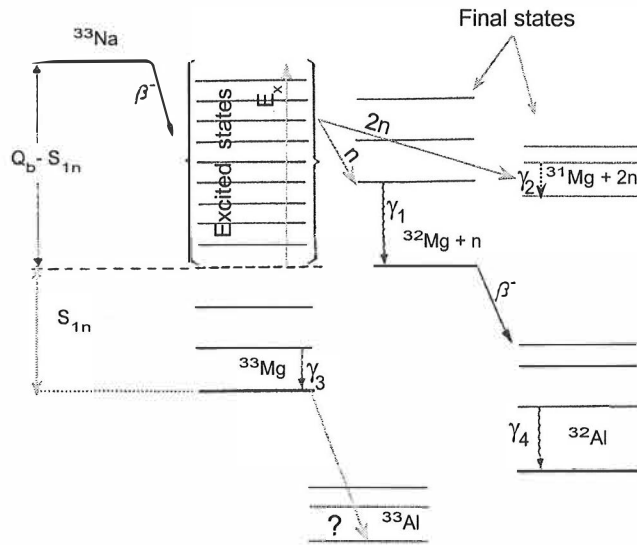


Figure 5. Principle characteristics of the  $\beta$ -delayed neutron emission process in decay of  $^{33}\text{Na}$ .

Two general experimental methods have been used so far in the determination of  $P_n$  values. The first is coincident  $\beta$  and neutron counting with well-calibrated (in efficiency and threshold) neutron and beta detectors. The second one is  $\gamma$ -ray spectroscopy of nuclei produced by fission. Beta-decay half-lives  $T_{1/2}$  and  $P_n$  values provides important structure information. However, they are integral quantities and therefore not definitive in extracting information on individual decay steps. As can be seen from Fig. 5, there are two ways to determine partial neutron branches (or  $P_n^f$ ) to individual final states:

- (I) by measuring the delayed neutrons in coincidence with  $\gamma$ -rays depopulating the excited states in the residual nucleus (triple-coincidence technique) and,
- (II) by relating the intensities of  $\gamma$ -rays originating from  $\beta$ - $n$ - $\gamma$  decay to known absolute  $\gamma$ -ray intensities of either the  $\beta$ -decay daughter of the residual nucleus or the  $\beta$ -decay daughter of the precursor.

The importance of an efficient detection of triple ( $\beta$ - $\gamma$ - $n$ ) coincidences together with the corresponding neutron energies has thus become evident.

In this work the total  $P_n$  value was obtained by  $\beta$ -neutron counting and the ratio  $P_{1n}/P_{2n}$  was extracted from characteristic gamma transitions. The experimental data reveal fine structure in experimental  $\beta$ -strength functions ( $S_\beta$ ), which has been calculated and presented in ref. [5]. For the determination of  $S_\beta$  and related functions

see Appendix 1. With experimental knowledge of the energy dependence of  $S_\beta$  and taking into account its influence on the neutron branching ratios, a detailed comparison of the measured  $P_n^f$  values and model predictions of the neutron emission process become possible.

For heavy nuclei (like  $^{95}\text{Rb}$ ) the upper part of the emitter excited states ( $E_x$ ) becomes exceedingly complex, and the states are of the same character as those studied as resonances in neutron reactions. These states are best described in the framework of the compound nucleus model treated in Hauser-Feshbach formalism [Gad92]. However, in the case of the  $^{95}\text{Rb}$  typical excitation energies of the emitter states are 4 to 10 MeV, implying that the spacing between levels of the same spin and parity at the top of the spectrum will be of the order of 1 eV to 1 keV only! Experience shows that the wave function of such states is very complex, and that the amplitudes for the individual configurations can best be described as random on a local scale. An additional complication in neutron emission experiments is relatively modest energy resolution and sensitivity. For this reason it is important to remember that individual states will be missed experimentally and that the spectra will, in most cases, contain unresolved parts. These physical phenomena emphasize the importance of having a high-resolution n-detection system, which may resolve and distinguish between different neutron emitting levels, as much as possible. Therefore, in the case of  $^{95}\text{Rb}$ , our primary goal was testing of time-of-flight technique for  $\beta$ -delayed neutron spectroscopy of mass separated isobars at the IGISOL facility. Besides testing of the *TOF* method additional analysis was performed to examine interconnection between partial neutron branches and the shape of the beta-strength function  $S_\beta(E)$  as a function of excitation energy ( $E_x$ ) in the emitter nucleus  $^{95}\text{Sr}$  (or neutron energy when corrected for the  $S_n$  and nucleus recoil energy). In the calculations I have used the algorithm and programs developed and described in detail in ref. [Pop99]. The input for the program is the measured  $\beta$ -delayed neutron energy spectrum, which also contains a data-base of the energy levels and the branching ratios in the decay of emitting nucleus  $^{95}\text{Sr}$ . The results are compared with measurements carried out using high-resolution  $^3\text{He}$  chambers [Kra81].

### 2.3 Neutron detection techniques

A neutron detection system necessary for characterisation of n-rich nuclei has to combine and optimize many aspects. The system has to be very efficient because of generally low production yields of exotic nuclei. In other words, sufficient statistics can only be obtained in long-term measurements, which demand a stable detection system with a low-level of accidental coincidences. Studies of beta-delayed neutron emitters require measurement of neutron spectra from almost thermal energies up to MeV range with the ability to resolve individual final states populated by neutron emission. The narrow spacing of n-emitting levels imposes high demands on the energy resolution of neutron detectors. Experiments along this line are additionally difficult because of short half-lives of delayed neutron precursors, which generally require fast detecting systems. As mentioned ( $\beta$ - $\gamma$ -n) triple coincidence technique is a very useful way for measuring partial neutron probabilities  $P_n^f$  in coincidence with characteristic gamma lines. However, total efficiency is generally modest and depends on the product of beta, gamma and neutron detection efficiencies. This constrains the space around observation point reserved for a possible array of accompanied Ge (cluster) detectors, which means that n-detection system has to be compact and relatively small in size.

$^3\text{He}$  tubes in combination with a neutron thermalizer have a high efficiency and allow determination of  $P_n$  values. Basically, there is no low-energy threshold for  $^3\text{He}$  counters (because of use of  $^3\text{He}(n,p)\text{T}$  reaction, see Fig. 15) but generally these are slow devices (response time  $\sim\mu\text{s}$ ) causing a high-level of accidentals and in some cases suffering from thermal-neutron background. On the other hand, gridded  $^3\text{He}$  filled proportional chambers, which are devices with the highest resolution [Fra77], have very low efficiency due to use of  $^3\text{He}$  in gaseous phase and low number of interaction centres per unit of active volume. Usually new (unexplored) n-rich nuclei are produced in such small amounts that  $^3\text{He}$  proportional chambers are not able to match low-statistical conditions.

Scintillators are faster (response time  $\sim\text{ns}$ ) and allow beta delayed neutron-gamma coincidences for time-of-flight (n-TOF) measurements from which neutron energies are deduced. A relatively efficient system, which covers low as well as high neutron energies, might be obtained by a combination of several different kinds of

scintillators. For example combination of proton recoil and  ${}^6\text{Li}$ -glass scintillators stands for a good candidate to cover energy ranges from 1 keV to 10 MeV, sufficient for spectroscopy of n-rich nuclei. Furthermore, the system should be designed as an array of many modules to gain absolute efficiency. This configuration allows that the quality of the whole array rely on the performance of a single small module, which may have good properties. Stability and low-threshold of the array is provided by small size of the modules and high granularity of the whole system. Therefore, for light n-rich nuclei ( $A\approx 30$ ) fast organic proton-recoil scintillators (NE102, NE213) were chosen in construction providing good time and, consequently, good energy resolution properties for energies down to 100 keV. Spectroscopy of heavy n-rich nuclei ( $A\approx 90$ ) requires a very high energy resolution and the ranges of neutron energies to be observed are extended to low values (1 keV–2 MeV). To access and explore the low-energy part the  ${}^6\text{Li}(n,T)\alpha$  reaction was chosen in  ${}^6\text{Li}$  enriched glass scintillator (GS20). This reaction has an almost exponential cross-section increase at lower energies (see Fig. 15) and presents a promising reaction for complementary detectors intended to operate at low neutron energies.

Experiments with exotic nuclei are often characterized by low-counting rates. This imposes high detection efficiency and low-level of accidentals in long-term measurements. On the other hand, the size of the active volume for one module is limited by asked for detector quality (light collection optics, threshold, background level etc...). An advantage of liquid proton recoil scintillators is that they give a possibility to distinguish between different types of radiation, which can be used for background minimisation. Therefore, I have designed and constructed a small liquid scintillator neutron detector and compared its features with the other detectors. This yielded information for possible construction of similar neutron-detector array in future, which is based on a liquid scintillator. The quality of the whole set-up relies on the quality of a single module and large number of modules provides high efficiency. Taking advantages of low-velocities of heavy recoils (after neutron emission) very compact spectroscopic system could be constructed because of short recoil flight-path. Coincident measurement between heavy recoil and neutrons allows time-of-flight (*r-TOF*) determination and consequently neutron spectroscopy. Microsecond time ranges of the observed *r-TOF* intervals still allow relatively good energy resolution in close detector geometry. A simple set-up was described in ref. [Pop99]



which involves ion electro-optics system for beam deceleration, fast-time devices like a micro-channel-plate for detection of recoils and a scintillator detector for neutron detection. Both described detectors are relatively simple and present fast counters neglecting angular correlations between emitted particles. This resulted in a physical limitation for the final neutron energy resolution. Therefore, I have suggested further improvements by introducing position sensitivity of both micro-channel-plate and neutron detector. Furthermore, both detectors could be triggered by a new position sensitive beta detector. In this case low voltage electro-optic system can be simplified.

### **3. Design and construction of the spectroscopic set-up**

In this chapter principal design and construction properties of the neutron detectors used at several facilities will be explained. Also, the principles of operation will be given in brief. The detectors are intended for investigation of neutron emission from different physical processes in a wide neutron energy range. To match all these necessities, a time-of-flight (*TOF*) method was employed where the stop signal is given by several kinds of neutron detectors and the start signal is provided by fast detection of beta particles or fission fragments. Besides neutron energy measurements by *TOF*, timing properties of the whole system are crucial feature in obtaining absolute beta and neutron activities. As in any of *TOF* coincident techniques efficiency and timing of the whole system directly rely on the triggering detector. Therefore, this is very important detector, which deserves special attention.

#### **3.1 Triggering detectors for *TOF* measurements**

Two different kinds of the trigger-detectors were designed and constructed in order to perform *TOF* experiments. The first one is beta-trigger detector ( $\beta$ TD), which serves as the main detector for beta-delayed neutrons, beta-gamma coincidences as well as beta singles. The second one is micro-channel-plate detector (MCPD), which serves as a main trigger for fission fragments (FF), neutrons and light charged particle (LCP) correlation measurements. High efficiency and good time resolution are the main

objectives for both of the detectors. Therefore, for the active parts I have selected materials with extremely fast driving processes. In the case of the  $\beta$ TD fastest plastic scintillator was used. In the case of MCPD small micro-channel-plates were used with high amplification power allowing the fastest possible charge to signal formation. For both systems a time diagram of the signals involved is shown in Fig. 6. In the case of  $\beta$ -decay spectroscopy the initial start signal is provided by beta decay producing a relativistic electron ( $e^-$ ) as an information carrier. Due to relativistic speed of electrons time ( $t_0$ ) to reach the surface of the  $\beta$ TD is very short ( $\sim$ ps) and negligible in respect to the full TOF range ( $t_n$ ) of observed neutrons ( $\sim$ 100 ns). This approximation is allowed by relativistic speed of the electrons, of course, but also by keeping the size of the beta detector relatively small. The velocity of FF (providing the start signal) is much lower compared to relativistic electrons produced in beta-decay. For example, the heavy FF has a mean velocity of 1.3 ns/cm which means about 4 ns is needed to reach the surface of the MCPD. Therefore, the  $t_0$  is not negligible in the case of FF correlation measurements (see Fig. 6) and it is necessary to correct the detectable variables ( $t_{f1}, t_{f2}$ ). The same consideration is valid for the light charged particles and neutrons where appropriate corrections have to be applied ( $t_4 = t_n + t_c$ ).

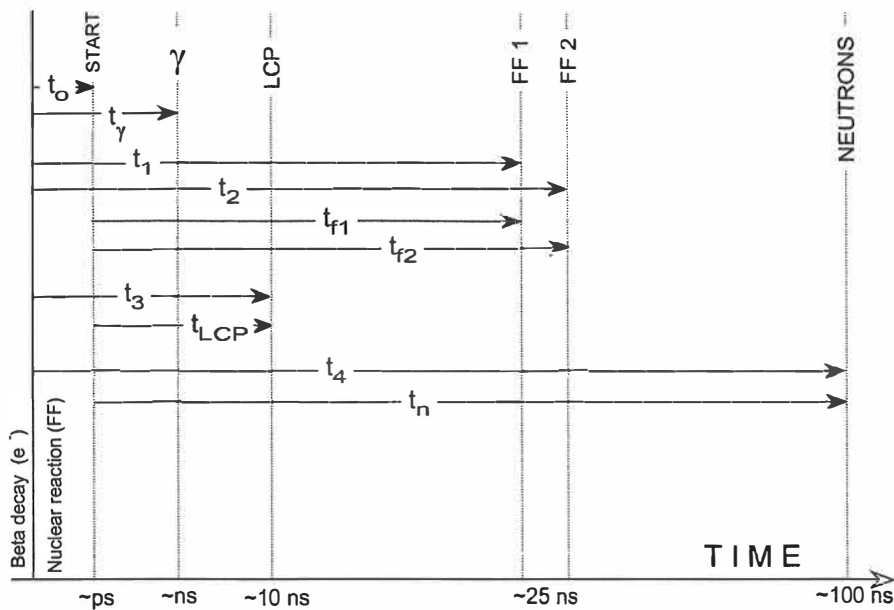


Figure 6. Definition and connection between different TOF variables observed in correlation measurements. The time scale is in order of magnitudes for illustration purposes.

I have designed and constructed the beta-trigger detector in accordance with experimental conditions for beta-delayed spectroscopy of mass separated nuclei. The active part of the  $\beta$ TD is BC408 plastic scintillator cylinder (3 cm in diameter and 5 cm high). Schematic and technical drawings are presented in Fig. 7(a,b). For excellent timing the scintillator is optically coupled to the middle of a Hamamatsu R1828-01 fast PM. Only the central part (3 cm in diameter) of the PM's photo-cathode (5 cm in full size) is used to minimise the influence of the photo-cathode borders and to emphasize amplification uniformity and finally time resolution. A diameter of 3 cm was chosen as a compromise of the necessity to having the moving tape-system in the detector (see Fig. 7a) as well as a minimal diameter to allow close position of the HPGe detectors to the beam collection point (to gain efficiency). The wall-thickness is kept to 2 mm to minimise detection of accompanied  $\gamma$ -rays and emphasize detection of electrons. Optical coupling was provided by a cylindrical light guide (plexy) and a soft silicon optical pad (hand-made), which serves as a soft 98% transparent opto-mechanical interface.

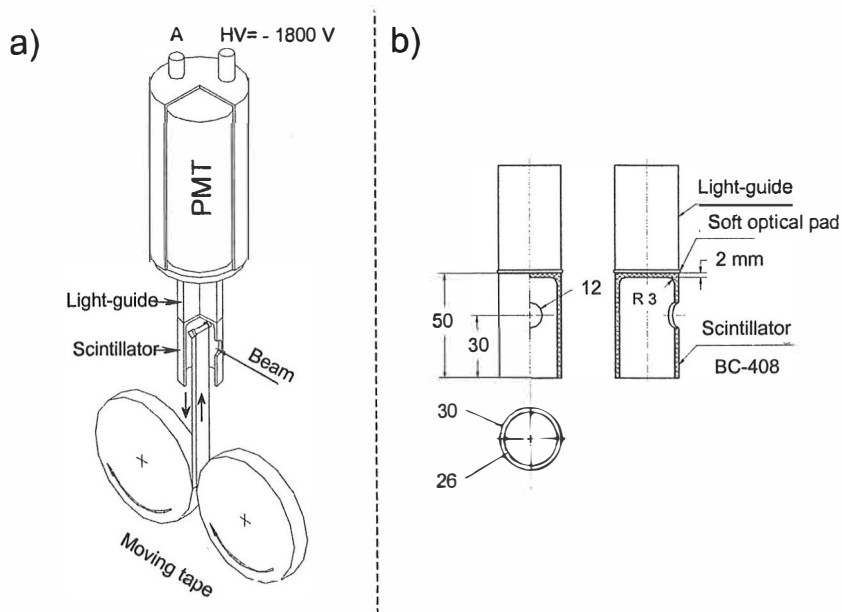


Figure 7. Beta trigger detector assemblies. (a) Active parts of the detector and (b) the scintillator cylinder with plexy-light guide.

Special effort has been given to polishing of the scintillator and light guide surfaces to supply good light collection and low-detection threshold. Smooth interconnection

between the cylinder walls and the top surface improved light-collection and efficiency (see Fig. 7b). All the  $\beta$ TD components are placed in a stainless steel frame with several windows (not shown in Fig. 7). One is for the beam entrance, the second one for the moving tape and three windows are for HpGe detectors covered by thin havar foil to minimise absorption of  $\gamma$ -rays. Finally, I made the  $\beta$ TD with a time resolution of 450 ps and the total efficiency of 64% for detection of electrons.

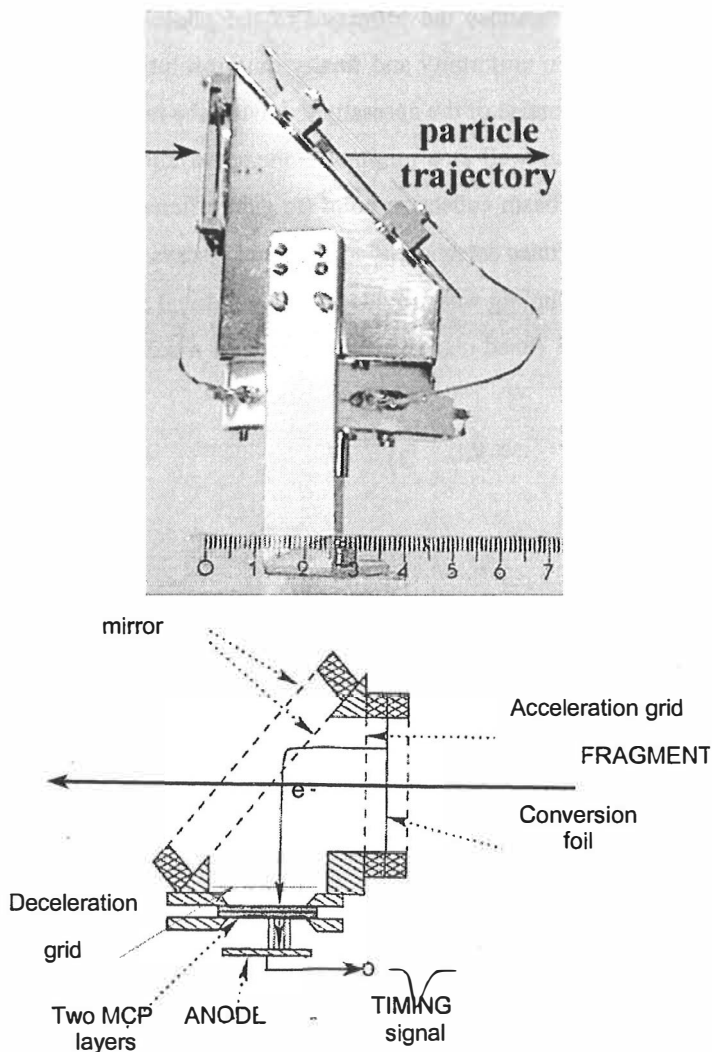


Figure 8. Top: Photograph of the Micro-Channel-Plate trigger detector. Bottom: schematic drawing of operation.

For spectroscopy of neutrons and LCP accompanied with fission-fragments several micro channel plate detectors (MCPD) have been developed and constructed. There

detectors serve as main trigger detectors at HENDES facility. The essential design features of the MCPD is to provide minimal distortion of the FF velocity vector and provide good time determination of the initial fission process. The detector consists of two layers of the micro-channel-plates (Philips, G12-36ST/15/A), an electro-optics system and a (30-100  $\mu\text{g}/\text{cm}^2$ ) thin foil, which serves for conversion of heavy ions (or FF) to electrons.

The trajectories of the electrons produced by the FF are bent on the electrostatic mirror and after deceleration guided to the first layer of the micro-channel-plate as shown in Fig. 8(b). On the back-side of the second micro-channel-plate there is an anode collecting the amplified charge.

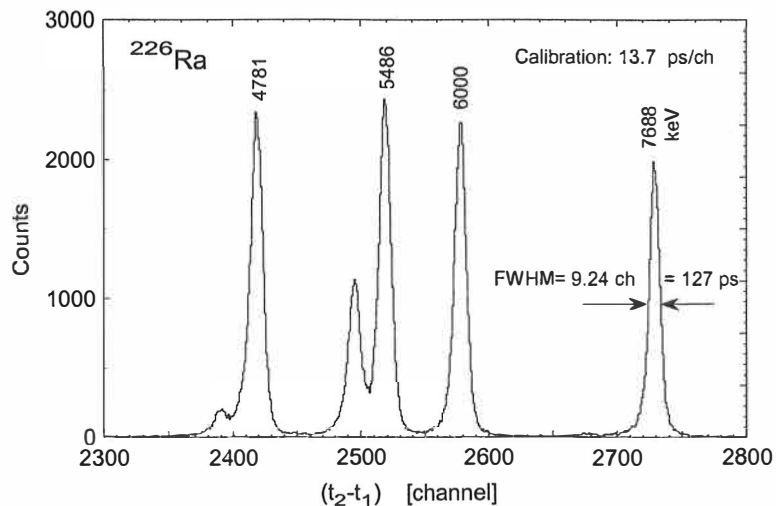


Figure 9. Time-of-flight spectrum of the alpha particles from  $^{226}\text{Ra}$  source measured by the two micro-channel-plate detectors.

The set of two micro-channel-plate layers provides a very fast amplification process with an overall amplification of about  $10^6$ . Usually the MCPD is placed at about 2-3 cm from the radiation source covering a solid angle of 15% of  $4\pi$ . In Fig. 9 there is shown a *TOF* spectrum which represents timing characteristic of the constructed MCPD detectors. This is obtained by measuring the time interval of an  $\alpha$ -particle ( $^{226}\text{Ra}$  source) passing between two identical MCPD. The inverse triggering method (inverse scale) was used to minimise the singles count rate. The standard deviation ( $\sigma_m = 55$  ps) of the peak obtained for the most energetic  $\alpha$ -particles (at 7.688 MeV) illustrates the timing properties of the MCPD detector.

### 3.2 Position Sensitive Neutron Detector

The Position Sensitive Neutron detector (PSND) stands as the main component of the HENDES multidetector array. HENDES consists of a set of fission-fragment detectors, light charged particle (LCP) detectors assembled in and around a reaction chamber and several modules of the PSNDs, which surround the spherical interaction chamber as shown in Fig. 10(a). The HENDES multidetector array has been designed to accommodate up to 48 PSNDs [Trz95] although owing to the position sensitivity of each module, successful experiments have been made with a few modules only.

There are two types of PSND; a small one and about four times larger (LANCER-PSND). The LANCER contains about 10 liters of NE213 scintillator in a rectangular quartz container (10×10×100 cm long) as shown in Fig. 10(c). Both ends of the detector are viewed by Philips XP2041 photo-multiplier. The LANCER detector has a higher detection threshold. However, its intrinsic efficiency is almost two times higher than for the small PSND. Usually the LANCER is placed at forward directions (see Fig. 10(a)) where more energetic neutrons are expected to be detected.

Five small PSND were very recently redesigned and improved (see Fig. 10(c)). Improvements have been made by using a new scintillator, new fast photo-multipliers and a new system of opto-mechanical coupling. This upgrade yielded better position and energy resolutions as well as a lower detection threshold.

The size and the length of the active part of a neutron detector are limited by detector quality demands. Many physical processes are involved and one limitation is the light attenuation by reflections and by absorption in the scintillator itself. The attenuation is proportional to the number of reflections and the length of flight paths giving rise to position dependent light collection.

Furthermore, variation of uniformity of light collection along the scintillator causes position dependence of the total integrated signals ( $E_T$ ) important for quality of n- $\gamma$  separation. Also, position and time resolution depend on uniformity of light collection. Non-uniform light collection additionally introduces a dependence of the detector efficiency and detection threshold on position along the PSND. Nevertheless, the light output should be maximised to ensure good time and position resolution and to allow a low energy threshold leading to high neutron efficiency. The light collection efficiency depends on quality of the interconnection surfaces in contact

with the scintillator. In the case of the liquid scintillator different container materials with different reflection properties, geometries and construction techniques have different light collection performances.

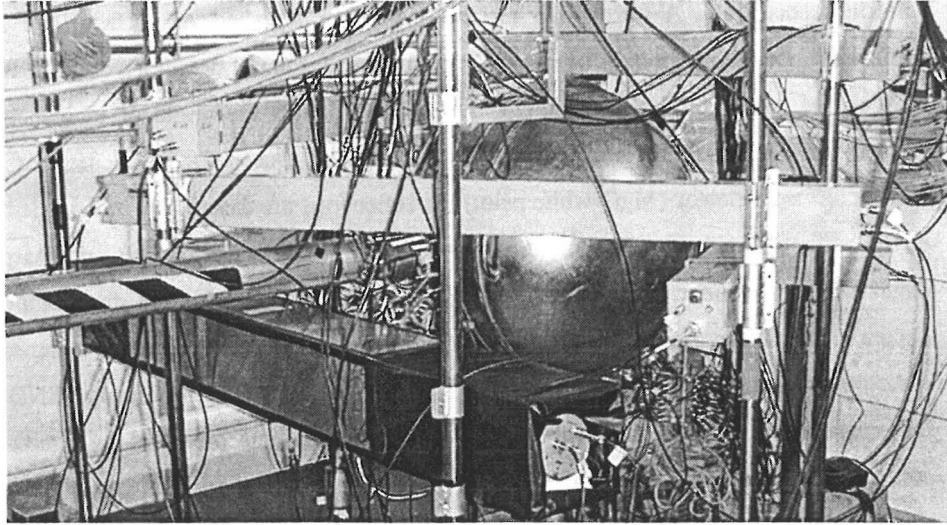
Generally speaking there are several types of reflectors used in combination with scintillator detectors. A mirror-like surface (Al-foil or polished Al surface) and a diffuse surface are commonly used reflectors suitable for small detector volumes. In the case of mirror reflector the angle of reflection equals the angle of incidence. Aluminium containers are easy to handle and commonly used for small detectors. With a diffuse reflector (MgO-white paint) the reflections are essentially independent of the angle of incidence. This fact helps the light to avoid corner effects and sharp edges of the container. On the other hand, with each reflection some degradation occurs so that this approach is not satisfactory in the case of large scintillator volumes where large number of reflections occurs, like in the case of our 1 m long PSND. Optimisation of the light collection properties in this case is provided by quartz-containers, which ensure position-independent light collection and good time resolution properties of the PSND.

The PSND is devoted mainly to investigation of neutron emission of nuclear reactions where two types of neutron sources are expected with their characteristic angular and energy distributions. This sets further requirements of the PSND performances. The first type of source is an evaporation neutron source mostly yielding smooth angular distributions with lower energy neutrons. Detection of these neutrons does not require high angular resolution but requires a large solid angle and relatively low neutron detection threshold. The second source is associated with fast moving fragments or pre-equilibrium neutron emission characterized by peaked angular distributions and higher neutron energies. To resolve these structures an angular resolution of about  $5^\circ$  and energy resolution of 10% are sufficient.

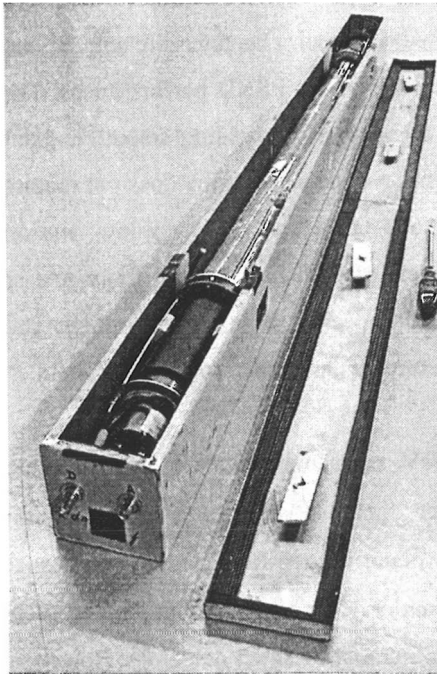
The neutrons in the energy range 1–100 MeV are usually detected with organic proton-recoil liquid scintillators because of their superior n- $\gamma$  discrimination properties. In particular the NE213 liquid scintillator is used for the PSND and usual charge-comparison method for n- $\gamma$  discrimination. The measurement of angular distributions can, of course, be performed by a number of small detectors. However, the necessity of high efficiency means a rather considerable expense (many photo-

multipliers and associated electronics etc.). Furthermore, extensive work is necessary for their calibration. These problems are reduced by a single large PSND.

a)



b)



c)

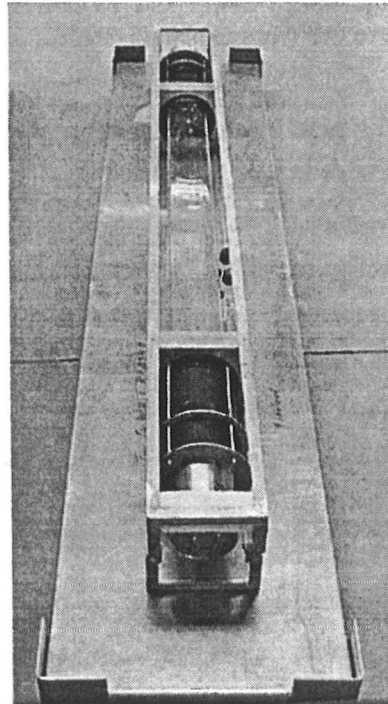


Figure 10. (a) Set of neutron detectors installed at the HENDES multidetector array. (b) A single open PSND module and (c) large LANCER-PSND.



All of these processes have been taken into account when the PSND was designed. The result is a PSND module, which consists of a  $\text{Ø}5.5 \text{ cm} \times 100 \text{ cm}$  quartz tube (cylinder wall thickness 2.5 mm) filled with liquid scintillator NE213 (about 2.3 l) viewed from both ends by PMs, and enclosed in a light-tight titanium container [Alk92]. Schematic drawings of the PSND are displayed in Fig. 11.

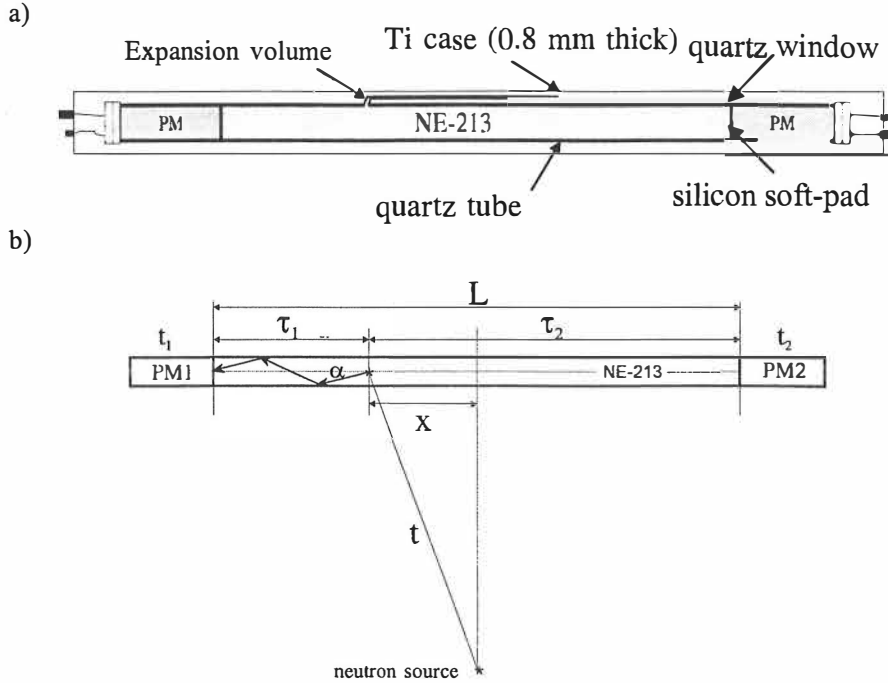


Figure 11. (a) Scheme of the PSND and light-tight titanium container. (b) Principle of time and position determination,  $X$ -position of a neutron interaction,  $t$ -time-of-flight,  $\tau_1$  and  $\tau_2$  mean light travelling times,  $\alpha$ -angle of photons relative to the PSND axis.

The construction of the holders and the expansion volume allow both horizontal and vertical mounting of the PSND. Following a principle first used by Charpak et al. [Cha62], the neutron induced scintillation is collected in the PMs at both ends. Position and time are derived from the correlated signals as depicted in Fig. 11(b). The most important signals to be generated are position  $x$  and time  $t$ . The position and time information is obtained from the difference and the sum between the mean light travelling times  $\tau_1$  and  $\tau_2$  to the two PMs as,

$$x = \frac{1}{2}(\tau_L - \tau_R) c / n_R \quad ; \quad t = \left[ \frac{1}{2}(\tau_L + \tau_R) - L / (c / n_R) \right], \quad (2)$$

where,  $c$  is the velocity of light,  $n_R$ , the refractive index of the NE213 and L-scintillator length as shown in Fig. 11(b).

In order to optimize and improve the PSND quality, I have explored the relative contribution of different sources of time uncertainty by testing several fast photomultipliers (see Table 1) attached to the same PSND. The time resolution of a *TOF* system can be determined by measuring the distribution of the time delays between prompt events. The so-called prompt spectra of two PMs (Hamamatsu R1828-01 and Philips XP2020) are shown in Fig. 12. The start and stop signals were from collimated  $\gamma$ -rays in decay of  $^{60}\text{Co}$ , detected in left and right PM coupled to the PSND, which yielded in estimation for position and time resolutions. The detector noise is minimised by applying fast coincidence between two PMs and by low dark-current features of the PMs used.

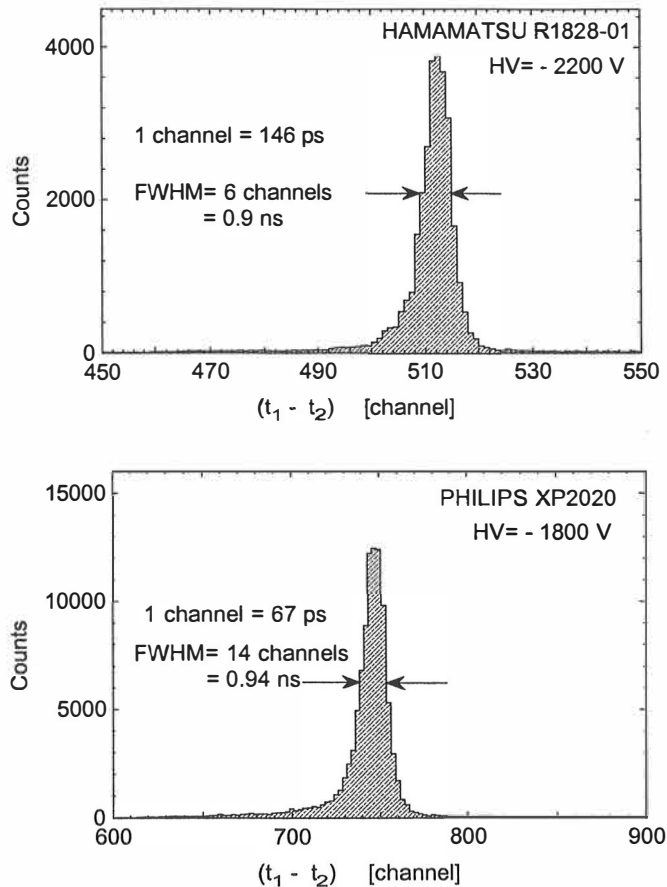


Figure 12. The prompt spectra from collimated  $^{60}\text{Co}$   $\gamma$ -source placed at the middle of the PSND accompanied with different PMs. Start signal was taken from one PM and stop from the second one.

The light collection process depends also on type, size and shape of the scintillator. Coupling optics, photo-multiplier's inherent transit-time-spread (TTS) and the associated electronics time spread are additional sources contributing to the final time uncertainty of the observed signals. The TTS depends directly on the quality of the photo-multiplier electro-optic system [Phi99]. By increasing the operational voltage (HV) between the photo-cathode and the first dynode the TTS decrease slowly. However, HV can not be too high because of the dark current leakage and consequent increase of the detection threshold. In addition, the time resolution is strongly limited by the large size of the scintillator because of the time spread of light collection induced by nuclear radiation absorbed in the volume of the scintillator. Therefore, variance ( $\sigma_g$ ) of the measured prompt spectrum (see Fig. 12) is composed of the variance of the time jitter in the scintillator ( $\sigma_s$ ), the two PMs and electronics used to process the signals ( $\sigma_{PE}$ ). Thus total variance is:  $\sigma_g^2 = \sigma_s^2 + 2\sigma_{PE}^2$ . Modern NIM and CAMAC electronics usually has good timing properties and yields a very small contribution (below 20 ps) to the time resolution. In the case of our long PSND the light collection process may introduce time spread larger than the time jitter of fast photo-multipliers. Self-absorption and re-emission processes affect the decay time of scintillating pulses and cause deterioration of time and energy resolution. From the measured data (see Fig. 12) I have estimated the standard deviation  $\sigma_s$  introduced by long scintillator to be 0.194 (ns) for Hamamtsu R1828-01 PM. I assumed that both R1828-01 PMs have equal standard deviation  $\sigma_{PM} = 0.235$  (ns) as reported in Hamamtsu catalogue [Ham01]. If we add about 55 ps for time uncertainty of the MCPD start detector the overall energy uncertainty for MCPD-PSND time-of-flight system can be estimated. Similar evaluations were performed for a set of commercially available fast PMs. The second column in Table 1 presents a comparison of the TTS ( $\sigma_{PM}$ ) of some recommended fast PMs. The measured widths of the prompt gamma spectra ( $\sigma_g$ ) are shown in the third column and in the last column estimations are given for appropriate overall energy uncertainties for neutrons detected by these assemblies when combined with MCPD start detector.

As a compromise between the price and detector performance I have selected XP2020 as an optimal PM for 100 cm long PSND. Note that using the rapidity of the ultra-fast XP2020/UR decreases only by about 30% final neutron energy resolution, due to the large size of the liquid scintillator.

Type of PM	TTS $\sigma_{PM}$ [ns]	$\sigma_g$ [ns]	Uncertainty [%]	
			at 3 MeV	at 20 MeV
XP2020/UR	0.15	0.29	2	7
R1828-01	0.235	0.39	3	9
XP2020	0.25	0.41	3	11
XP2262B	0.5	0.74	5	14

Table 1. The timing properties of several photo-multipliers [Phi99] and evaluated overall neutron energy uncertainty for the PSND placed at 171 cm long flight path.

The position resolution of the PSND supplied by two XP2020 PM was also estimated using the prompt time difference spectrum ( $t_1-t_2$ ) presented in Fig. 12. Since the total length of the PSND on ( $t_1-t_2$ ) spectrum is 10 ns, the width of the peak  $\sigma_g=0.41$  ns corresponds to position resolution of about  $\sigma_L=4$  cm for an equivalent neutron energy of 3.25 MeV. The position resolution of the PSND slightly depends on the total amount of n-induced light, which is proportional to the neutron incoming energy. Therefore, the position resolution also depends on the neutron energy as is shown in Fig. 13 for  $^{252}\text{Cf}$  source. By putting a gate on the energy loss spectrum in the scintillator, it is possible to determine the dependence of the position resolution on the energy deposited by an incident neutron in the scintillator. At larger incident neutron energies the contribution of the light collection properties become small, and position resolution depends mostly on the quality of the PMs.

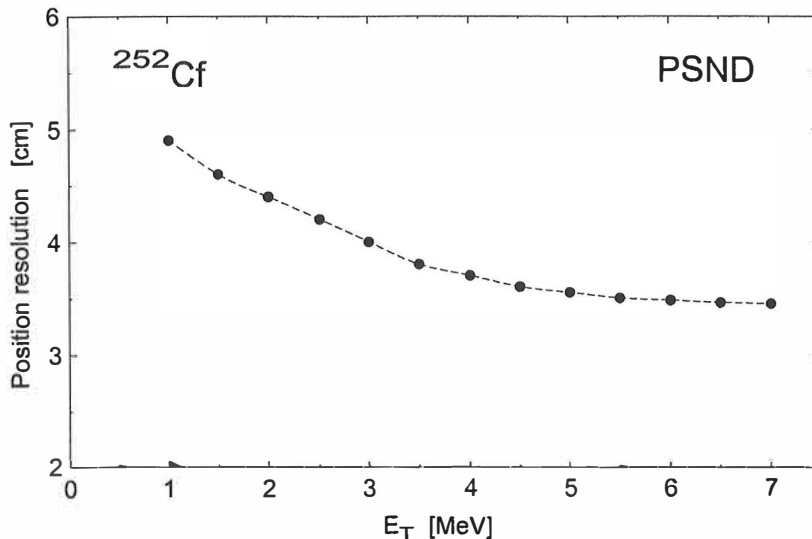


Figure 13. Experimentally measured position resolution of the PSND by using a  $^{252}\text{Cf}$  source as a function of deposited neutron energy in the scintillator.

### 3.3 Low-threshold neutron detector array

An array of low-threshold neutron modules was originally designed and constructed by the IReS-Strasbourg group [Bou96]. This low-threshold neutron detector array (LTND) is dedicated to studying exotic n-rich nuclei produced at ISOLDE, GANIL IGISOL facilities. Usually, the LTND array is accompanied by a beta-trigger detector ( $\beta$ TD) and several large Ge detectors for  $\gamma$ -ray spectroscopy. A single module and the whole LTND array are displayed in Fig. 14. As can be seen from Fig. 14 the size of the active volume of the LTND module is kept quite small to emphasize quality of the light collection and to avoid neutron multiple scattering within the scintillator.

Each neutron module consists of a cylindrical NE102A plastic scintillator (1 cm thick, diameter 10 cm) viewed by two ultra fast photo-multipliers (Philips-XP2020/URQ), connected horizontally and vertically, as shown at Fig. 14. Two light guides, with polished aluminium reflectors, ensure light collection from the scintillator.

The scintillator and PMs are enclosed in a light-tight box. The LTND neutron detector array permits detection of the low-energy neutrons down to  $E_{th} = 60$  keV with a mean detection efficiency around 13% for neutrons in the energy range 60 keV–5 MeV.

Low-energy detection is possible by adjusting the detection threshold just below the one photo-electron response. Minimisation of noise is performed by demanding fast coincidences between two PMs of each module derived from anode correlated signals. The spectra from each module are independently tuned by adjusting the delays of each module and combined into a single final neutron *TOF* spectrum. The modules are usually placed at about 50 cm from the source and at different angles having a total solid angle of about 2% of  $4\pi$ .

Besides *TOF* and energy measurements, LTND array is used for measurements of absolute neutron activities and determination of the neutron emission probabilities ( $P_n$ ). Therefore, precise knowledge of the neutron detection threshold ( $E_{th}$ ), intrinsic efficiency and timing properties of the LTND modules are the key element to determine the usefulness of the neutron detector array intended for high-precision neutron spectroscopy. Although calculation and evaluation of the known parameters of the scintillation material provide a good guide, the final calibration is done prior to the actual measurement by using the well-known  $^{29}\text{Na}$  source [Aud99].

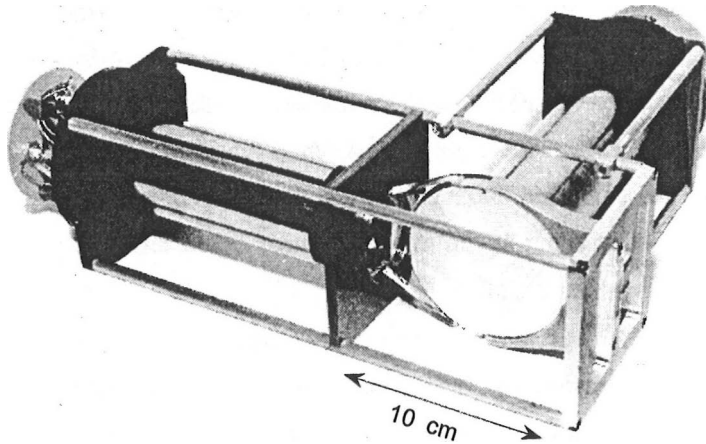
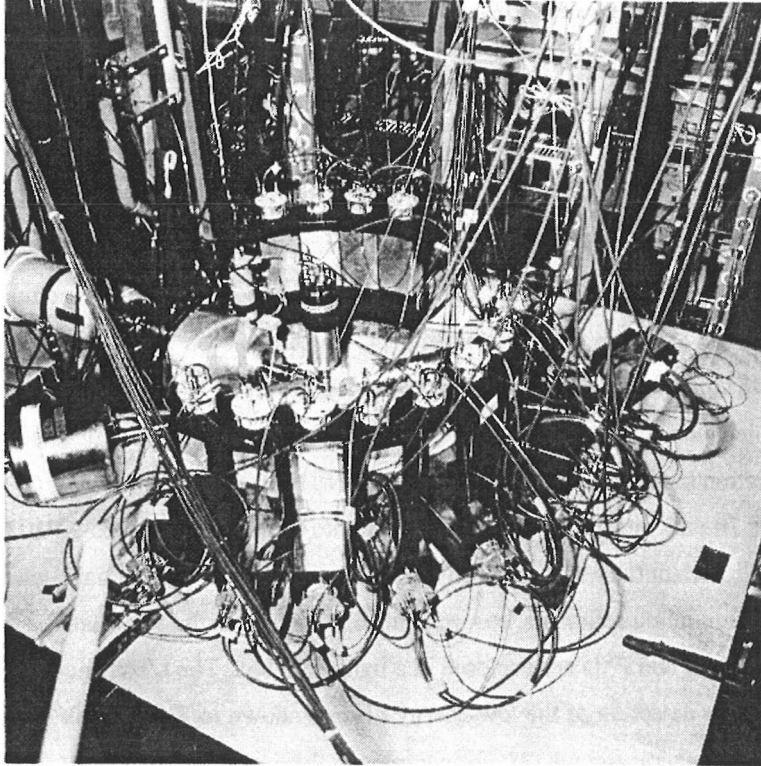


Figure 14. Top: beta-trigger detector in the centre surrounded by twelve LTND modules for delayed neutron spectroscopy. Bottom: a single module of the low-threshold neutron detector (LTND). Note minimisation of all inactive materials!

Therefore, the properties of the LTND array are determined both experimentally and by simulation. In other words, the results of measurements with  $^{252}\text{Cf}$  source are compared with results of simulations in order to get precise information about the

threshold of neutron detection and intrinsic efficiency as a function of neutron energy. A complete evaluation procedure is described in chapter 4. This procedure yielded  $E_{th}=60$  keV for threshold evaluation for the LTND array.

### 3.4 ${}^6\text{Li}$ -glass detector for low-energy neutrons

The value of  $E_{th}=60$  keV for the LTND module is already very close to the physical limits of the proton recoil scintillators. A possibility to detect even lower neutron energies is to use a complementary neutron-array constructed of  ${}^6\text{Li}$ -glass scintillator modules operated in *TOF* mode. The  ${}^6\text{Li}$ -glass array is more efficient at low energies, because  ${}^6\text{Li}(n,\alpha)\text{T}$  nuclear reaction (see Fig. 15) is used for the scintillation light production.

The  ${}^6\text{Li}$ -glass array could be placed quite close to the source ( $\sim 25$  cm) because of slow neutrons to be observed. This compact configuration intends to gain solid angle but still keeps the neutron energy error in reasonable range. Furthermore, a single module might be placed very close to the source (several cm), serving as an efficient counter in the low energy region, which allows extraction and determination of  $P_n$  values by means of simultaneous counting of beta and neutron activities.

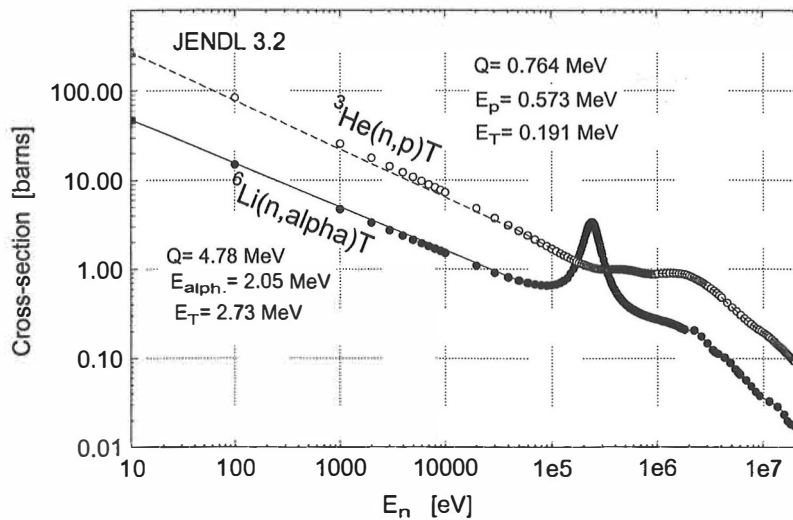


Figure 15. The  ${}^6\text{Li}(n,\alpha)\text{T}$  and  ${}^3\text{He}(n,p)\text{T}$  reaction cross-section for detection of low-energy neutrons.

I have designed and constructed a single prototype neutron module using small  ${}^6\text{Li}$ -glass scintillator GS20 in order to extend the range of detectable neutrons and explore detection possibilities under experimental conditions. The active scintillator, 5.1 cm in diameter and 2.4 cm thick cylinder, is optically coupled to the photo-cathode surface of the XP2020 photo-multiplier. I have used again our hand-made 1 mm thick silicon soft pad for optical coupling. The usual flight path of 25 cm for this single module provides a solid angle of  $\Omega_L = 0.24\%$  of  $4\pi$ . Timing and energy information are collected and neutron-gamma discrimination is performed via pulse-height analysis. The whole assembly is mounted in a light-tight, thin aluminium cylindrical container with a screw system, which provide easy handling and fixing of the detector close to the radiation point as shown in Fig. 16.

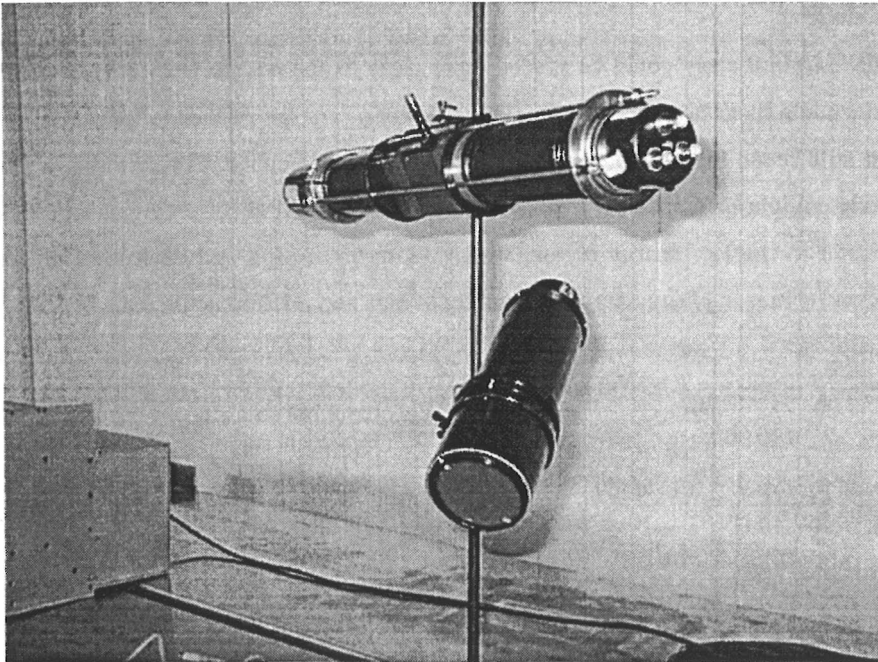


Figure 16. Prototypes of two detectors made in Jyväskylä. Upper: New module of NE213 liquid scintillator detector for studying of noise minimisation possibilities. Lower:  ${}^6\text{Li}$ -glass scintillator (GS20) module for detection of low-energy neutrons.



### 3.5 Small NE213 detector for noise minimisation

As mentioned experiments on nuclei very far from stability, such as studies of  $\beta$ -delayed neutron emission of n-rich nuclei, are often characterized by low-counting rates, below 1 ion/second at the collection point. This demands an efficient neutron detection system with a low-level of accidentals in long-term measurements. Accidentals may be due to uncorrelated beta, gamma and neutron background events in the start and stop detectors recorded within the resolving time of the coincidence circuit. Random noise of the photomultiplier is an additional source of accidentals. The level of accidentals is directly proportional to singles rates in the start and stop detectors. A neutron detector in usual experimental conditions is exposed to high-flux of gamma rays producing high counting rate in the contribution to the level of accidentals. For example the observed gamma-to-neutron event ratio for example in studying of  $^{33}\text{Na}$  decay was about  $\gamma/n=3$ .

These facts called for a construction of a prototype of neutron module (SLND), which has stable working conditions, possibility of minimisation of accidental, relatively low threshold and high intrinsic efficiency. For noise minimisation liquid scintillator NE213 was used, because of the possibility for n- $\gamma$  separation via pulse shaping of the anode signals.

The size and shape of the detector active part was designed by using the EFEN Monte-Carlo simulation (see chapter 4). The simulation results suggested a limitation of about 1.6 cm for the detector thickness and no more than 16 cm long active volume. These dimensions are optimal values to minimise neutron multiple scattering effects, which can destroy the detector properties. Furthermore, two fast PMs per detector ensured noise minimisation by operating in coincidence mode and provided position sensitivity of the SLND module. The position sensitivity (if compared with the LTND modules) further improved overall neutron energy resolution because of better knowledge of the exact interaction point along the scintillator. I have constructed a small NE213 neutron (see Fig. 16) as a compromise of all of these facts. Both ends of the detector scintillator ( $5 \times 1.6 \times 16$  cm rectangle) are viewed by a fast XP2020 photomultiplier. The detector is usually placed at a distance of 30 cm and covers a solid angle of  $\Omega_n = 0.7\%$  of  $4\pi$ . Two PMs provided a timing signal for *TOF* and total and fast integrated output signals ( $E_T, E_F$ ) for pulse-shape analysis. The

module has neutron detection threshold of  $E_{th} = 150$  keV and a mean intrinsic efficiency of about 14% for neutron energies between  $E_{th}$  and 10 MeV.

#### **4. Monte-Carlo simulations of neutron detector properties**

The simulation package EFEN has been written with the intention to perform a comparative study of several neutron detectors based on fast proton recoil scintillators (NE213, BC501A, BC408, NE102A), in particular, to determine the most important parameters like intrinsic efficiency and threshold for neutron detection. Simulations were also used in the detector design phase and helped in estimations of the critical parameters. Flexibility in setting different detector geometries corresponding to real experimental conditions allowed very easy evaluation of the detector properties for different detector's configurations. The simulation program EFEN has been written in the extended Fortran language commonly used on many PCs or UNIX machines. The relative simplicity of the simulation program easily allows suitable modification and application for many different types of detectors.

##### **4.1 Simulation of neutron interaction with scintillator**

Organic scintillators are aromatic compounds containing linked or condensed benzene-ring structures. Fig. 17 shows the structural formula of xylene, which is the main ingredient in scintillators. Xylene molecules are sensitive to excitation by light charged particles like electrons, protons, deuterons, tritons, alphas. These particles can be produced in reactions caused by incident neutrons or gammas. A very important characteristic of scintillators is related to the extremely rapid time decay of excited molecules. This is the reason why detectors based on these scintillators have very good timing characteristics. The important physical properties of most scintillators can be found in the Bicron catalogue [Bic98]. Scintillation light in xylene arises from transitions of free valence electrons belonging to the molecules. These delocalized electrons are not associated with any particular atom in the molecule and occupy what are known as  $\pi$ -molecular orbitals.

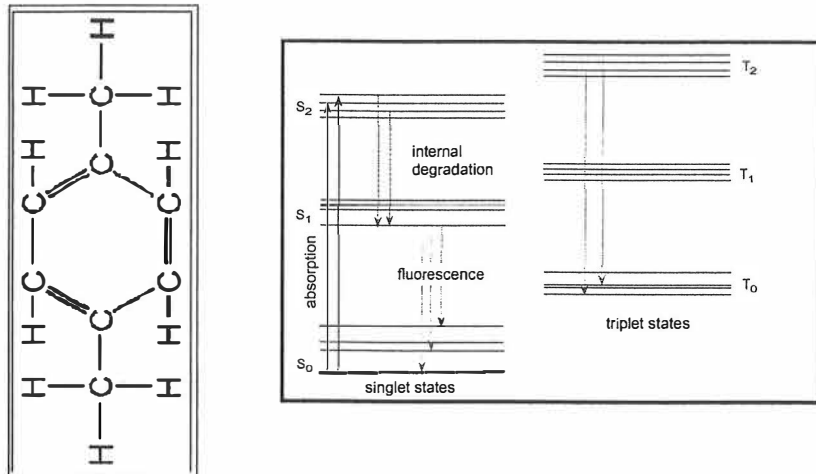


Figure 17. The structural formula of xylene and energy level diagram of a xylene molecule.

A typical energy diagram for these orbitals is shown in Fig. 17, where it is possible to distinguish the spin singlet states from the spin triplet states. The ground state is a singlet state, which is denoted by  $S_0$ . Above this level are the excited singlet states ( $S_1, S_2, \dots$ ) and the lowest triplet state ( $T_0$ ) and its excited levels ( $T_1, T_2, \dots$ ). The energy spacing between electron levels is of the order of a few eV. There is also fine structure associated with each electron level, which corresponds to excited vibrational modes of the molecule. The charged particles excite both the electron and vibrational levels. The singlet excitations generally decay immediately ( $<10$  ps) to the  $S_1$  state without emission of radiation. This process is known as internal degradation. From the  $S_1$  state radiative decay to one of the vibrational states of the ground state  $S_0$  within a few nanoseconds is highly probable. This is a normal process of fluorescence, which is described by the fast component of the time evolution of the decay process,

$$N_{ph}(t) = A \exp(-t / \tau_F) + B \exp(-t / \tau_S), \quad (3)$$

where,  $N_{ph}$  is the number of photons emitted at time  $t$ ,  $A$  and  $B$  are specific constants for any scintillation material,  $\tau_F$  and  $\tau_S$  are the decay constants for the fast and slow components, respectively. A similar internal degradation process also occurs for the triplet excited states, which brings the system to the lowest triplet state. While

transitions from  $T_0$  to  $S_0$  are possible, they are however, highly forbidden by multipole selection rules. The  $T_0$  state instead, decays mainly by interacting with another excited  $T_0$  molecule leaving one of the molecules in the  $S_1$  state (interaction goes over phonon production). Radiation is then emitted by  $S_1$ , as described above, but this light appears after a delay time characteristic to the interaction between these excited molecules. This is a slow component of scintillator light. Existence of these two components forms the basis for the technique of pulse shape discrimination between different particles, which excite liquid scintillators. The scintillator light response is actually specific to the kind of interaction for different charged particles with xylene molecules. This presents the basis for possibilities to distinguish different types of radiation. More precisely, the shape analysis of scintillation pulses allows one to discriminate between different reaction channels induced by incident neutrons, which produce different charged particles ( $\gamma$ -rays, protons, tritons, alphas etc...).

The detection process in scintillators simulated by EFEN proceeds in several stages. The first process is slowing-down due to neutron collisions with hydrogen ( $^1\text{H}$ ) and carbon nuclei ( $^{12}\text{C}$ ), which are the basic ingredients of organic proton-recoil scintillators. Neutron propagation involved in the simulation assumes elastic collisions with H and C for neutron energies below 4.8 MeV, which is the threshold for nuclear reactions with C nuclei. Ultimately, the neutron comes into thermal equilibrium with the medium and diffuses within the scintillator volume. The dissipation of neutron's total initial kinetic energy occurs in nanosecond time scale giving rise to initial scintillation signal. Escaping through the walls of the active scintillator's volume or a non-elastic collision with C, represent the processes terminating the history of followed neutron in the EFEN.

The incident neutron can interact with any of the scintillator ingredients (hydrogen H or carbon C nuclei) in such a way that the final products are light-charged particles and gamma rays. Energy transfer between the incident neutrons and the particles produced is not a linear process. In other words, information about the incident neutron energy is lost and cannot be measured in this way with a good energy resolution. However, for neutron spectroscopy a *TOF* technique can be used taking advantage of the fast scintillation processes where only a small portion of the incident neutron energy is enough to provide appropriate signals. In our simulation model the parameterisation of Birks [Bir72] is used to calculate light output for different

particles produced in neutron interaction where the number of photons  $dN_{ph}$  emitted per path-length  $dx$  traversed by particle is given by:

$$\frac{dN_{ph}}{dx} = n_0 \frac{dE}{dx} \left[ 1 + kB \left( \frac{dE}{dx} \right) \right]^{-1}, \quad (4)$$

where,  $dE/dx$  stands for stopping power of the scintillator,  $n_0$  is the average number of photons per unit of deposited energy, and  $kB$  is a characteristic of the scintillator. All parameters for the set of various scintillators considered can be found in the Bicon catalogue. The total light yield is obtained by integrating eq. (4) between zero and the initial particle energy. Furthermore, to simulate signal formation each particle trajectory is divided into small segments which produce a constant energy loss  $\Delta E$ , then eq. (4) is numerically integrated with this energy to yield the number of photons  $\Delta N_{ph}$ , (0.1 MeVee<sup>-</sup> in case of NE213 produces about 1000 photons)<sup>1</sup>, which are emitted isotropically into the full solid angle. This procedure is iteratively repeated until the charged particle has completely lost its energy in the active scintillator volume. Absorption of the light in the simulation is described by equations 5.

$$P(x) = \exp(-x / l_a). \quad (5)$$

$P(x)$  represent the probability to reach the distance  $x$  in a scintillator with an attenuation length constant  $l_a$ . When the light signal reaches the photo-cathode of the PM tube the photons eject a photoelectron with the quantum efficiency coefficient  $K_e$  (10% for Philips XP2020 PM). The electrons are further focused onto the first dynode with efficiency  $F_e$  and amplified by the dynode chain with a factor of  $G$ . The PM anode current  $I(t)$  is given by product:

$$I(t) = e \Phi(t) K_e F_e G, \quad (6)$$

where,  $\Phi(t)$  is the rate of photons at the photo-cathode surface and  $e$  the elementary charge. Finally, the corresponding voltage pulse at the anode  $\tau=RC$  circuit is given as:

---

<sup>1</sup> Here I have used electron equivalent units MeVee<sup>-</sup> for deposited energy in scintillator. Connection with proton recoil equivalent units MeV, is in given by eq. (12).

$$V(t) = \frac{R e^{-t/\tau}}{\tau} \int_0^{\max} \exp(t/\tau) I(t) dt . \quad (7)$$

The simulation uses a simple measurement of the anode output signal-shape to estimate all variables in eq. 7. An example of the anodes response on  $^{60}\text{Co}$  gamma source taken from the LTND module is shown in Fig. 18. Under this condition, the amplitude of  $V(t)$ , a measurable quantity, is proportional to the total number of photons transported to the photocathode and in the EFEN simulations is used to determine the threshold for neutron detection ( $E_{th}$ ).

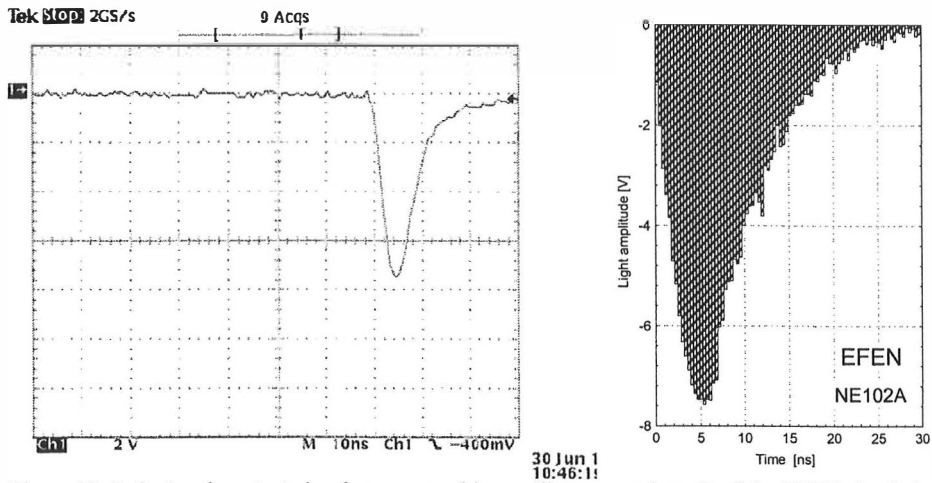


Figure 18. Left: Anode output signal as measured by oscilloscope and result of the EFEN simulation for the LTND module (at the right).

## 4.2 Nuclear data base as input for the EFEN simulation

As a stochastic process the interaction of neutrons with different scintillators in the EFEN simulation is described by total cross-sections for interactions with constituents of the scintillators. I have given preference to the evaluated cross-section data files (ENDF/B-VI and JENDL 3.2) received from the International Atomic Energy Agency (IAEA-Vienna and [Lan98]). These data represent a compact-package of all the available data, which are periodically updated according to experiments performed over the last few years. Also, these data serve as referent data and convenient basis for comparison of results of different simulations. For higher neutron energies ( $E_n > 32$

MeV) I have used the data reported in ref. [Gue76] and references therein. Therefore in the EFEN simulation I have used nuclear data libraries as input files to produce information about involved reaction cross-sections, angles of scattered neutrons and produced particles. There are many different reaction channels for neutron interaction with light charged particles produced in the output channel. The most important (seven) channels for neutron detection are shown in Fig. 19. Angular distributions of scattered neutrons and produced particles are given in the c.m. system by eq. (8) in forms of energy dependent Legendre coefficients  $C_l(E_n)$ .

$$\left(\frac{d\sigma}{d\Omega}\right)_{c.m.} = \frac{\sigma_t(E_n)}{4\pi} \left[ 1 + \sum_{l=1}^{l_{max}(E_n)} C_l(E_n) P_l(\cos\theta_{c.m.}) \right], \quad (8)$$

where,  $\sigma_t(E_n)$  is the total cross section for the given reaction at the incident neutron energy  $E_n$ ,  $\theta_{c.m.}$  is the c.m. angle of emission of the reaction product,  $P_l(\cos\theta_{c.m.})$  is the Legendre polynomial of the order  $l$ ;  $l_{max}(E_n)$  is the order of the last, non-zero coefficient in the decomposition (8).

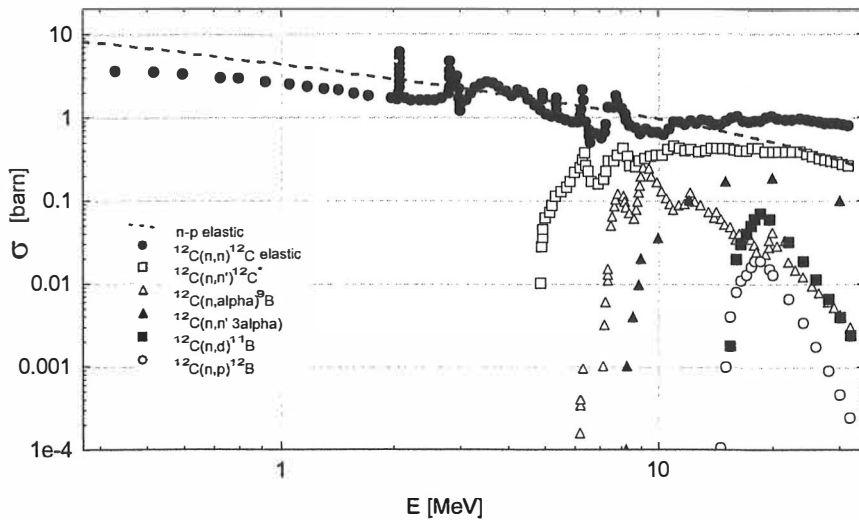


Figure 19. Cross-section of reactions which are important for neutron detection by proton-recoil scintillators (taken from ENDF/B-VI and JENDL 3.2 libraries).

### 4.3 Modelling and sampling of neutron detection

Statistical modelling of neutron interaction with different materials is governed by probability density functions (PDF) of interaction. Physical processes described by the PDF approach reality by sampling a large number of interaction events [Sob83]. The EFEN simulation consists of several modules of which some are intended to be modified according to the specific detector type. In particular, the definition of detector geometry and active volume, type of scintillator, properties of the neutron source, as well as choice of the quantities to be simulated are at the disposal of the user. A simplified flow chart of the program is displayed in Fig. 20. Its execution starts with the block marked as "block 1", which contains input variables and necessary parameters describing the initial state of the system (neutron source–detector). The detector active volume in 3D space and spectral characteristic of the neutron source  $\Psi(\nu, \varphi, E_n)$  are defined here. When the initial neutron velocity vectors are defined (by  $\nu, \varphi$  angles and neutron velocity) the "start" points  $(x_0, y_0, z_0)$ , are found. These are points where neutron velocity vectors are crossing the surface of the scintillator volume and the probability for neutron detection becomes larger than zero. Furthermore, requirements for total simulation statistics and energy steps are also here in block 1. My experience shows that one million simulations for each step of 100 keV of neutron energy is sufficient to suppress the statistical fluctuations. After completion of the initialisation phase, the program executes the main DO loop, where the subroutines emitting and tracking particles are called. The essential part of EFEN is the tracking module. It tracks all particles, currently in the detector volume and describes history of neutron interaction. Tracking module consists of several sub-tasking programs marked in Fig. 20 as blocks (2,3,4). The block 2 calculates neutron mean free path  $\lambda$  until interaction occurs for a given amount of neutron energy. Because of the many processes involved the probability of neutron interaction is composed as a sum of two main interaction branches (on H or/and C-nuclei). Therefore mean free path in the block 2 is calculated by using

$$\lambda(E) = 1 / (n_H \sigma_H(E) + n_C \sigma_C(E)), \quad (9)$$



where,  $\sigma_H(E), \sigma_C(E)$  are total cross-sections for neutron scattering on H and C nuclei (taken from the nuclear data libraries),  $n_H, n_C$  are concentrations of H and C atoms in a scintillator. The mean free path is further used for sampling the distance  $S$  to the next interaction with the nucleus. The  $S$  is random variable with exponential distribution of the PDF [Sob83]. To sample the distance  $S(E)$  between two points of neutron interaction in the simulation operational formula (10) was used:

$$S(E) = -\ln(\varepsilon) / \lambda(E), \quad (10)$$

where,  $\varepsilon$  is a random number with uniform distribution on segment (0,1) obtained by a random number generator subroutine. The exact outcome of the neutron collision depends on the nature of the particles. Therefore, block 3 simulates the different collision channels using the operational formula (11) to reach a decision about the type of interaction, which actually stands for the relation between a particular channel and all possible interaction channels.

$$P_H(E) = \frac{n_H \sigma_H(E)}{n_H \sigma_H(E) + n_C \sum_{i=1}^6 \sigma_C^i(E)} \quad P_C^i(E) = \frac{n_C \sigma_C^i(E)}{n_H \sigma_H(E) + n_C \sum_{i=1}^6 \sigma_C^i(E)}. \quad (11)$$

In general, this is the way how dynamic channeling of the code's flow is produced for different reactions (channels). All channels have a certain statistical weight as calculated by eq. (11). When the neutron goes into any channel, block 4 calculates the angle of scattering. In each channel, the scattering angle is first sampled in the centre of mass system and is then translated into the laboratory system. When information about  $S$  and the angle exist, the position of the scattering point is located and it is possible to check whether this point is inside the active volume. This is done in the fifth block. If the point of scattering is outside the active volume, the neutron history is terminated and the code returns to the beginning where a new neutron history is initiated. If the point is inside the active volume, then such an event may increase efficiency. Also, the flow of the code returns to the fourth block where the calculation of neutron kinematics as well as kinematics of the produced particles in neutron collision are carried out.

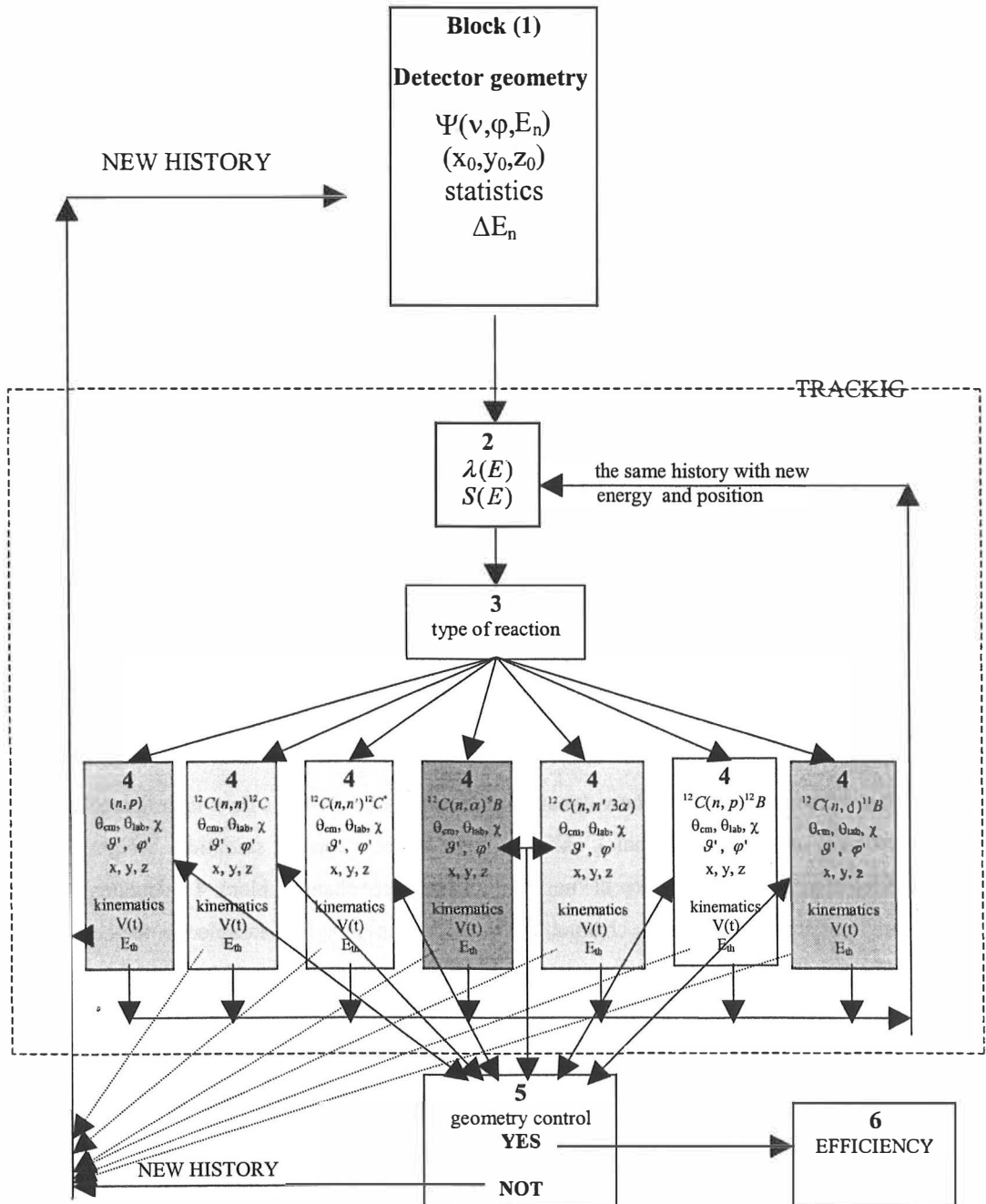


Figure 20. Flow chart of the EFEN simulation.

For specified charged particles the total energy loss  $\Sigma_i(\Delta E_i)$  is further calculated and attributed to the amount of photons which form the output signal. If the amount of neutron energy after scattering is larger than the threshold ( $E_{th}$ ), the flow of simulation goes to the second block where the new scattering for the same neutron is initiated with the remaining energy and with the new laboratory angle. Then follows the sampling of  $S$  and choosing the type of reaction. If the remaining energy is too low (below  $E_{th}$ ) the action of the tracking routine terminates. In other words the neutron history is followed while the neutron has enough energy for detection or until the neutron escapes from the scintillator.

In addition, the scattering multiplicity ( $M$ ) of a neutron is monitored and makes it possible to follow how many scatterings a neutron has had in a typical neutron history.

#### 4.4 Results of EFEN simulations

The results of the EFEN simulation refer to several different detectors at usual source-detector geometries, which fulfils the constraints imposed by the real physical experiment. In presenting the results of the simulation the intrinsic efficiencies for the set of different detectors were stressed. Some of other results intend to fulfill complete description of the detector properties and detection process for instance to optimize the detector design and improve quality of experimental data. A sample of representative results will be given here including intrinsic efficiencies, multiple scattering effects and optimal detector sizes, influence of diaphony and inactive materials on neutron detection process.

When calculating the efficiency, I attempted to reproduce actual experimental conditions, such as the correct geometry of the active (scintillator) and inactive materials, the threshold settings, and the energy spread of the incident neutrons. Efficiencies near the threshold are especially sensitive to various experimental parameters and are expected to be more difficult to reproduce accurately. To achieve a good noise rejection the simulations have been made with a limitation for signal amplitudes of the formed light-outputs. In the simulation I have used ( $E_{th}^{el}$ ) electron-equivalent light output units (expressed in  $\text{MeVee}^-$ ), as recommended by Bicron.

Correlation with more familiar proton recoil units ( $E_{th}$ , expressed in MeV) can be found by

$$E_{th}^{el} = a_1 E_{th} - a_2 [1 - \exp(-a_3 E_{th}^{a_4})], \quad (12)$$

where,  $E_{th}$  is the proton energy and  $E_{th}^{el}$  is the electron energy that gives the same light output. The constants  $a_i$  ( $i=1,\dots,4$ ) for specific scintillators are reported in ref. [Bic98,Mou94]. The simulations usually considered isotropic neutron source where  $10^6$  simulations were made for each of 100 keV energy step. The results calculated by EFEN for intrinsic efficiency as a function of neutron energy and threshold  $E_{th}$  are shown in Figs 21-25 for several types of detectors involved in the experiments. The first presented result is actually a comparison of results obtained by EFEN and MENATE simulations [Des98]. The MENATE simulation stands for the standard programme used to evaluate properties of DEMON neutron module. Comparison is shown in Fig. 21 together with a schematic presentation of a single DEMON module.

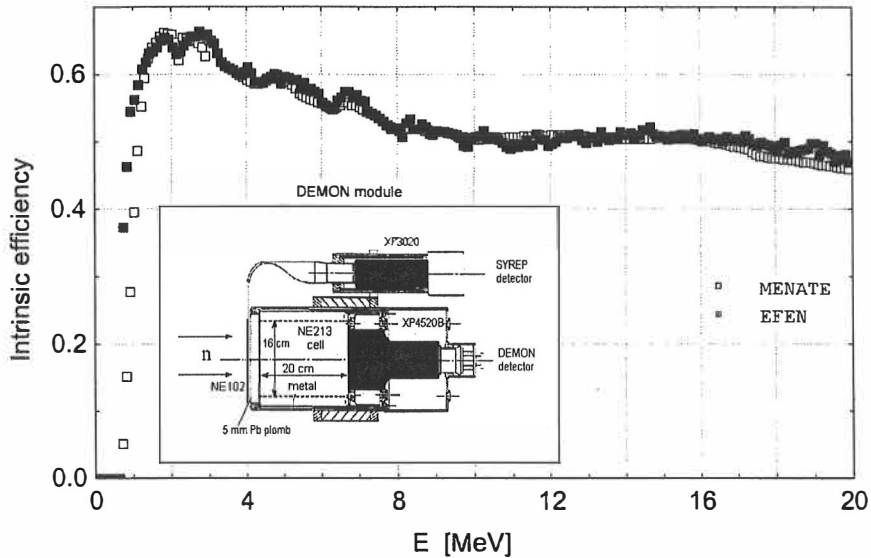


Figure 21. Comparison of results for one cell of DEMON detector calculated by MENATE [Des98] and EFEN codes for  $E_{th}=700$  keV threshold.

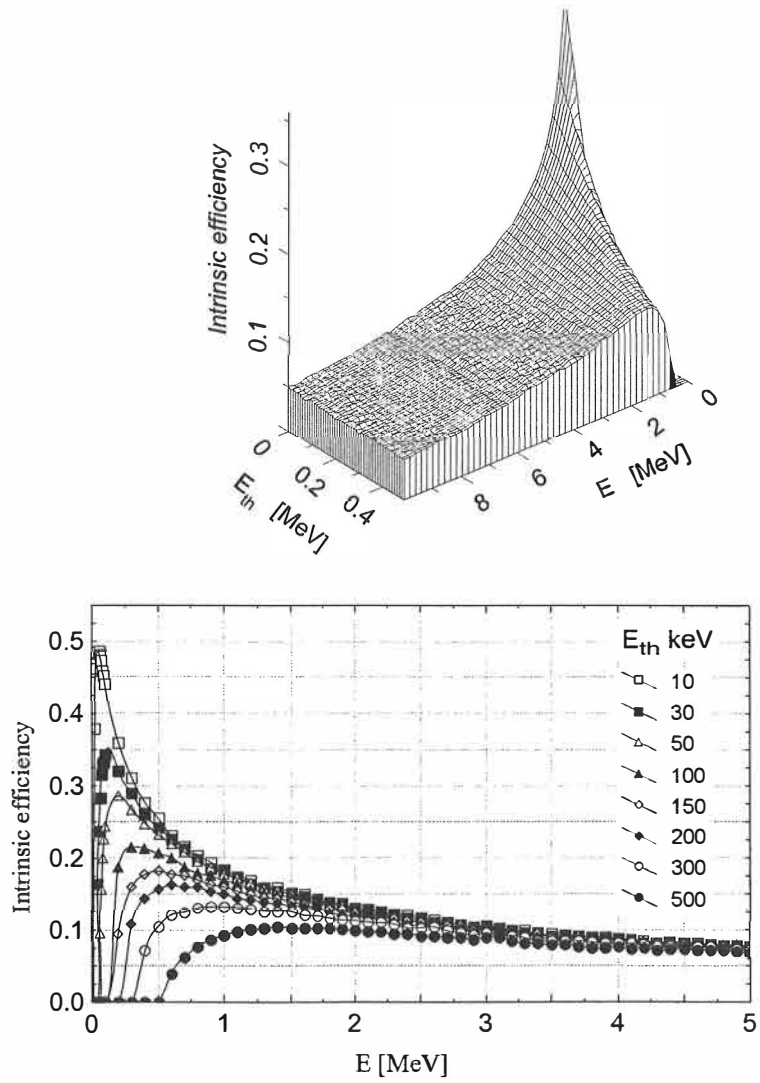


Figure 22. Intrinsic efficiency of the LTND module obtained by EFEN simulation as function of neutron energy and for different detection thresholds  $E_{th}$  (MeV).

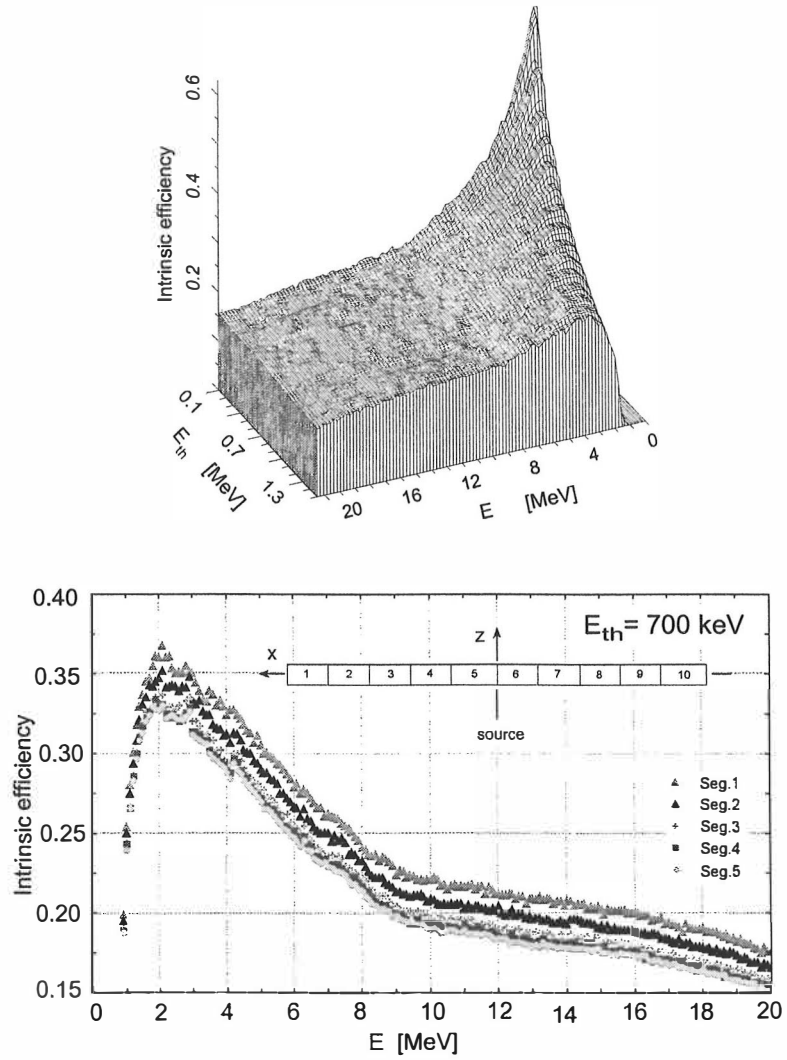


Figure 23. Top: Intrinsic efficiency for central 10 cm long part of the PSND as a function of energy and detection threshold  $E_{th}$ . Bottom: Intrinsic efficiency for several 10 cm long parts of the PSND module obtained by EFEN simulation for threshold  $E_{th} = 700$  keV.

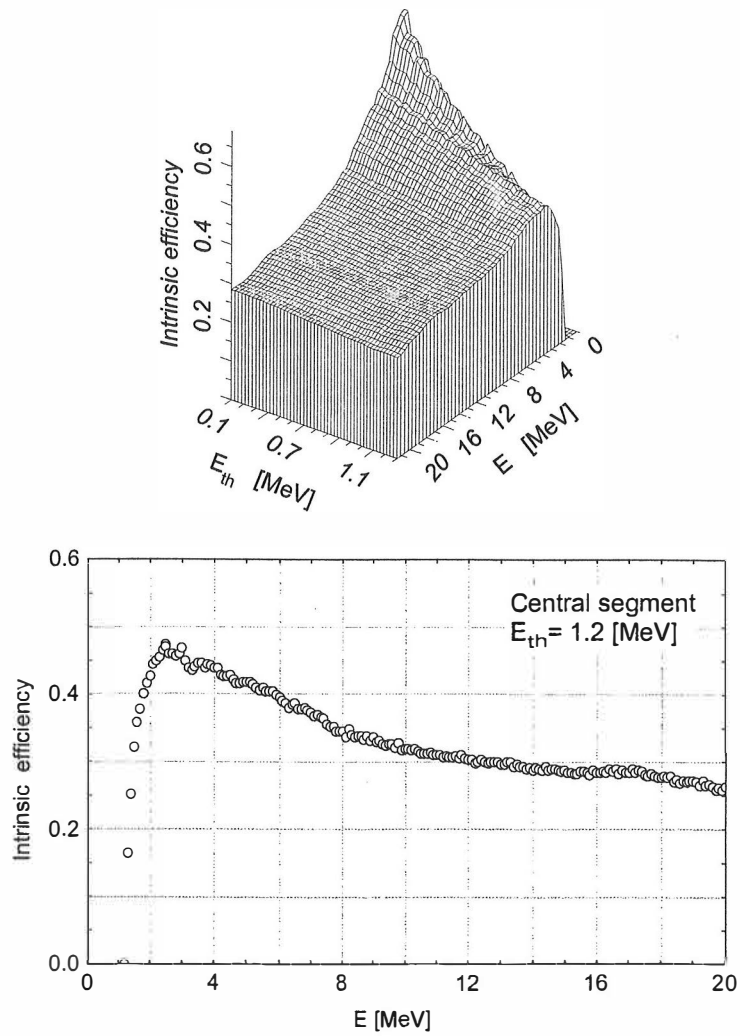


Figure 24. Top: 3D correlation, intrinsic efficiency-neutron energy  $E$  and detection threshold  $E_{th}$  for the LANCER module. Bottom: Intrinsic efficiency for the central 10 cm long part of the LANCER module as function of energy for  $E_{th}=1.2$  MeV threshold.

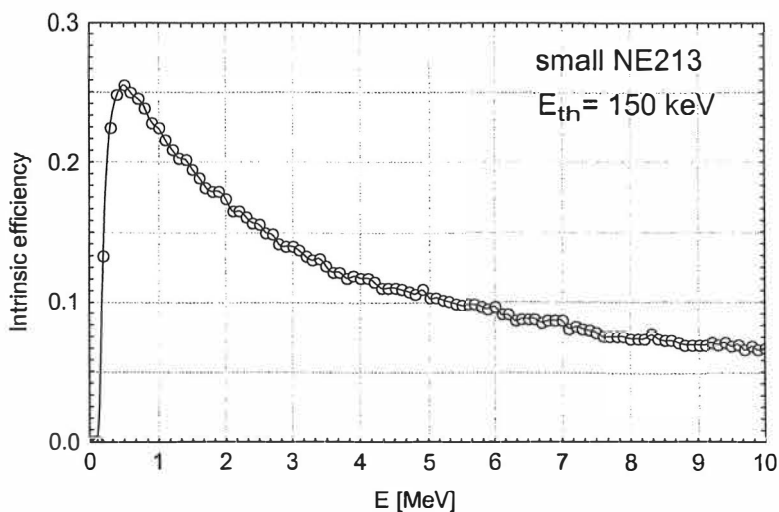


Figure 25. Intrinsic efficiency for the small NE213 neutron detector as evaluated by combination of the EFEN simulations and measurements.

Besides the geometric effects two prominent shapes constitute an efficiency curve presented in Figs 21-25. For “thin” detectors (Figs 22 and 25) the shape of efficiency curve is mainly dominated by elastic scattering on H nuclei. For the medium-size detectors like (PSND), there are two main contributions. The first constituent refers to the energy range  $E_{th}$ –9 MeV, and the second refers to energies above 9 MeV. The first part mainly corresponds to elastic scattering on H-nuclei, and the second is predominantly caused by inelastic scattering on carbon nuclei. These processes are actually governed by cross-section values for different channels at given amounts of energy (see Fig. 19). For the large-size detectors like (LANCER and DEMON) the relative contribution of both principal interaction channels (interaction with H and C nuclei) are similar.

In processes involved in scintillators a neutron can be scattered more than once before escaping the active volume or before being absorbed. Those multiple scattering events happen faster than the collection of light by fast photo-multipliers (XP2020) changing the shape of the total light output signal. The final effect is a non-uniform process of light-collection and signal processing. Furthermore, it disturbs the pulse-shape analysis and thus the quality of the n- $\gamma$  discrimination. The ideal situation would occur if it would be possible to detect incident neutrons (in large energy range) by only one act of scattering, and if the place of neutron deposition would be a point. However,



the neutron energy deposition process has its time-space finite extension and it is not a point. Multiple scattering effects actually create an upper-limit factor for active detector volume. In other words, the size of detector must be kept small to obtain certain detector quality. On the other hand, increasing the detector size (radius), will increase the probability for detection and intrinsic efficiency. However, there will be more complicated effects caused by multiple scattering, which will damage the time and energy resolution. These effects were estimated by EFEN simulation for different incident neutron energies as shown in Fig. 26 and results were used in the design phase of the small NE213 neutron detector dedicated to noise and accidental minimisation experiments at ISOLDE. The size of the active part was chosen in such a way that single scattered events dominate and at the same time the intrinsic efficiency is still relatively high. Projection on the detector thickness (R-M) multiplicity plane is shown in Fig. 26, also. Different curves represent calculations for different incident neutron energies. As can be seen in Fig. 26, increase of neutron energy contributes to two processes affecting the intrinsic efficiency. Firstly, increasing neutron energy decrease number of scattering per one neutron history and cause lower probability for detection or lower intrinsic efficiency. Secondly, the number of neutrons scattered only once in the detection process in the scintillator, decrease. Therefore, the chosen thickness for the small NE213 detector was 1.65 cm which favours one neutron scattering events but still allows relatively high efficiency in the selected energy range ( $\sim 1.5$  MeV) for neutron spectroscopy.

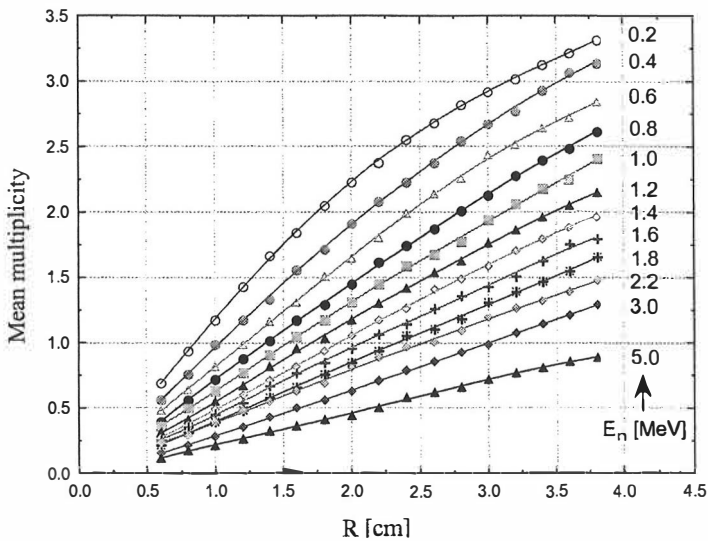
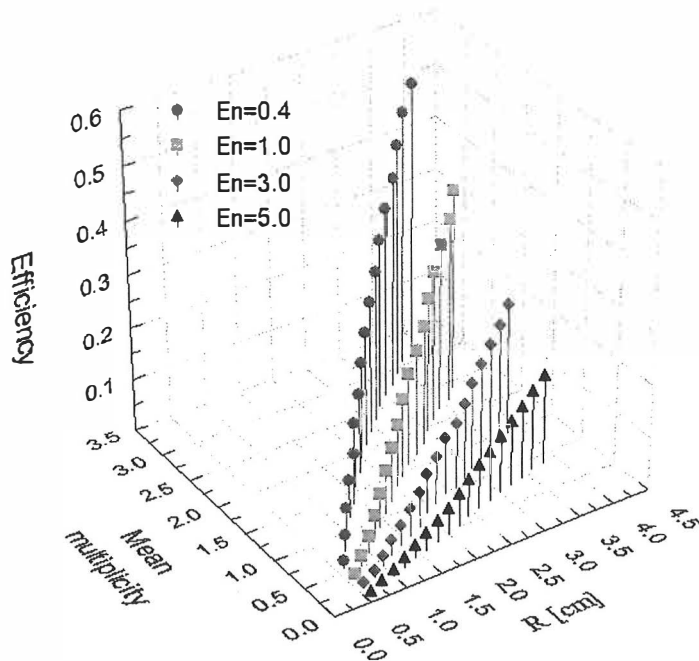


Figure 26. The multiple scattering effects calculated by the EFEN simulation in the NE213 liquid scintillator as function of active volume size. Top: Dependence between diameter (R) of active volume, mean neutron multiplicity (M) and intrinsic efficiency for different neutron energies ( $E_n$ ). Bottom: Mean multiplicity (M) as function of the detector thickness (R) for different neutron energies.

The shape and intensity of the light response depends on reaction types. The neutrons, which have been scattered on hydrogen after an initial elastic scattering on carbon

cause a complicated effect in relation to detection and present the diaphonic effect. The reason for this is very small light response of a scintillator on carbon ions (50 times less than for a proton with the same energy), which makes these interactions invisible by the PM.

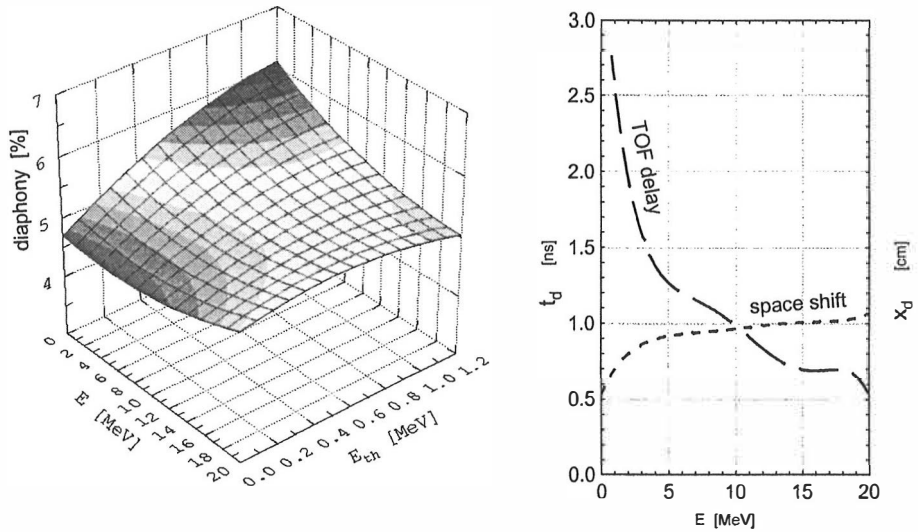


Figure 27. Left: Representation of the role of diaphonic effect in the PSND detector. Right: influence of diaphony on registration as calculated by EFEN simulation for different neutron energies. For the *TOF*-delay and space-shift right and left scales are valid, respectively.

The diaphonic effect shifts neutron energies measured by *TOF* towards smaller values. The main reason for this shift is an increased time of travel before the “visible” point of scattering. To explore and estimate these effects I extended the EFEN simulation and Fig. 27 shows results for the PSND detector. As can be seen from Fig. 27 the diaphonic effect contributes about 5-6 % to all types of reactions. It is also clear that the detection threshold has a weak influence on the diaphony. This percentage (5-6%) of interaction causes a space shift of about  $\pm 1$  cm, and a delay time of neutron detection as shown in Fig. 27. Finally, for any given size and geometry of a scintillator, diaphony effects generally decrease with increasing of incident neutron energy.

In order to improve the quality of our neutron measurements with the PSND at HENDES facility I have estimated the influence of inactive materials on the detection process by using EFEN simulation. The inactive materials involved in experiments at the HENDES are the stainless-steel spherical chamber (composed of several ingredients: Fe, Cr, Ni, C), the titanium box around each PSND, and the quartz cylinder (Si, O) containing NE213 scintillator. The dimensions of all the materials are known and the concentration of the centres for interactions can be calculated to provide input for EFEN simulation. Cross-sections for neutron interaction for all inactive materials were found in ENDF/B-VI library.

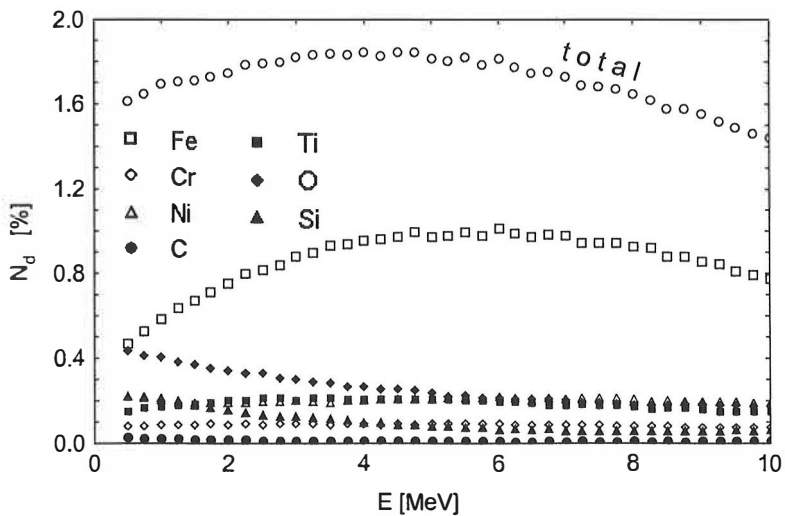


Figure 28. Percentage of incident neutrons, which have interacted with inactive materials at HENDES facility as calculated by EFEN simulation.

Finally the simulation showed that about 1.7% of incident neutrons ( $N_d$ ) are lost in the inactive materials in a typical run at HENDES as shown in Fig. 28.

#### 4.5 Threshold, efficiency and energy resolution evaluations

In order to get precise information on the interplay of energy threshold of neutron detection and on intrinsic efficiency several measurements with a  $^{252}\text{Cf}$  source were performed at the HENDES facility.  $^{252}\text{Cf}$  is a spontaneous fission source where the associated neutrons are emitted isotropically in space. Furthermore, the shape of neutron energy spectrum is well-known and serves as the reference spectrum in many experiments. Before and after each experiment, californium spectra are taken not only for calibration purposes but also for testing and tuning of the experimental set-up including electronics.

When neutron spectra from  $^{252}\text{Cf}$  were measured the start signal for *TOF* was given by fission fragments, registered by a micro-channel plate detector, and the stop signal was provided by the neutron modules. In the case of a PSND module the neutrons are first selected by n- $\gamma$  separation technique and then converted into an energy spectrum. A typical  $^{252}\text{Cf}$  neutron *TOF* spectrum is shown in Fig. 29.

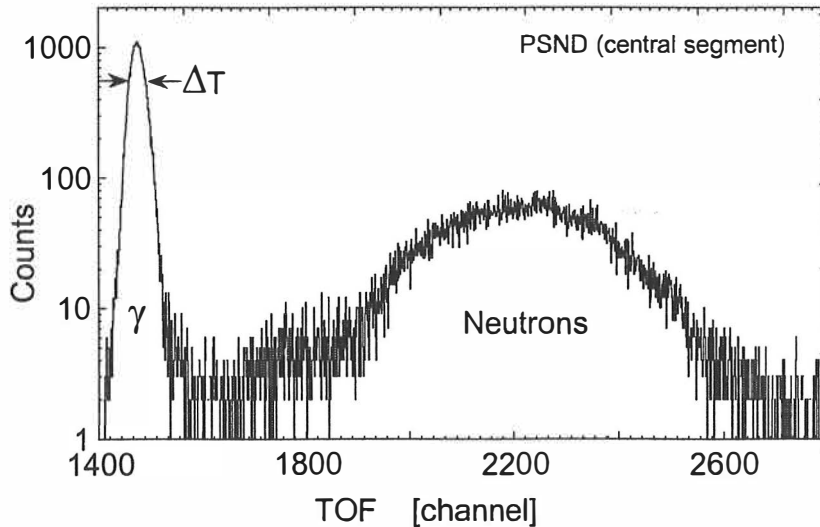


Figure 29. Neutron *TOF* calibration spectrum of  $^{252}\text{Cf}$  source detected by central segment of the PSND module.

Subsequently, the neutron energy spectrum is corrected for intrinsic efficiency and compared to the well-known reference spectrum of  $^{252}\text{Cf}$  [Bud88]. The efficiency correction is performed for the set of intrinsic efficiencies obtained by the simulation for different thresholds ( $E_{th}$ ).

For the LTND module the curve with the  $E_{th}= 60$  keV threshold correction resulted in the best agreement with the reference neutron spectrum and indicated the real operational threshold of the LTND. Furthermore, the well-reproduced shape of the intrinsic efficiency corrected  $^{252}\text{Cf}$  spectra confirms that the EFEN simulation involved all neutron detection processes in a proper way. In addition, a sharp increase of the neutron intensity at 60 keV marks furthermore the detection threshold. The sudden increase of the neutron intensity indicate the edge where noise starts to dominate the observed spectra. This noise is mainly caused by thermal emission of electrons from the PM photo-cathode. The same procedure for the PSND module yielded 700 keV threshold for neutron detection. The calibration spectra of  $^{252}\text{Cf}$ , measured by the LTND and PSND modules are shown in Fig. 30 together with actual intrinsic efficiencies as a function of neutron energy.

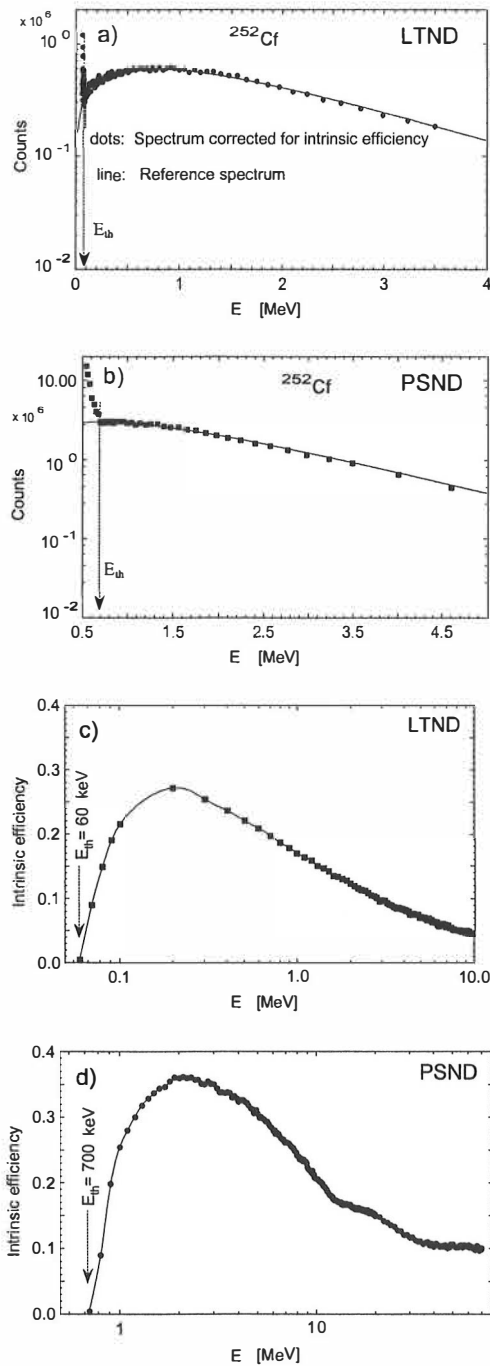


Figure 30(a) Neutron spectrum of  $^{252}\text{Cf}$  (dots) measured by LTND modules corrected for intrinsic efficiency of the detector is compared to the reference spectrum (lines) taken from ref. [Bud88]. (b) The same for the PSND module and for the 10 cm long central part. (c) Intrinsic efficiency of the LTND and PSND module (d) as evaluated by combination of  $^{252}\text{Cf}$  measurements and EFEN simulations.

The evaluation for a large-size LANCER module yielded an actual threshold of  $E_{th}=1.2$  MeV and efficiency was already shown in Fig. 24. The actual intrinsic efficiency for the small NE213 neutron detector was already presented in Fig. 25 such as result of measurements and simulation.

In the transformation from measured  $TOF$  to kinetic energy  $E$ , I have used the relativistic equation:  $E = m_n (\kappa - 1)$ , where  $m_n$  is the energy equivalent of the neutron mass (939.56 MeV) and  $\kappa$  is the Lorentz factor. Due to non-linear transformation from time to energy, the energy spectrum is stretched-out for long and compressed for short time-of-flight. Hence, in the  $TOF$  measurements, energies of fast and slow neutrons are obtained with different resolutions. The spectra with unequal energy bin size are usually then transformed in a second step to equal energy bins. The neutron energy resolution of the used neutron detectors is dominated by two physical sources. The first one is connected to the time uncertainty of the start (trigger detector) and stop (timing of the neutron modules) signals, respectively. The second one is related to the pathlength uncertainty in the neutron flight path. This uncertainty is caused by not knowing precisely the neutron interaction length inside the scintillator whose thickness is not negligible with regard to the flight path. Consequently, the overall energy resolution is given by:

$$\Delta E_n / E_n = \kappa (\kappa + 1) \sqrt{(\Delta L / L)^2 + (\Delta TOF / TOF)^2}, \quad (13)$$

where,  $\kappa$  is the Lorentz factor,  $L$  the measured flight path,  $\Delta L$  and  $\Delta TOF$  flight path and time uncertainties, respectively. For an estimation of the energy resolutions for the detectors  $^{252}\text{Cf}$  neutron  $TOF$  spectra were again used, but now the prompt gamma parts. It is supposed that total time uncertainty  $\Delta T$  (from start and stop detectors) is directly measurable and presents the width of the prompt gamma peak in the  $TOF$  spectrum as shown in the insets of Fig. 31. By adding flight path uncertainties  $\Delta L$  it is possible to estimate the overall energy resolution as function of neutron energy. The results for the LTND and PSND modules are presented in Fig. 31.



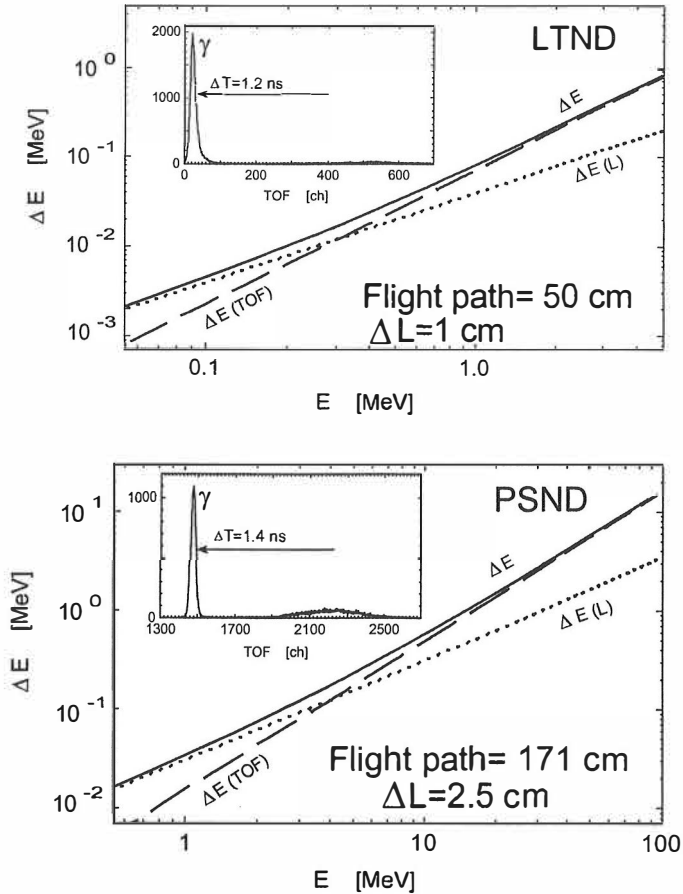


Figure 31. Energy uncertainty of the time-of-flight (LTND and PSND) neutron modules. Note different sources of uncertainties. The dashed line stands for the time uncertainty, the dotted line for the pathlength uncertainty and the solid line for the overall error. The insets represent  $\Delta T$  (FWHM) of the prompt gamma peak in the TOF spectrum measured by the  $^{252}\text{Cf}$  source.

## 5. Experimental arrangements

### 5.1 HENDES

Since a large part of measurements involved in this work has been done at HENDES, I will start here with a general description of this facility. HENDES (High Efficiency Neutron DEtection System [Trz97]), is a multi-detector array for correlation measurements of fission-fragments and light particles produced in nuclear reactions.

The whole set-up is updated all the time as one takes advantage of new technologies. Inside the 2 mm thin stainless steel spherical chamber of 80 cm diameter, there are, about 3 cm from the target, one or two MCP trigger detectors followed, at about 24 cm, by two large Position Sensitive Avalanche Counters (PSAC). As very fast devices MCP trigger detectors provide reference for all other time-of-flight detectors (PSND, PSAC, LCP etc.). When two MCP trigger detectors are used they are placed on opposite sides of the target, each in front of the corresponding PSAC. Presence of a fast coincidence between the two PSACs and at least one of the start detectors is a usually required trigger condition for correlation measurements. The remaining space inside the chamber is taken by various LCP detectors, mostly PIN diodes but also, depending on the application, by Si(Li) detectors, CsI(Tl) scintillators, proportional counters etc. as shown in Fig. 32.

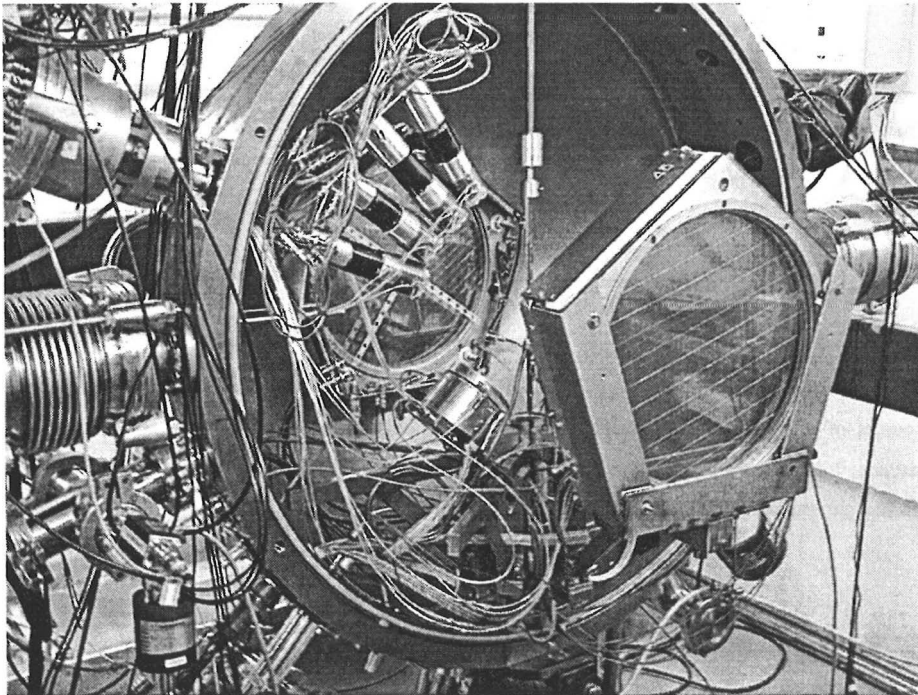


Figure 32. HENDES multi detector array for correlation measurements of fission fragments and light particles.

HENDES is very well suited for efficient measurements of fission fragment mass distributions, correlated light charged particles (LCP) and neutrons. Therefore, first part of measurements for determination of absolute cross-section in fast neutron induced fission of  $^{238}\text{U}$ , was performed at HENDES facility. To measure fission-

fragment mass distribution in coincidence with the LCP and neutrons two large PSACs, single MCP start detector, two PSNDs and two LANCERs neutron detectors were used. Two LANCER modules were placed in the forward direction, the PSND behind the PSAC and at the backward angle as shown in Fig. 33. The neutron modules all together (PSNDs+LANCERs) covered 4% of  $4\pi$  solid angle.

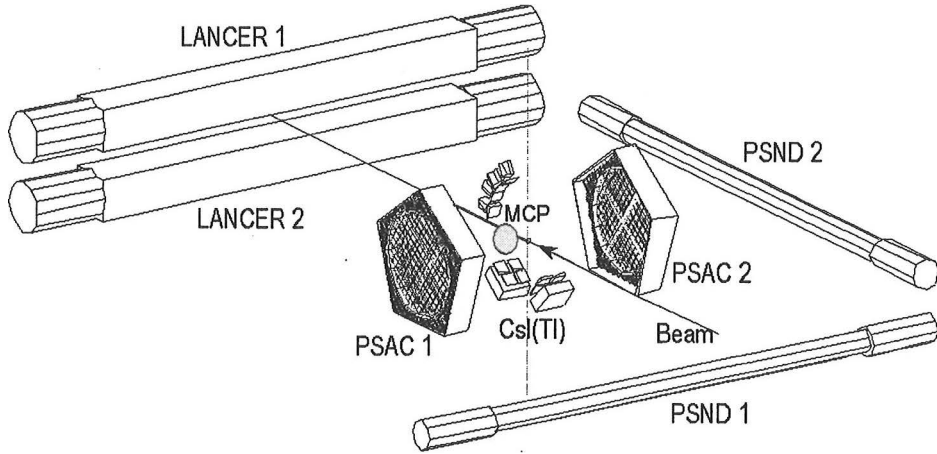


Figure 33. Experimental lay-out of HENDES  $d(p,f)$   $E_d = 65$  MeV experiment.

All neutron detectors have been located outside the chamber at about 65 cm from the target. The time-of-flight method was used both for neutron and fission fragment detection. The PSAC detectors [Ort93] have a diameter of 245 mm and provide a time resolution better than 400 ps and a position resolution below 1 mm as shown in Fig. 34. They were tuned to be insensitive to  $\alpha$ -particles. The MCP, with  $100 \mu\text{g}/\text{cm}^2$  thick gold plated mylar conversion foil and intrinsic time resolution of 55 ps, was placed in front of one of the PSAC detector. For both PSACs, the distance between cathode center and target was 235 mm. In-plane angles between the beam direction and the centers of the first and second PSAC were  $90^\circ$ . The angular acceptance of both detectors was  $56^\circ$  in-plane and  $\pm 28^\circ$  out-of-plane providing total geometrical efficiency of 10% of  $4\pi$ . The calibration spectra for PSAC detectors obtained by  $^{252}\text{Cf}$  source before the deuteron run are shown in Fig. 34. A detailed fission-fragment mass reconstruction procedure from the data obtained via *TOF* using PSAC detectors is described in Appendix 2.

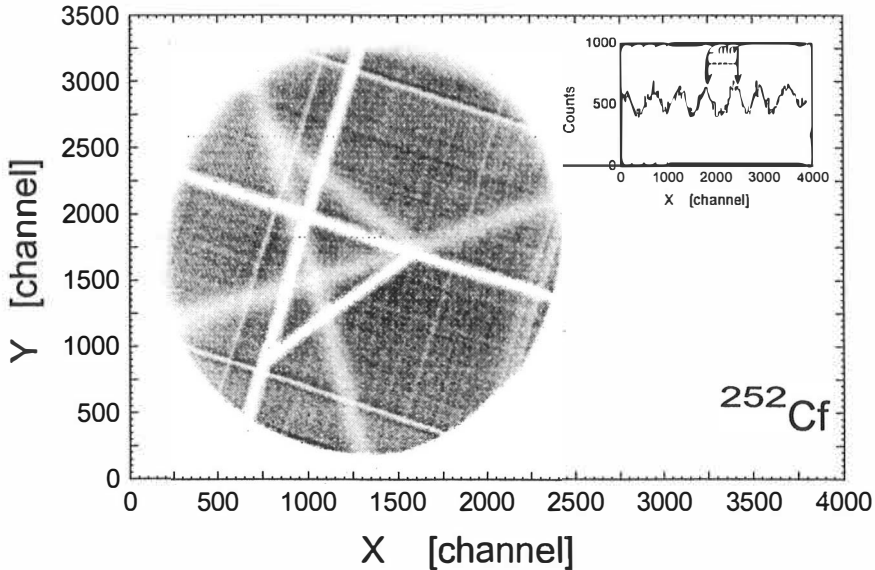


Figure 34. Position calibration of the PSAC's inner coordinate system by using  $^{252}\text{Cf}$  source. The correlation with the laboratory system is done by using the mask placed in front of the PSAC. Notice shadows caused by the mask. The inset shows shadows caused by inner structure of the thin wires placed at 2 mm distances inside of the PSAC.

Usually before the run the position calibration of the neutron detectors was done by moving in 10 cm long steps a collimated  $^{60}\text{Co}$   $\gamma$ -source along the length of the neutron modules. Neutron-gamma separation was performed with a standard pulse-shape technique. Threshold levels of neutron module electronics were adjusted to 0.8 MeV and 1.2 MeV for the PSND and the LANCER modules, respectively, to suppress high count rates induced by X and soft  $\gamma$ -rays. No collimators were used in the vicinity of the target chamber. The beam dump, 3.5 m from the target, was shielded by 20 cm of boron loaded paraffin and 25 cm of lead. The target was a  $150(10) \mu\text{g}/\text{cm}^2$  of  $^{238}\text{U}$  evaporated on  $60 \mu\text{g}/\text{cm}^2$  of  $\text{Al}_2\text{O}_3$  backing. Close to the target several CsI(Tl) telescopes with a total solid angle of 2.5% of  $4\pi$  for LCP detection were positioned. These covered angles from  $30^\circ$  to about  $140^\circ$  with respect to the beam and were located on the plane perpendicular to the direction between the centers of fission fragment detectors. Each telescope consisted of CsI(Tl) crystal working as  $E$  and a  $380 \mu\text{m}$  silicon PIN diode working as  $\Delta E$  and also providing the timing information. The CsI(Tl) crystals (diameter  $\phi = 2 \times 2$  cm cylinders) were optically coupled either to

photo multipliers or to light sensitive diodes. In each case it was possible to reach energy resolution close to 5% for  $^{226}\text{Ra}$  alpha-lines.

## 5.2 Set-up for neutron yield measurements

The second step in study of fast neutron induced fission was precise characterisation of the neutron yield produced in several combinations of thick targets, projectiles and bombarding energies. Therefore, in order to know the exact characteristics of the neutron flux impinging on the uranium target several experiments were performed. These experiments provided information about: absolute intensities, angular distributions and energy spectra of neutrons emitted from thick  $^{12,13}\text{C}$  and  $^9\text{Be}$  targets irradiated by deuteron (d) and proton (p) beams. Low (100 pA) intensity beams were focused into a target sufficiently thick to stop the beam. A cylindrical 14 mm thick, 50 mm diameter  $^9\text{Be}$  target was covered by a  $3.1\text{ mg/cm}^2$  aluminum foil to prevent chemical contamination from beryllium evaporation and sputtering. The  $^{12}\text{C}$  target (a 25 mm thick cylinder, 48 mm in diameter) was directly irradiated without any additional shielding. The  $^{13}\text{C}$  target was in powder form (6.5 g) and encapsulated in 1 mm thick cylindrical (18×35 mm) graphite container covered at the front surface with a thin ( $3\text{ mg/cm}^2$ ) aluminum foil. All targets were mounted on a 1.5 mm thin aluminum window at the end of a 10 cm long tube that was isolated from the rest of the beam line and served as a Faraday cup. Neutron energy was determined by the *TOF* technique where the start signal was taken from the different neutron detectors and stop from the cyclotron (RF) signal. The neutron flight path to the detector modules and the RF frequencies imposed the lower limit on the measurable neutron energy. The beam pulse width of about 2 ns was the main limiting factor in time resolution of the neutron detectors.

In order to optimize the energy resolution and measure neutron spectra with low energies, several separate experiments have been performed for each of the beam energies. For higher neutron energies (4-70 MeV), three PSNDs were placed at a distance of 171 cm from the target at different angles relative to the beam axis, as shown in Fig. 35(a). The low-energy parts of the spectra (0.3-10 MeV) were measured in a separate run by using three modules of the LTND positioned at the same angles as the PSND but closer to the target, as depicted in Fig. 35(b). A shorter neutron flight

path of 50 cm was chosen to observe the low-energy neutrons in the time window limited by the cyclotron RF frequency.

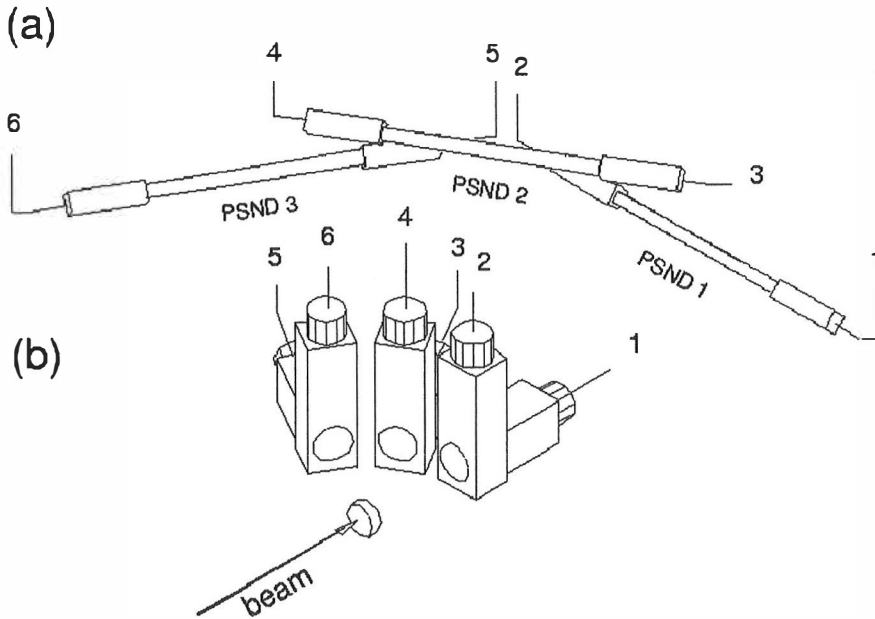


Figure 35. (a) Three modules of the Position Sensitive Neutron Detectors – PSND. (b) Three modules of the low-threshold neutron detectors – LTND placed closer to the neutron source (converter). The numbers marked are to help with electronic interconnection (see Fig. 44).

Therefore, the low energy cut-off limit was about 0.3 MeV for the LTND modules. In the case of plastic scintillator (LTND modules), only energy signals associated with the scintillator ( $E_T$ ) were recorded. Afterwards, in off-line analysis, both timing and energy in the appropriate range had to be present to provide an acceptable signal for the *TOF* spectra. The relative normalisation between different modules was performed using isotropic  $^{252}\text{Cf}$  neutron source. Position resolution of the PSND modules was sufficient to provide continuous coverage from  $0^\circ$  to  $60^\circ$  with about  $3^\circ$  angular resolution. The actual time resolutions (2.5 ns for the PSND and 2.2 ns for the LTND), were estimated by the width of the prompt gamma peaks in the *TOF* spectra. Moreover, by adding neutron flight-path uncertainties the relative error in neutron energy was estimated to be in the range of 11-20% for 10-70 MeV and 12-24% for 0.5-5 MeV for the PSND and LTND modules respectively. Neutron-gamma separation for the neutron modules were obtained by comparing the fast to the total

integrated PMs' output signals. More precisely, the sum of the signals from both PMs was taken into account to minimize the influence of the interaction point on the quality of n- $\gamma$  separation. The energy calibration of the total integrated signals was done using the  $^{137}\text{Cs}$  and  $^{60}\text{Co}$  gamma sources, i.e. the Compton edges of the deposited energies. The quality of separation of a PSND module is presented in Fig. 36.

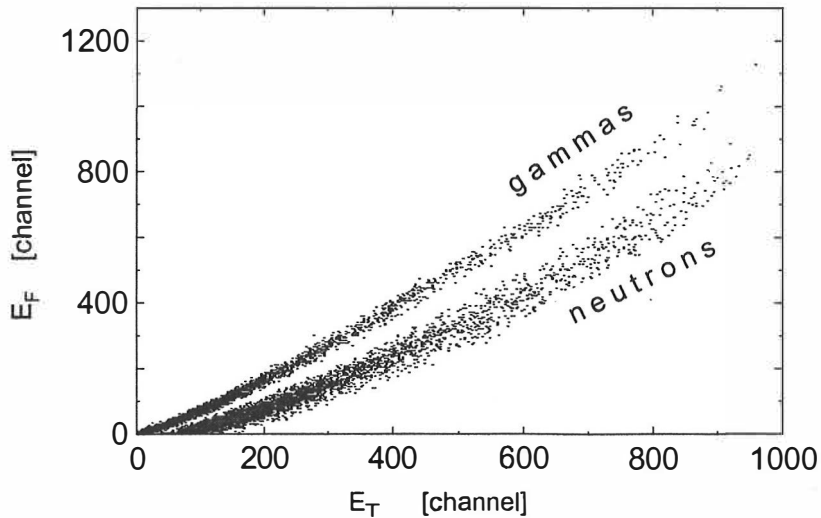


Figure 36. Neutron-gamma separation obtained by plotting fast versus total component of the signals from the central segment of the PSND, as measured in  $^{12}\text{C}(d,xn)$  reaction at  $E_d=50$  MeV.

### 5.3 IGISOL

The third step in studying of fast neutron induced fission was determination of the independent yields for mass separated nuclei using the IGISOL on-line mass separator and  $\gamma$ -ray spectroscopy. In the IGISOL (Ion Guided Isotope Separation On-Line) technique [Dend98, Pent97] the high energetic fission fragments are slowed down in the target (but can exit the thin target) and then thermalized in a high-pressure helium stopping chamber (see Fig. 37). Fission fragments leave the uranium target with kinetic energies of about 100 MeV. They enter the chamber filled with He, where they loose energy by collisions. Charge exchange reactions in the helium lower the charge state of fission products to a value of + 1. Fast flowing helium gas transports the fission products out of the chamber. By use of differential pumping and suitable

skimmer voltage, ions are guided to the acceleration electrode. Radioactive ions accelerated to 40 keV energy were mass-analysed with a resolving power of 350 and implanted into the collection tape. The tape was moved periodically in order to remove long-lived daughter activities.

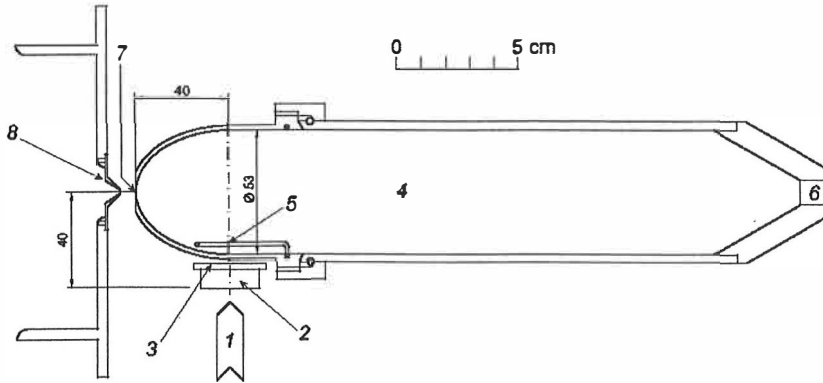


Figure 37. Helium chamber specially constructed for the experiment with fast neutrons at IGISOL in Jyväskylä (see ref. 4). The marked numbers indicate: 1. deuteron beam; 2.  $^{12}\text{C}$  converter; 3. 1.4 mm steel foil; 4. helium-filled ion guide target chamber; 5.  $15\text{ mg/cm}^2$ ,  $25\text{ mm} \times 25\text{ mm}$   $^{238}\text{U}$  target; 6. helium inlet; 7. exit-hole (1.2 mm); skimmer plate with 1.35 mm hole.

The IGISOL technique is one of the fastest mass separator systems with separation times of 1 ms. Due to the fact that primary thermalized ions are initially contained in and transported by inert helium gas and extracted by electric field, no chemical selectivity influences the transport. The set up for  $\gamma$ -ray spectroscopy at IGISOL consisted of a  $\beta$ TD detector surrounded by two large Ge detectors (a part of Nordball Ge detector array [Mos89]). The  $\gamma$ -rays were recorded in coincidence with betas detected by the  $\beta$ TD. Both timing and energy signals were taken from outputs of the  $\beta$ TD photomultiplier.



#### 5.4 Set-up for beta-delayed neutron spectroscopy

The LTND array was used together with a beta-trigger detector and two large Ge detectors for  $\gamma$ -ray spectroscopy for studying  $\beta$ -delayed neutrons of very neutron rich nuclei. In addition, two detectors were added for testing purposes to examine noise reduction possibilities by a small NE213 detector (SLND) and to extend the energy range of observable neutrons by using one module of new  ${}^6\text{Li}$ -glass detector. A schematic drawing of the whole set-up is presented in Fig. 38.

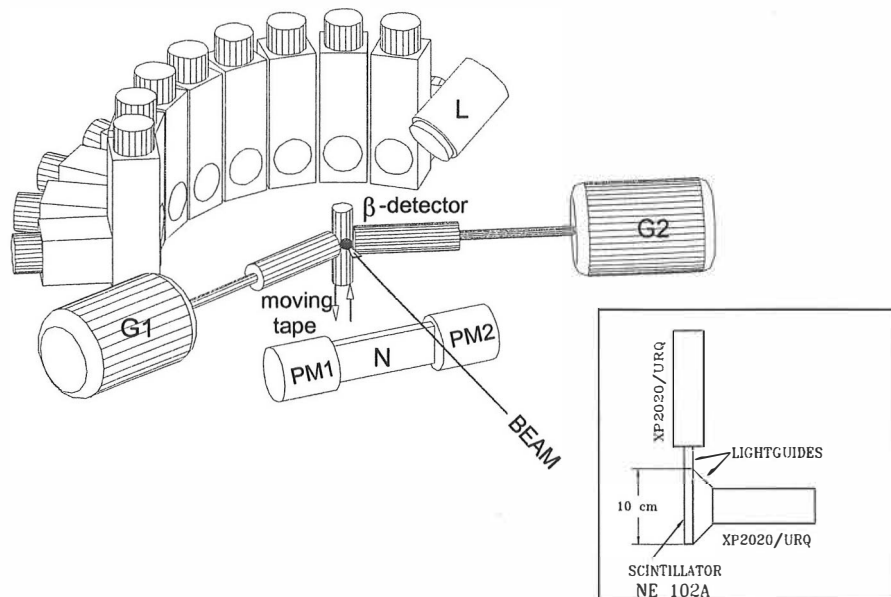


Figure 38. The detector set-up used at ISOLDE-CERN and IGISOL-Jyvaskylä in studying of the  $\beta$ -delayed neutron emission. The set-up consists of eight modules of neutron detectors with NE102A plastic scintillator, two Ge detectors (G1 and G2), one module of a neutron detector filled with NE213 liquid scintillator (N) and one module of  ${}^6\text{Li}$ -glass neutron detector (L). The implantation point is surrounded by a thin cylindrical  $\beta$ -detector constructed of BC408 plastic scintillator. The inset shows cross-section of the plastic scintillator detector module.

This set-up was used at two facilities: ISOLDE-CERN for studying of beta delayed neutron decay of  ${}^{33}\text{Na}$  and at IGISOL-Jyvaskylä for testing purposes by measuring beta-delayed neutron decay of mass separated isobars. At ISOLDE  ${}^{33}\text{Na}$  isotopes were induced by 1.4 GeV proton beam in an uranium carbide target. The beam was composed of high intensity pulses ( $3 \times 10^{13}$  protons/pulse) separated by an integer

multiple of 1.2 s. Average beam current in the target was typically 2  $\mu\text{A}$ . The separator beam was switched on for 20 ms, starting after each proton pulse and the data were collected during the following 550 ms period. The mass separated  $\text{Na}^+$  ions were collected onto an aluminized Mylar tape. The tape was moved periodically in order to remove the long-lived daughter activities. A typical yield for  $^{33}\text{Na}$  at the collection point was 2 ions/s. The implantation point was viewed by a beta-trigger detector. The beta detector was used as a main trigger for beta singles, beta-gamma ( $\beta-\gamma$ ), beta-neutron ( $\beta-n$ ) and beta-gamma-neutron ( $\beta-\gamma-n$ ) coincidences. The signals for triggering were accepted only if both timing and energy in a certain energy range were present at the same time, providing additional cleaning of all spectra in coincidence with betas. Two large-volume Ge detectors (70%) were used to measure  $\gamma$ -ray spectra. For time-of-flight neutron spectroscopy, eight low-threshold neutron detectors (LTND), were placed at a 50.8 cm distance from the source at different angles covering a total solid angle of  $\Omega_A=1.92\%$  of  $4\pi$ . The neutron *TOF* spectra were independently matched by adjusting the delay of each module and combined into one final *TOF* spectrum.

### 5.5 On-line calibration with well-known neutron sources $^{94,95}\text{Rb}$

The neutron detectors were checked and calibrated at IGISOL prior the data taking by using well-known neutron precursor  $^{94,95}\text{Rb}$ . At the same time these measurements served as tests of neutron *TOF* technique at IGISOL. Not only  $P_n$  and  $T_{1/2}$  but also neutron energy spectra of  $\beta$ -delayed neutrons were measured. Well-known  $^{94,95}\text{Rb}$  precursors were produced by bombarding a uranium target with a 25 MeV proton beam. The cross-sections for production of fission products around masses 94,95 as calculated by fission model simulation programme developed by V. Rubczenya [Rub98] are shown in Fig. 39. The typical  $\gamma$ -ray spectra attributed to mass 94, 95 are presented in Fig. 40(a,b). The yields achieved at the collection point were about 3000 and 1700 ions/s for  $^{94}\text{Rb}$  and  $^{95}\text{Rb}$ , respectively.

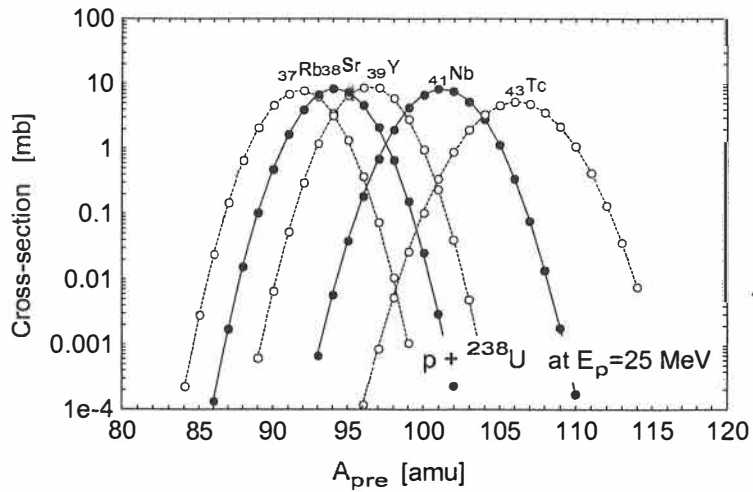


Figure 39. Independent isotope yields as calculated with the model developed by V. Rubchenya [7].

The measured time structure of the “cycle” for mass 95 is shown in Fig. 40(c) and represents both absolute beta and neutron activities observed in the run. The beta-trigger detector besides providing excellent timing properties was appropriately adjusted to minimise background and PM’s noise. An example of energy associated to the anode output is also shown in Fig. 40(d). The primary production of the strontium and yttrium isotopes (see Fig. 39) at mass 94,95 is not negligible when compared to the yield of  $^{94,95}\text{Rb}$ , but in this mass region the  $^{94,95}\text{Rb}$  are the only prominent short-lived neutron emitters. Furthermore, the  $\beta$ -decay daughters  $^{93,94}\text{Sr}$  are long-lived isotopes without any neutron emission, which made the unfolding of the activities trivial. Table 2 represents the literature reported half-life and  $P_n$  values [ToI98] as well as the coefficients proportional to the relative  $\beta$ -activities for two selected masses (94,95) as calculated by V. Rubchenya fission model [Rub98].

Isotope\mass	$T_{1/2}$ [s]		Rel. $\beta$ -activity [%]		$P_n$ [%]	
	A=94	A=95	A=94	A=95	A=94	A=95
Rb	2.72	0.337	85	47	10.4	8.7
Sr	75.3	23.9	14	52	0	0
Y	1122	618	1	1	0	0

Table 2. Important physical properties for the  $\beta$ -delayed neutron spectra around of two selected masses (94,95) at IGISOL.

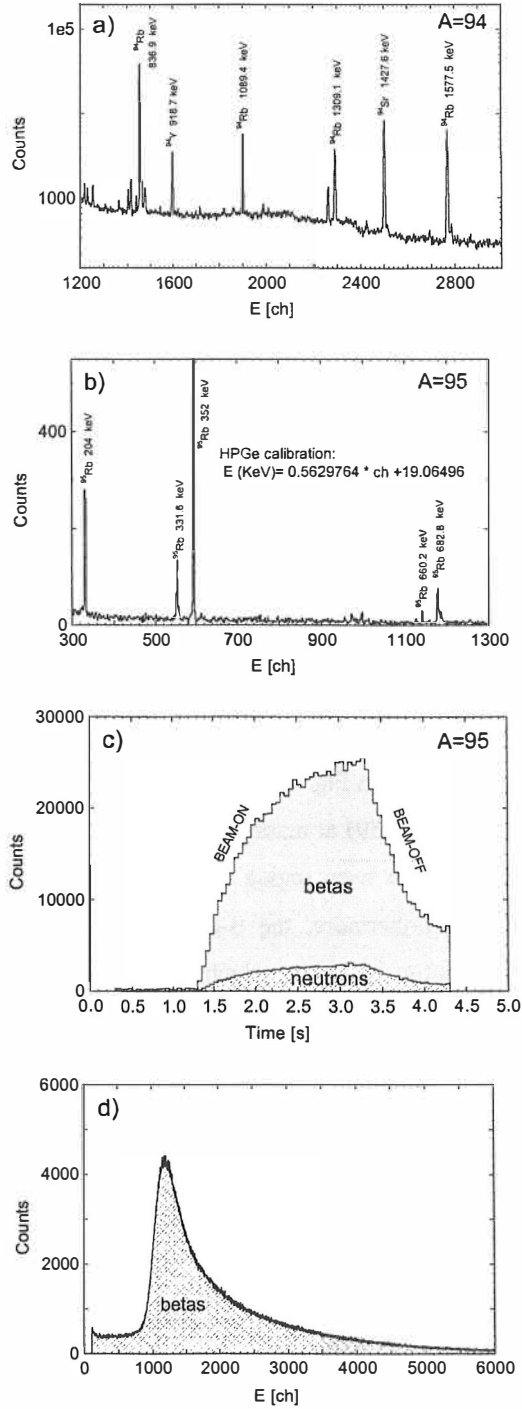


Figure 40. The part (a,b) represent beta-gated  $\gamma$ -ray spectra at masses  $A=94,95$  where the characteristic activities observed are denoted by their chemical symbol. (c) The cycle spectrum for both beta and neutron activities recorded at mass  $A=95$ . (d) The energy distribution associated to electrons and measured using the beta-trigger detector.

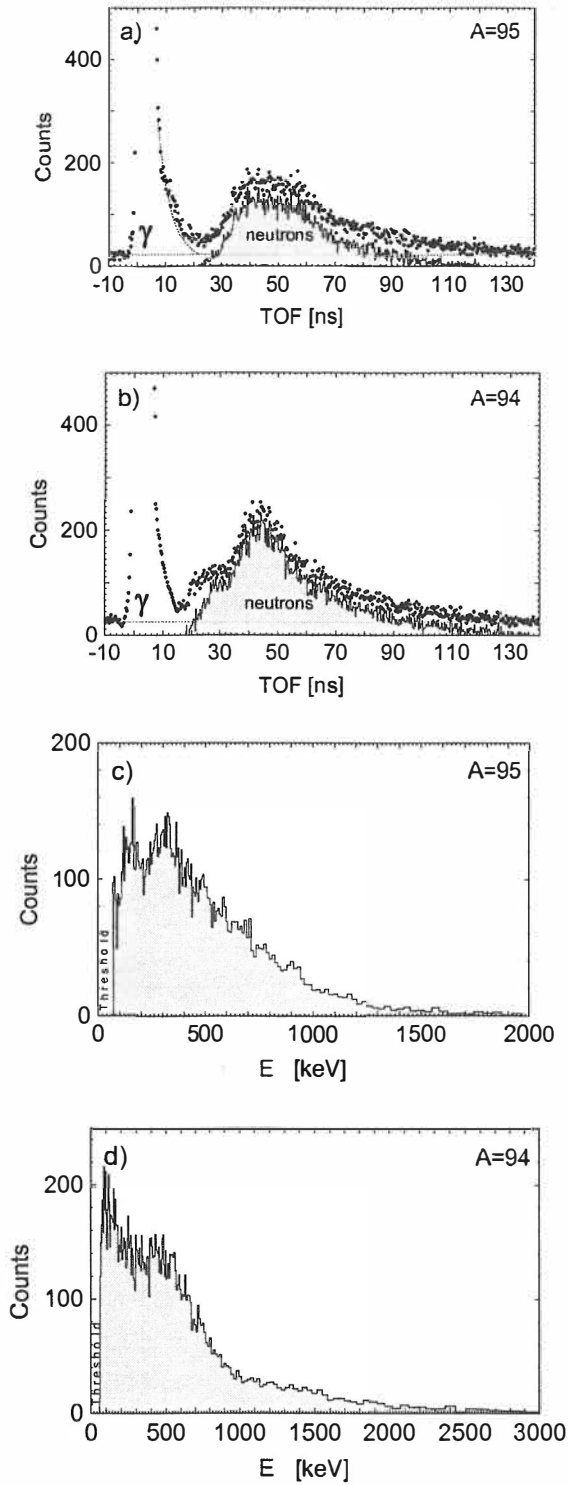


Figure 41. Beta-delayed neutron *TOF* and energy spectra observed in decay of  $^{94,95}\text{Rb}$ .

In Fig. 41 the measured *TOF* and neutron energy spectra are shown. Before converting into the energy spectra the *TOF* spectra (see Fig. 41 a,b) have been corrected for accidental background (dotted-lines) and then converted into energy as shown in Fig. 41 (c,d). Almost all neutron intensity is seen below 2 MeV although full energy ranges are 3.6 MeV and 4.9 MeV for neutron emission from  $^{94}\text{Sr}$  and  $^{95}\text{Sr}$ , respectively. Furthermore, both spectra exhibit fluctuation pattern due to many excited emitting levels. This is due to very high-density of the emitting levels and extremely high-resolution of a neutron spectrometer is demanded. The energy resolution in our *TOF* spectra was about 6 keV for 100 keV and about 0.1 MeV for 1 MeV neutrons.

Apart from the fact that the energy range up to about 60 keV was not covered, the observed neutron spectra quite similar pattern as measured by using  $^3\text{He}$  ionisation chambers [Kra81]. Some of the sharp peaks in the  $\beta$ -delayed neutron energy spectra have not been resolved but the envelopes are very much the same, which presents an additional affirmation for the detector intrinsic efficiency evaluation.

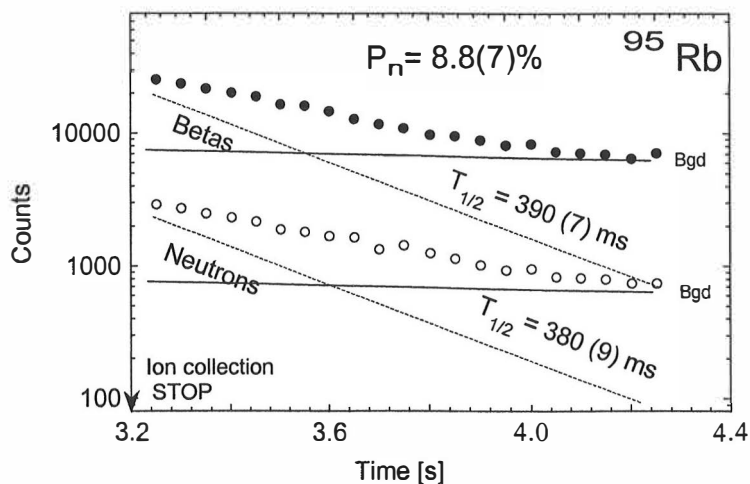


Figure 42. Decay curves of beta and neutron activities after ion collection stop. The dots represent measured data for beta (filled dots) and neutron activity (open-dots) corrected for intrinsic efficiency of the LTND modules. The dashed lines relate to beta and neutron activity and the solid lines stand for an almost uniform long-lived background (Bgd).

Besides the energy measurements of the  $\beta$ -delayed neutrons the obtained data provided also information about half-life and  $P_n$  values by direct measurements of absolute beta and neutron activities. The method used for unfolding of the activities

was the same but much simpler than in case of  $^{33}\text{Na}$  decay (see chapter 6.2). The results are displayed in Fig. 42. Based on measured data beta-strength function  $S_\beta$  was calculated by using the algorithm and programs developed and described in ref. [Pop99]. The input for the program is the measured beta-delayed neutron energy spectrum, which also contains the data-base of the energy levels and branching ratios in the decay of emitting nucleus  $^{95}\text{Sr}$ . This information is enough to calculate the neutron transmission coefficients  $T_l$  and relevant gamma-widths and then corresponding  $I_\beta$  and  $S_\beta$  functions (see Appendix 1). Finally, experimental  $\beta$ -strength function for  $^{95}\text{Rb}$  precursor was obtained and is displayed in Fig. 43 together with partial neutron probabilities to the excited levels of  $^{94}\text{Sr}$ . Furthermore, an integration over the whole energy range (from  $S_{1n}$  to  $Q_\beta$ ) yielded a calculated value of  $P_n=9.6(9)\%$  for total neutron emission probability.

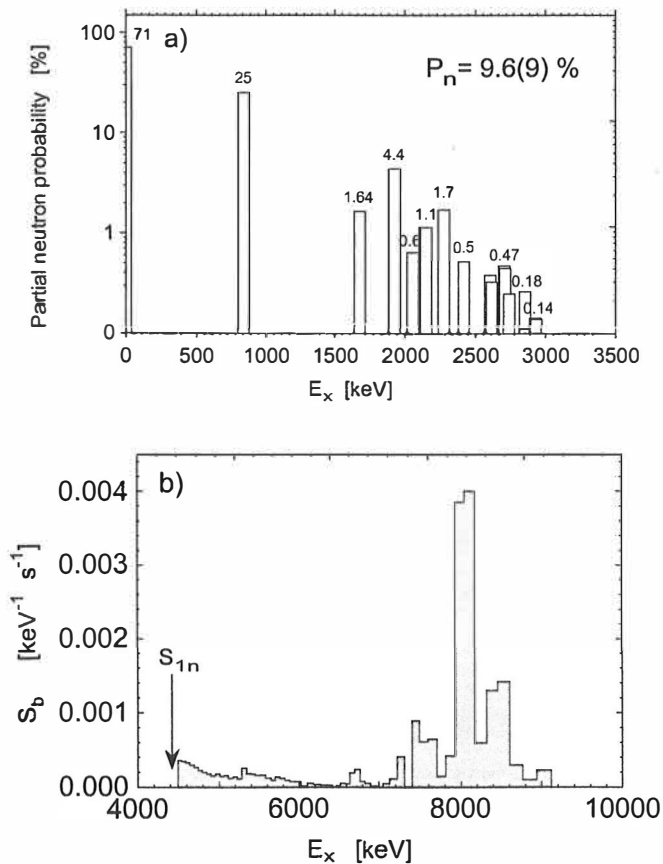


Figure 43. (a) Partial neutron probabilities and (b) beta strength function of  $^{95}\text{Rb}$  decay derived from experimental data. The  $E_x$  scale stands for excitation energy.

The weighted average of two measurements based on beta and neutron spectroscopy resulted in a value of 385(8) ms for the half-life of  $^{95}\text{Rb}$ . Furthermore, direct measurements of the total probability for neutron emission yielded a value of  $P_n=8.8(7)\%$ , which is in good agreement with the reported one (8.7%) [Kra81] and the previously calculated one 9.6(9)% (see Fig. 43(a)). These well-reproduced results indicate that neutron detector properties as well as techniques for the data analysis are consistent with the techniques based on  $\gamma$ -ray measurements.

## 5.6 Data acquisition system

In all the experiments electronics scheme similar to that displayed in Fig. 44 was used with standard CAMAC and NIM units. When measuring fission-fragments in coincidence with light particles at the HENDES beta and gamma detectors were not used. However, beta, gamma and neutron detectors were employed at the ISOLDE and IGISOL facilities. Finally, in measurements of absolute neutron yields only neutron modules and RF signals were used.

Two electronic units have been designed and built by the HENDES group. The first one is Master Trigger Unit (MTU), which processes logical signals and allows almost arbitrary logical combination for triggering of the Data Acquisition System (DAQ) depending on the specific experiment. For example, in the case of  $^{238}\text{U}(d,pf)$  run the logical condition at the MTU was set so that the DAQ stores the data only if three fast time signals, two from the PSACs and one from the MCP were present at the same time.

The second developed unit is the Signal Processor Block (SP), especially designed to process anode signals from the neutron modules and to perform neutron-gamma discrimination by charge comparison method. The SP unit occupies one standard CAMAC slot. Eight SP units were constructed to supply signal processing from 8 neutron modules. Each SP unit has two channels or more precisely includes two constant fraction discriminators and two pulse-shape analysis circuits similar to those described in ref. [Tök93]. These analogue pulse-shape schemes allow avoiding multiple gates, which are usually needed for particle identification in liquid scintillators. The resulting signals are digitised by fast multi-channel TDCs, QDCs



producing timing information ( $t_1, t_2$ ), fast and total pulse components ( $E_{1,F}, E_{1,T}, E_{2,F}, E_{2,T}$ ).

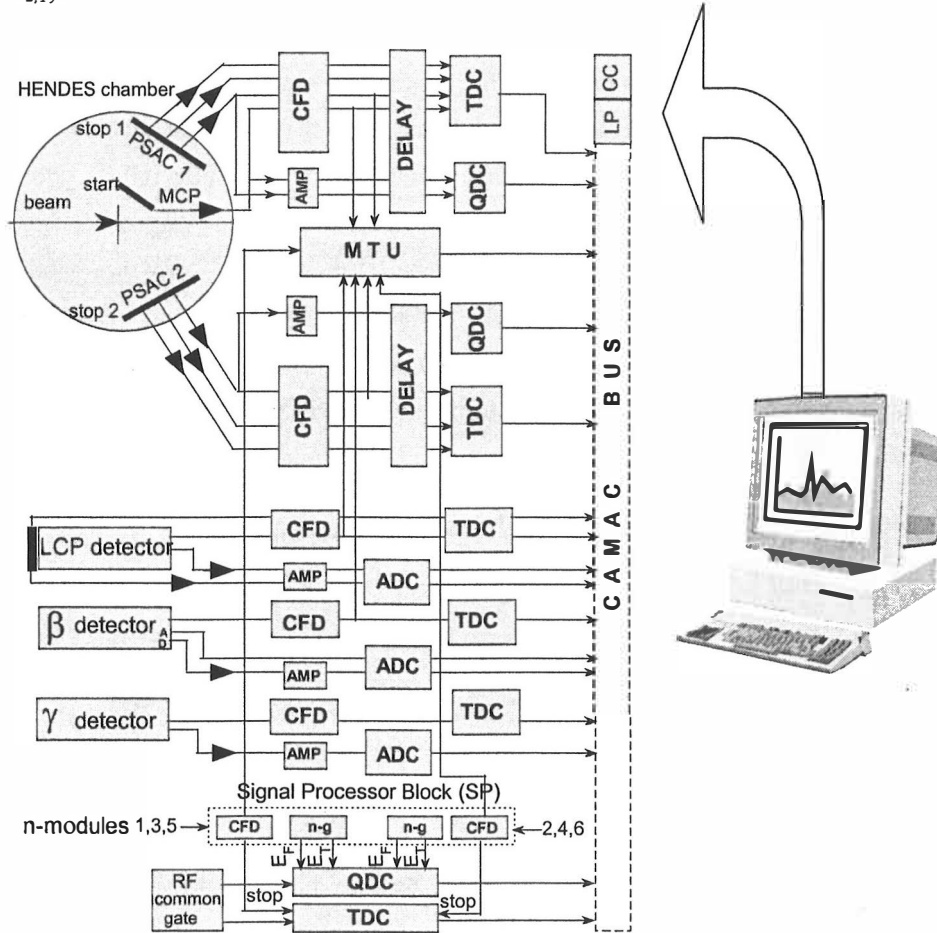


Figure 44. Electronics configuration of the Data Acquisition System used for experiments at several facilities. The bold triangles stands for preamplifiers.

In case of a multi-detector array, SP block's outputs can be plugged into QDCs triggered with Common Gate (see Fig. 44). This was done in absolute neutron yield measurements where RF signal was to be present to open the Common gate.

All modules of ADCs (Silena 4418A), TDCs (Ganelec 812F) and QDCs (LeCroy 4300B) are connected to the CAMAC bus, which is controlled by Crate Controller (CC) and List Processor LP (Hytec 1341) as shown in Fig. 44. The CC is connected to the computer (PC) via multiwire data-bus cable and controlled by DAQ software installed in the PC. The source of the DAQ software was written in C language and allows changes specific for given experimental conditions to be made easily.

Instead of checking and reading each electronics module into the CAMAC crate, the PC loads the list of modules and program of readout into LP via CC. When MTU unit issues a request, the LP takes control under CAMAC bus allowing fast readout of modules and writes data into internal buffer which has a capacity up to 256 kb. When the LP memory buffer is full, the data are transmitted to the PC to be saved into a file on hard-disc. As a result of zero-suppression mode the recorded data in binary form have very compact size suitable for transportation and analysing at different laboratories. Besides conventional spectroscopic channels each event has another helpful parameter. Since real time of each event is registered it is possible to estimate the time difference between two neighbouring events. Deviation from the exponential law (Poisson statistics) has been used to estimate the dead-time of the DAQ system.

## **6. Experimental results**

The measurements in the present work were done at several facilities. The experiments at HENDES concentrated on measurements of absolute neutron yields and fission fragment (FF) mass distributions by means of correlated measurements of the FF and light particles. The corresponding charge distributions were obtained at IGISOL by conventional  $\gamma$ -ray spectroscopy. Finally, neutron spectroscopy of n-rich nuclei was performed at ISOLDE and IGISOL by a combination of both light particle and  $\gamma$ -ray spectroscopy techniques.

### **6.1 Neutron yields from thick targets and fast-neutron induced fission of $^{238}\text{U}$**

The first step in the study of fast neutron induced fission as a primary reaction mechanism for production of n-rich nuclei was precise characterisation of neutron field emerging from thick targets. The second step was measurement of mass distribution of fission fragments in fast neutron induced fission by taking advantage of  $^{238}\text{U}(\text{d},\text{pf})$  reaction. The last step involved measurements of isobaric yields of mass separated ions. This set of the measurements allowed determination of absolute cross-sections in fast neutron induced fission of  $^{238}\text{U}$ .

### 6.1.1. Neutron energy spectra and yields

There are several processes where neutrons may be produced when a target is bombarded by high-energy deuterons, therefore the shapes of the angular and energy distributions are a result of competition between different reaction channels leading to neutron emission. The most probable reactions and their  $Q$ -values are shown in Table 3.

Reaction	Q-value on ${}^9\text{Be}$ [MeV]	Q-value on ${}^{12}\text{C}$ [MeV]
(d,n)	4.36	-0.28
(d, $\alpha$ n)	-0.10	-9.78
(d,dn)	-1.67	-18.72
(d,pn)	-2.22	-2.22
(d,p2n)	-3.89	-20.95
(d,2n)	-4.07	-20.34
(d,3n)	-22.65	-36.38
(d,p3n)	-22.79	-34.07
(d,4n)	-35.67	

Table 3. Expected reaction channels for primary deuteron projectiles and their  $Q$ -values for carbon and beryllium targets.

In Fig. 45 two-dimensional energy versus angle contour-plots of neutron spectra for two targets are shown. As expected, both cases show a concentration of yield at forward angles. At larger angles the angle-energy correlation becomes more linear. The contour lines for lower energies are nearly parallel to the angle axis indicating an almost isotropic evaporation source.

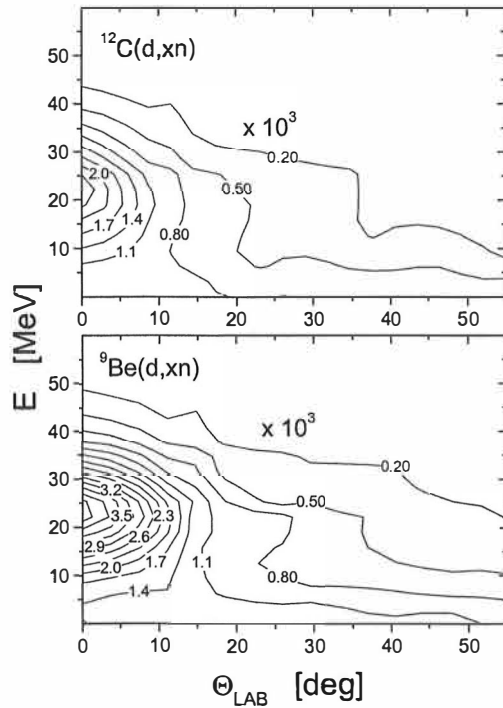


Figure 45. Diagram of constant yield versus neutron energy and laboratory angle for the  $^{12}\text{C}(d,xn)$  at  $E_d=50$  MeV and  $^9\text{Be}(d,xn)$  at  $E_d=65$  MeV reactions. The numbers at the contour lines indicate yield in neutron per steradian per MeV per deuteron multiplied by a factor of  $10^3$ .

The energy spectra of neutrons emerging from thick  $^{12}\text{C}$  and  $^9\text{Be}$  targets at different angles are displayed in Fig. 46. It is possible to see two regions of interest: the first connected with low-energy part up to 5 MeV which corresponds mainly to neutrons emitted from the target-like source, and the second high-energy part produced by the projectile break-up.

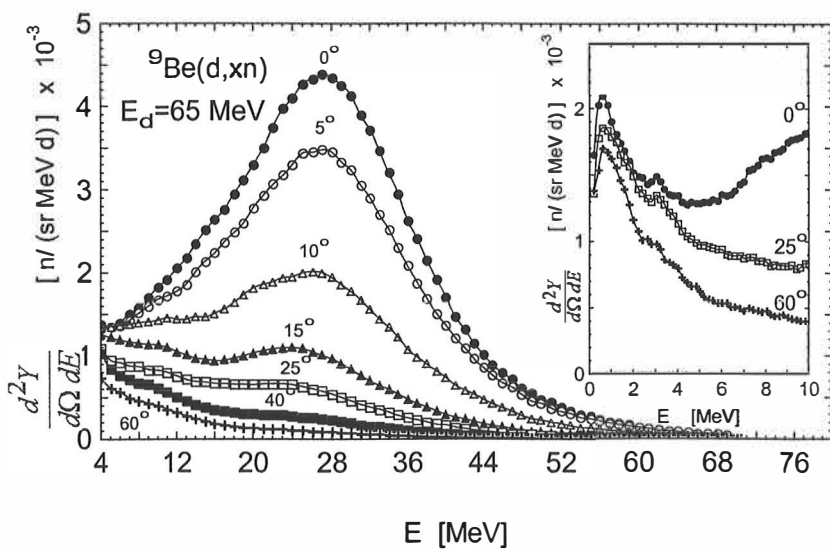
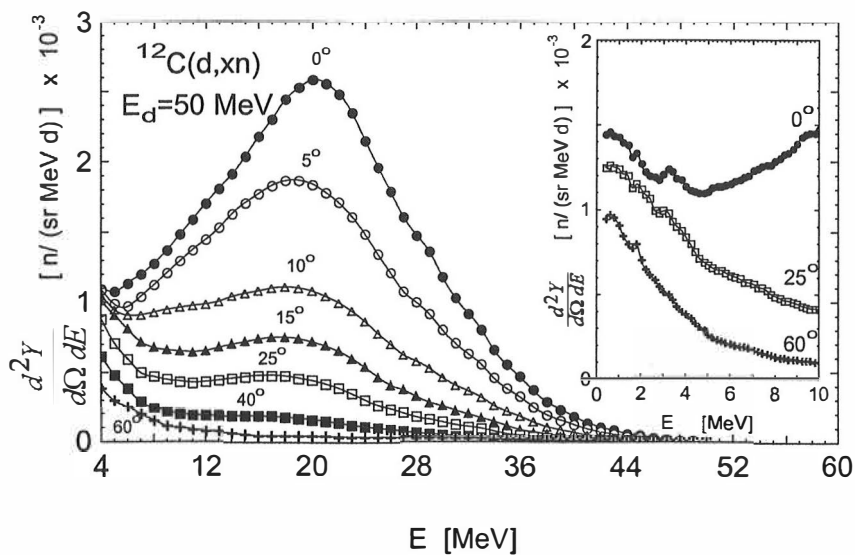


Figure 46. Double differential neutron yields  $d^2Y(E, \theta)/dEd\Omega$  produced in reactions on thick  $^{12}\text{C}$  and  $^9\text{Be}$  targets for different angles as a function of neutron energy. The insets show blow-up of low-energy part of the neutron spectra measured by using the LTND modules. The solid lines are only for guiding the eye.

At higher energies and at small forward angles ( $<15^\circ$ ) one can see well-pronounced bell-like shapes. These neutrons emerging in narrow forward-cones are from direct reactions (stripping and break-up) [Ser47,Rid99]. The neutrons from the direct reaction mechanism are still visible at larger angles ( $40^\circ$ ). However, the relative intensity and the position of the maxima decrease with angle. The most probable

energy of neutrons from the stripping reaction is equal to approximately one half of the incident deuteron energy corrected for the Coulomb barrier and the energy loss in the target prior to the reaction. The observed average energy of the neutron spectra is at about 0.4 times the deuteron energy, which is also the case in other measurements at higher energies [Pau00]. The energy maxima of the bell-like neutron groups at different angles are presented in Table 4.

$\theta_{\text{LAB}}$ [°]	${}^9\text{Be(d,xn)}$ at 65 MeV		${}^{12}\text{C(d,xn)}$ at 50 MeV		${}^{13}\text{C(p,xn)}$ at 30 MeV
	$dY/d\Omega$ [n sr <sup>-1</sup> d <sup>-1</sup> ]	$E_n$ [MeV]	$dY/d\Omega$ [n sr <sup>-1</sup> d <sup>-1</sup> ]	$E_n$ [MeV]	$dY/d\Omega$ [n sr <sup>-1</sup> d <sup>-1</sup> ]
0	0.125(10)	26.7(9)	0.068(7)	20.4(7)	0.0112(4)
5	0.099(9)	26.0(8)	0.050(5)	19.5(7)	0.0114(4)
10	0.071(7)	23.6(8)	0.031(4)	18.3(6)	0.0115(4)
15	0.045(4)	21.5(8)	0.021(3)	17.1(6)	0.0112(4)
25	0.024(3)	19.6(7)	0.014(1)	16.5(5)	0.0101(3)
40	0.015(1)	16.5(5)	0.0081(8)	14.0(4)	0.0093(3)
60	0.0085(9)	13.6(4)	0.0042(4)	12.4(3)	0.0083(2)

Table 4. Differential yields  $dY/d\Omega$  at different angles for three target projectile combinations. For the reactions with deuteron beam the position of the energy maxima for bell-like shapes in neutron energy spectra are also given. All angles ( $\theta_{\text{LAB}}$ ) are in the laboratory system relative to the beam axis.

The asymmetry of the bell-like shapes corresponds mainly to folding of the thick target and multiple scattering effects before the direct reaction processes take place [Ser47]. Rutherford scattering causes also deflection from the incident deuteron direction and broadening of the angular distribution of the neutrons emerging from the direct reactions.

The insets in Fig. 46 present extensions of the neutron spectra to low-energies. This part is dominated by the emission (evaporation) of low-energy neutrons from the excited target-like nuclei and yielded almost isotropic angular distributions for neutrons. For example, in the case of the Be target, the relatively sharp increase at about 0.67 MeV, is due to the decay of the 2.43 MeV excited state in  ${}^9\text{B}^*$  to the ground state of  ${}^8\text{Be}$ , where  ${}^9\text{Be}^*$  are populated by inelastic scattering  ${}^9\text{Be(d,d')}{}^9\text{Be}^*$  of the deuterons [Bre89].

In both of the neutron production reactions using deuteron beams the dominant mechanism is deuteron break-up. Fig. 47 presents neutron energy spectra produced in the  ${}^{13}\text{C(p,xn)}$  reaction at  $E_p = 30$  MeV where the main part of the spectra are neutrons

emitted from excited states of  $^{14}\text{N}$ . The threshold for populating the first excited state is at  $E_p = 5.8$  MeV and all excited states in  $^{14}\text{N}$  are unstable against particle emission. More precisely, the spectra are a result of the composition of different sources of neutron emission. The low-energy component corresponds to the evaporation process and the high-energy component is a mixture between pre-equilibrium emission and direct reactions. Broadened neutron group labelled with D corresponds to ground state neutrons ( $E_n \sim 7.7$  MeV). The neutron groups leading to the first and the second excited state ( $E_n \sim 5.4$  and  $E_n \sim 4.3$  MeV) are labelled with C and B letters, respectively. The neutrons emitted from high-excited states in decay of  $^{14}\text{N}$  are marked with letter A and present a large contribution in total neutron yield. Finally, the bump labelled with E presents mixture between pre-equilibrium emitted neutrons and from direct reactions where the most probable energy is centred at about half of the projectile energy. The magnitude of the bump and its most probable energy decrease with increasing emission angle. This shows that the primary reaction process, leading to the bump-spectra is direct knock-out reaction but energetic pre-equilibrium neutrons are present as well.

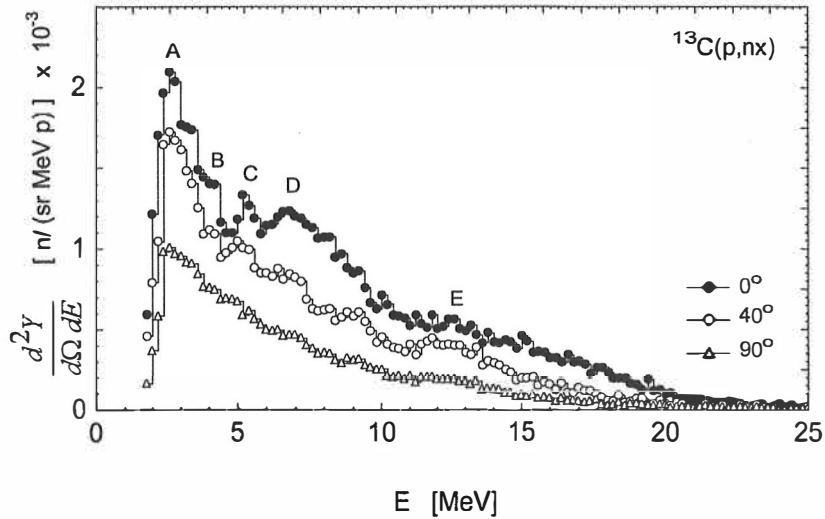


Figure 47. Double differential neutron yields  $d^2Y(E, \theta)/d\Omega dE$  produced in  $^{13}\text{C}(p, nx)$  at  $E_p = 30$  MeV reaction for different angles as a function of neutron energy.

The numeric data which summarizes the neutron yield angular dependence, are also presented in Table 4. They are obtained by integration of the double-differential

spectra ( $d^2Y(\theta, E)/d\Omega dE$ ) from the lowest (0.3 and 1.8 MeV for d and p beams, respectively) to the highest registered neutron energies. Energy integrated angular distributions of differential yields ( $dY/d\Omega$ ) are shown in Fig. 48. In the case of  ${}^9\text{Be}(d, xn)$  and  ${}^{12}\text{C}(d, xn)$  reactions, the decrease of the neutron flux with increasing angle is due to the drop of direct reaction contribution in the neutron spectra. The total neutron yield ( $Y$ ) has been extracted using a linear interpolation between the data points and assuming that  $(dY/d\Omega) \sin(\theta)$  drops linearly at angles larger than  $60^\circ$  until  $180^\circ$ . This resulted in a neutron yield of 0.109(10) [n/d] for  $d+{}^9\text{Be}$  at 65 MeV and 0.056(6) [n/d] for  $d+{}^{12}\text{C}$  at 50 MeV reactions, respectively.

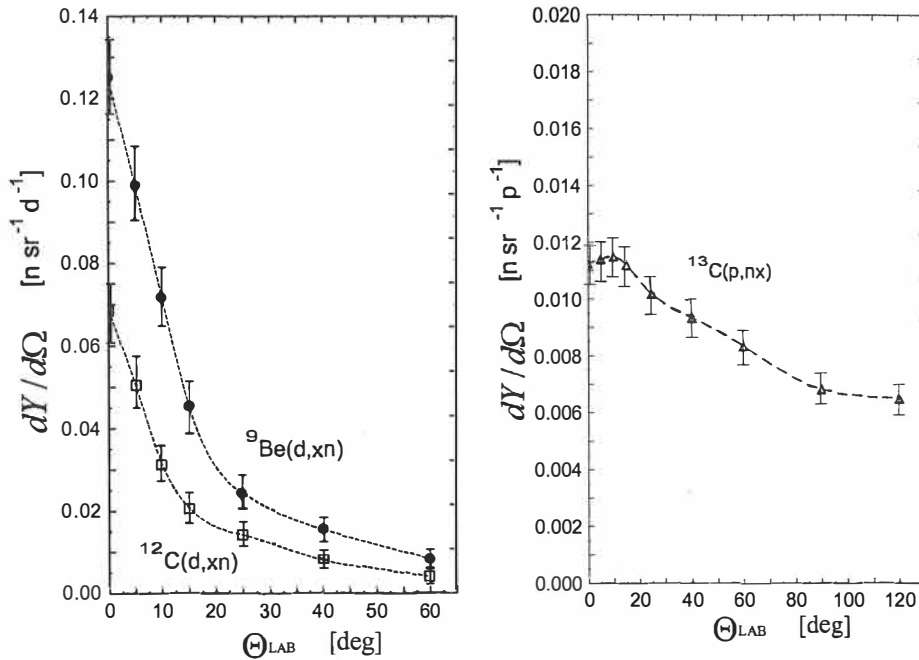


Figure 48. Left: Angular distribution of neutrons from  ${}^{12}\text{C}(d, xn)$  at 50 MeV and  ${}^9\text{Be}(d, xn)$  at 65 MeV reactions. Right: Angular distribution of neutrons from  ${}^{13}\text{C}(p, xn)$  at 30 MeV.

The angular distribution of differential yields ( $dY/d\Omega$ ) from the  ${}^{13}\text{C}(p, xn)$  reaction is also shown in Fig. 48. The total neutron yield ( $Y$ ) observed is 0.022(3) [n/p] with a slight angular anisotropy. A slight forward-peaking is probably due to direct interaction between the incoming proton and a neutron on the surface of the  ${}^{13}\text{C}$  nucleus and because of neutrons emitted from the hot pre-equilibrium states since they occur in a more forward direction.

In Fig. 49 the neutron yield is shown as a function of the projectile beam energy. The measured yields using deuteron and proton beams on thick targets, present a new addition into the systematic of the absolute yields of neutron sources. The yield from



carbon is less than that from beryllium but carbon withstands higher temperatures and can be placed very close to the fission target (uraniumcarbide or metallic molten uranium) and covers higher solid angle for neutrons. The uranium target composition and design is very important for the success of the production of a RNB by fast neutron induced fission. It is clear that in the present target-converter (see Fig. 3) configuration, the forward peaking of the neutrons is a preferred feature of the conversion mechanism. Furthermore, several measurements indicate that a carbon converter is the best compromise in respect to the d/n conversion factor and engineering design considerations [Ibr00,Leb98].

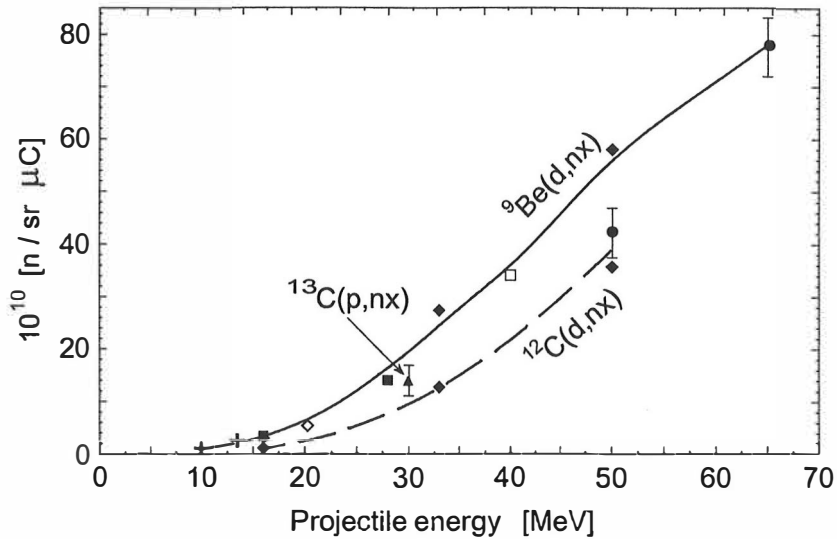


Figure 49. Neutron yields produced in thick  $^{12,13}\text{C}$  and  $^9\text{Be}$  targets measured at zero degrees. Crosses, solid squares, solid diamonds, open diamond and open square are data from refs. [Bre89,Wat79,Meu75,Bel98,Sal76], respectively. The solid circles and triangle with error bars are from this work

### 6.1.2 Mass and yield measurements in fast neutron induced fission of $^{238}\text{U}$

In the second step the  $^{238}\text{U}(d,pf)$  at  $E_d = 65$  MeV reaction was used to provide means for measurements of neutron induced fission at intermediate energies. The virtual neutron spectra have been obtained by gating proton energy spectra detected by CsI(Tl) telescopes in a certain energy window. It was done demanding coincidences between fission fragments and protons emitted under small solid angle in the forward direction where the protons from stripping reactions were measured. The proton spectra measured by telescopes at different angles are shown in Fig. 50. The spectrum

at  $30^\circ$  shows a bell-like shape characteristic of the stripping reaction with the maximum at about half of the bombarding energy (32 MeV). The spectra at larger angles and lower energies ( $< 20$  MeV) have a typical evaporation shape. The shape of the virtual neutron spectrum is determined by direct stripping and evaporation components. To select neutron energies in the virtual neutron spectrum equation (14) which connects  $E_n$ - neutron and  $E_p$ - proton energies where the protons are detected at angle  $\theta$  was used. The  $E_d$  and  $B_d$  are deuteron bombarding and binding energies, respectively.

$$E_n = E_d - B_d - E_p + 0.0954\sqrt{E_p} \cos(\theta). \quad (14)$$

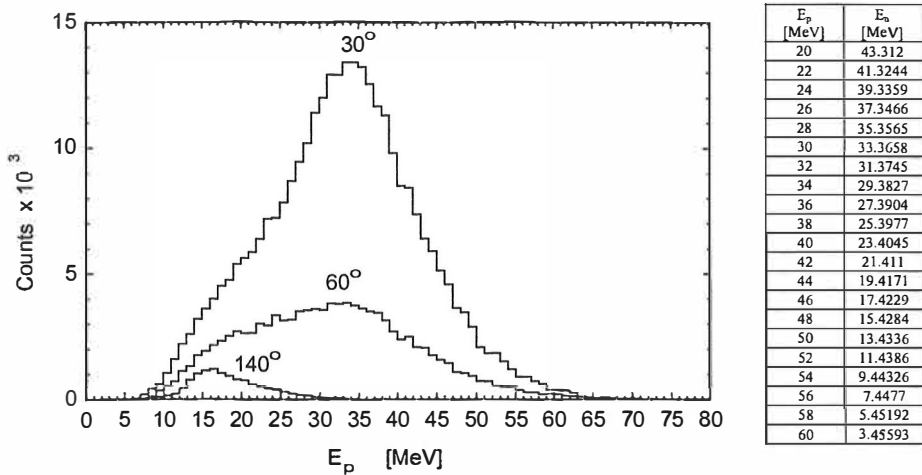


Figure 50. Energy spectra of protons from the  $^{238}\text{U}(d,pf)$  reaction measured at different angles in coincidence with fission fragments. Two columns at the right-side give corresponding proton and neutron energies.

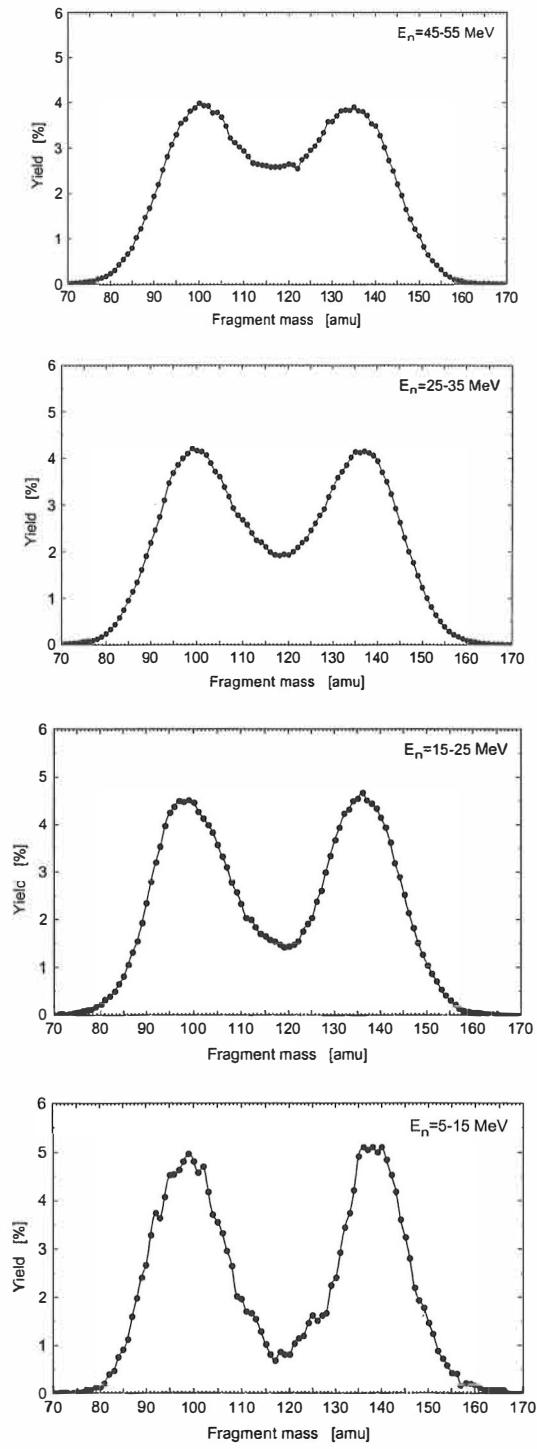


Figure 51. Fast neutron induced fission fragment mass distributions measured for the  $^{238}\text{U}(d,pf)$  reaction at several neutron bombarding energies.

Fission fragment mass distributions measured in the  $^{238}\text{U}(\text{d},\text{pf})$  reaction for different virtual fast-neutron energies are shown in Fig. 51. Different neutron energies are selected by gating the proton energy window in the telescope detector. Therefore, it was possible to reproduce mass distributions obtained in  $^{238}\text{U}(\text{n},\text{f})$  reaction for several bombarding neutron energies. The results are in good agreement with the data reported in ref. [Zöll95], where neutrons from the spallation source at Los Alamos National Laboratory were used.

### 6.1.3 Absolute cross-sections of fast neutron induced fission of $^{238}\text{U}$

Isotopic distributions of the fast-neutron induced fission on  $^{238}\text{U}$  using the IGISOL facility were measured in the third step. The neutrons produced in the thick  $^{12}\text{C}$  target by 50 MeV deuterons impinged on a uranium target ( $15 \text{ mg/cm}^2$ ) in the He chamber already shown in Fig. 37. The production yields of n-rich nuclei in the mass ranges 88-94 and 136-144 were measured. Examples of  $\beta$ -gated gamma spectra taken at several masses ( $A= 89,112,139$ ) are given in Fig. 52 where evidence of different isobars can be seen. In the first step, the characteristic experimental  $\gamma$ -peak areas were corrected for detection efficiency and decay branching in order to get the number of primary ions at the collection point.

Then another correction was made to account for the finite acquisition time and to get the beam intensities as a number of ions/s, the so-called independent yields. The independent yields were added to form cumulative yields. Finally, the cumulative yields were then normalized for a primary beam intensity of  $1 \mu\text{A}$ .

Combining these results with the known total cross-section (see Fig. 2) for fast neutron induced fission and with the results of mass distributions from the  $^{238}\text{U}(\text{d},\text{pf})$  reaction it was possible to estimate absolute cross-sections in fast-neutron induced fission of uranium. The data have been normalized according to ref. [Bab71] and very recent measurements done at the IGISOL [Num01]. The results are displayed in Fig. 53 together with earlier measurements using protons [7]. Furthermore, the measured values are compared with the model calculations described in detail in Appendix 3. An indication for consistency of the analysis is fairly smooth behaviour of the mass yields.

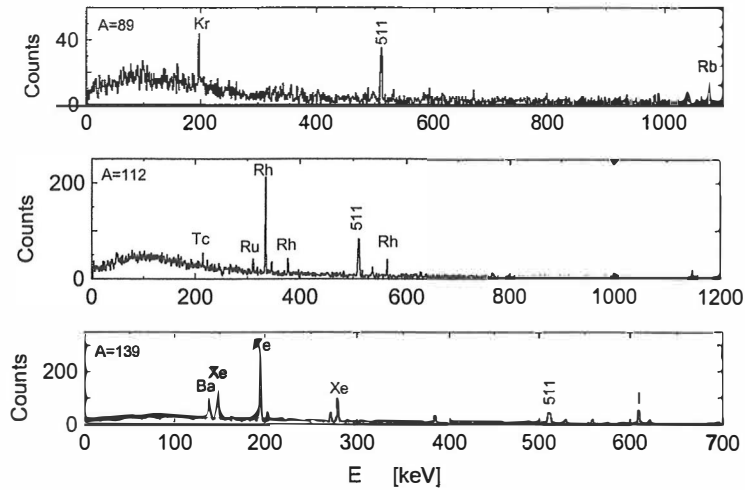


Figure 52. Beta gated gamma spectra in fast neutron induced fission of  $^{238}\text{U}$  experiment recorded for several masses at IGISOL facility. The activities observed are denoted by their chemical symbol.

The observed valley in the symmetric region with a peak-to-valley ( $P/V$ ) ratio value, as expected, is much more shallow than for thermal-neutron induced fission of  $^{235}\text{U}$  where  $P/V$  is about 600 [Wah88]. The reported  $P/V$  value for fast neutron ( $E_n \approx 20$  MeV) induced fission at Los Alamos [Zöl95] is 3.5. However, the data obtained by HENDES showed a value of  $P/V = 2.8$ . A reason for different  $P/V$  values might be in the low-energy part of neutrons produced by thick converter when bombarded by deuterons. The inset in Fig. 46, shows an increase of the neutron flux at low energies. The rather isotropic distribution of these low-energy neutrons suggests another mechanism than stripping, possibly evaporation from the target nucleus.

Furthermore, the influence of low-energy neutrons is enhanced by use of a thick U target ( $15 \text{ mg/cm}^2$  in the present experiment), in which low-energy fission neutrons are produced and can further induce fission. Even a small amount of low-energy neutrons could increase the  $P/V$  ratio, which varies rapidly at this energy [Zöl95, Viv00].

Fission fragment charge distributions are conventionally described by Gaussians of width  $\sigma_z(A)$  and centered at the most probable charge  $Z_p(A)$ . Corresponding isobaric yield  $Y(A, Z)$  is given by the expression

$$Y(A, Z) = 1/\sqrt{2\pi}\sigma_z \exp(-0.5(Z - Z_p/\sigma_z)^2). \quad (15)$$

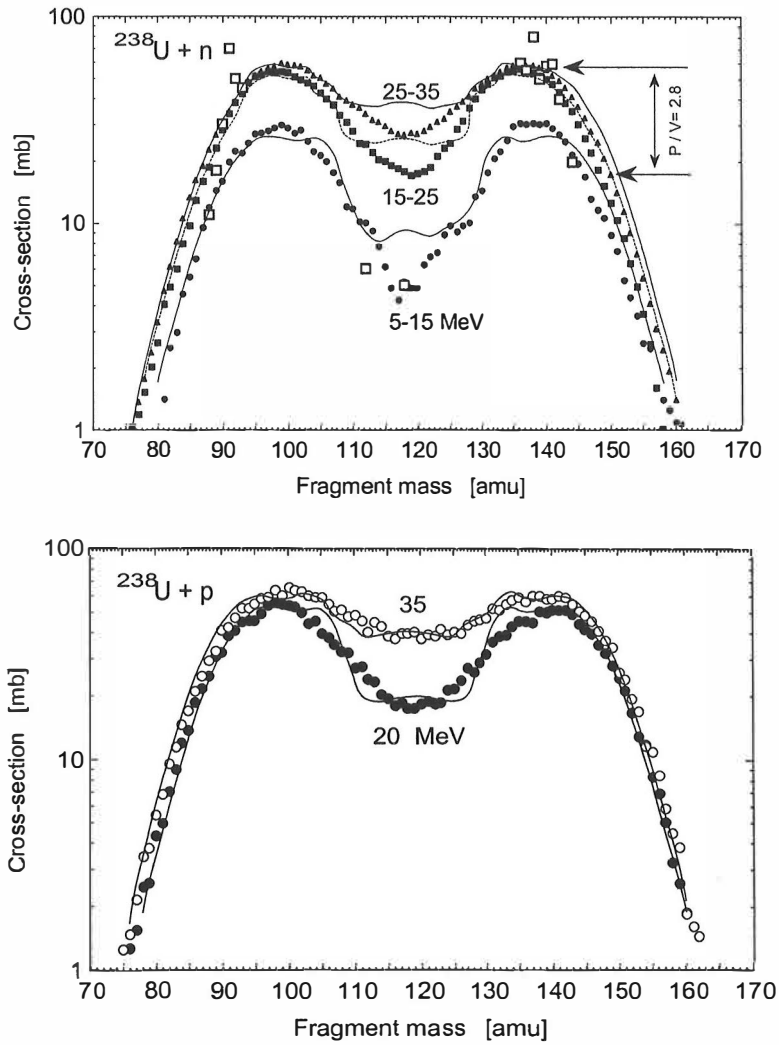


Figure 53. Top: Cross-sections of mass distributions in fast neutron induced fission of  $^{238}\text{U}$  for several average neutron energies as measured by HENDES (filled symbols) and IGISOL (open squares) facilities. Bottom: The same but obtained by proton beam for two energies (see ref. 7). In both figures lines represent results of calculations by V. Rubchenya's model [7].

Despite of large fluctuations it was possible to extract general trends by fitting the cumulative yields. The fitting procedure assumed several simplifications. It was possible to adopt the constant-charge-ratio (CCR) rule in such a way that the most probable charge  $Z_p(A)$  at each measured mass is defined by a simple linear equation  $Z_p(A) = aA + b$ . The fitting data analysis has been extensively explained in ref. [4]. The fit resulted in the best  $\sigma_z(A)$  value of 0.70 for neutron induced fission.

Furthermore, the obtained slope coefficient value ( $a$ ) for neutron induced fission is very close to the value obtained by using protons [Kud98]. The ( $a,b$ ) parameters for the fits of the whole data sets are (0.3662, 3.21) and (0.3670, 3.90) for neutron and proton induced fission, respectively. Very interesting is the offset difference which indicates a shift towards the most n-rich nuclei for neutron induced fission. This shift is stable with respect to large variations of other parameters, and represents an encouraging result for production of n-rich nuclei by fast neutron induced fission.

## 6.2 Beta-delayed neutron decay of $^{33}\text{Na}$

The study was performed using the ISOLDE on-line mass separator facility at CERN PS-Booster. Two detectors extended the standard set-up as already shown in Fig. 38. The first one was a single module of  $^6\text{Li}$ -glass detector, which provided extension to low neutron energies. The second one was installed for testing possibility to minimize the background by pulse-shape analysis with a small liquid scintillator neutron detector (SLND).

The  $P_n$  and the half-life value of the  $^{33}\text{Na}$  precursor ( $P_{1n}=52(20)\%$  and  $P_{2n}=12(5)\%$ , [Lan84],  $T_{1/2}=8.2(4)$  ms [Thi81]) have been reported previously, but neutron energy spectra were measured in this work for the first time. There are several reasons why the decay scheme of  $^{33}\text{Na}$  has not been established so far. First, the very short half-life demands fast mass-separation process. Secondly, the large energy-window ( $Q_{\beta}-S_n$ ) for the neutron emission emphasises the role of neutron detection. Thirdly, the low production yield makes the determination of numerous decay channels difficult.

In the present work two experimental methods have been combined for determination of the  $P_n$  values. These are simultaneous  $\beta$  and neutron counting with well-calibrated neutron and beta detectors, and  $\gamma$  spectroscopy of nuclei produced by fission.

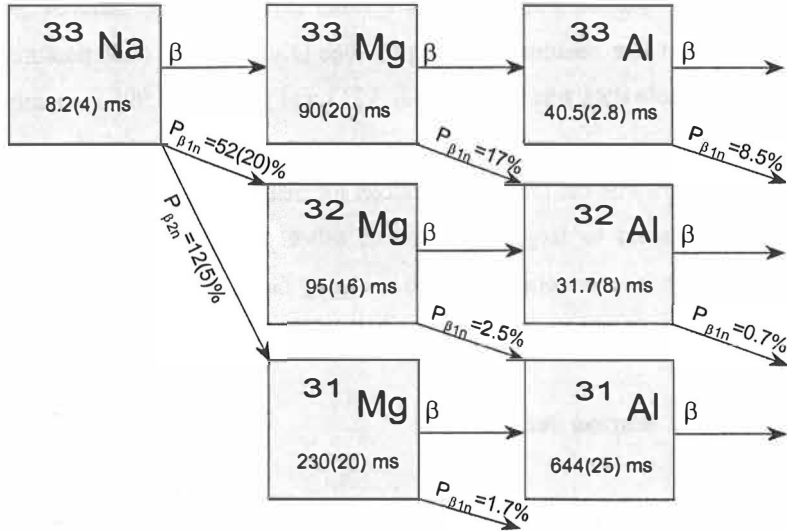


Figure 54. Decay of  $^{33}\text{Na}$  and its daughter activities. The values reported are taken from ref. [Aud97].

The methods were combined in such a way that the total  $P_n$  value was obtained by  $\beta$ -neutron counting and the ratio  $P_{1n}/P_{2n}$  was extracted from characteristic gamma transitions. The scheme of activities produced by the decay of  $^{33}\text{Na}$  is presented in Fig. 54. It illustrates the complexity and difficulty to isolate a particular decay in these conditions by using usual  $\beta$ - $\gamma$  spectroscopy and complete spectroscopy becomes critically dependent on neutron measurements in order to establish branching probability to different final states.

Additional checking of all the neutron-modules was performed on-line at ISOLDE with a  $^{29}\text{Na}$  source under the same detection conditions as for  $^{33}\text{Na}$  data taking.  $^{29}\text{Na}$  is a well-known  $\beta$ -delayed single neutron emitter with a prominent peak structure [Bau87,Zie81]. The neutron spectra of beta-delayed neutrons from  $^{29}\text{Na}$  are shown in Fig. 55.



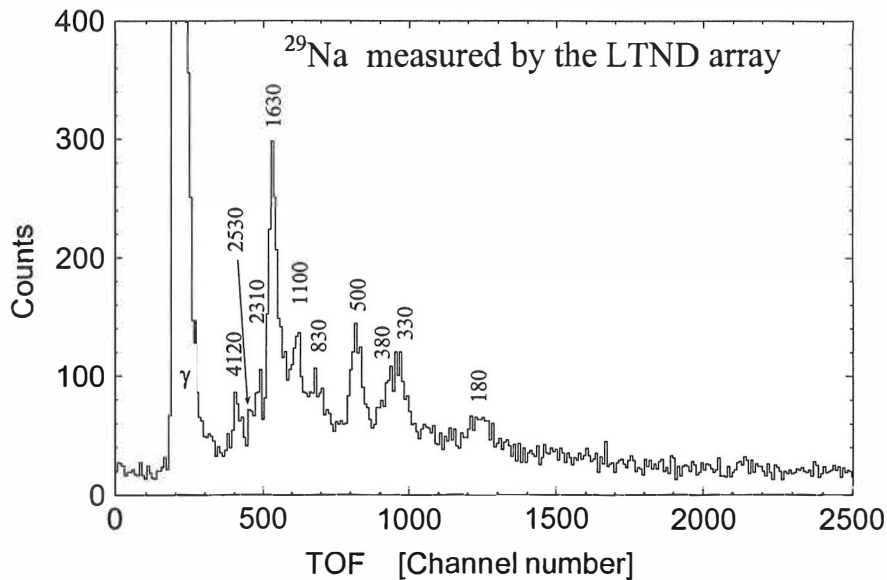


Figure 55. Neutron *TOF* spectrum of  $^{29}\text{Na}$  measured by the neutron detector array. The peaks marked are in keV.

### 6.2.1 Half-life of $^{33}\text{Na}$

The characteristic gamma line at 885 keV which follows  $\beta$ -delayed neutron decay to the first excited  $2^+$  state in  $^{32}\text{Mg}$ , was used for the half-life determination of  $^{33}\text{Na}$ . A short time gate (5-40 ms) provided additional cleaning of the background. The time distribution of 885 keV  $\gamma$ -events from two large-volume Ge detectors was fitted by a single component decay function after background subtraction resulting in a value of 8.1(4) ms for the half-life of  $^{33}\text{Na}$ , see Fig. 56. Beta singles and  $\beta$ -neutron coincidences with neutron *TOF* information were recorded simultaneously. The time distributions of singles  $\beta$  and neutron activities are shown in Fig. 57(b,c). The time variations of activities of  $^{33}\text{Na}$  and its daughter isotopes (Mg, Al, Si) were determined by an unfolding procedure as depicted in Fig. 57(b,c). This was done by fitting a series of exponential functions to the beta and neutron time spectra (using the CERN MINUIT program [Jam98]). The set of differential equations for the decay of beta and neutron branches were solved. This yielded expressions for the coefficients of exponential decay terms, which in turn enabled calculation of the relative contribution of  $^{33}\text{Na}$  in the beta and neutron time spectra.

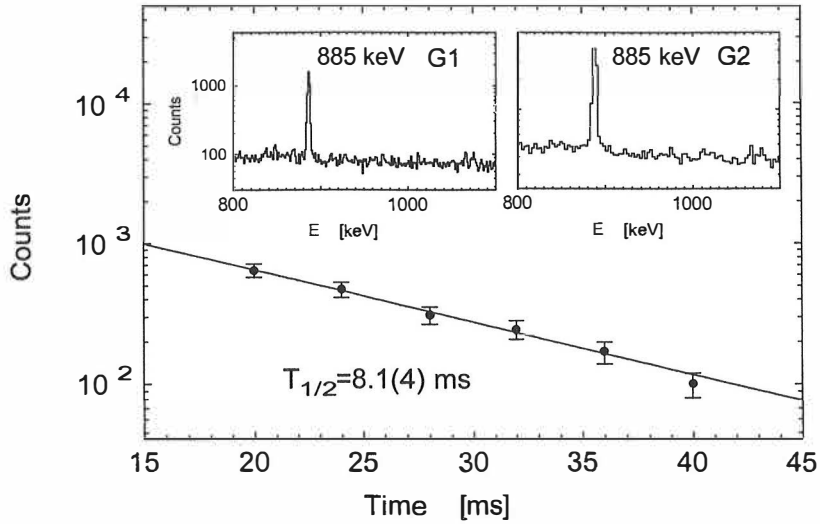


Figure 56. Decay curve of the 885 keV  $\beta$ - $\gamma$  coincidences after background subtraction. The 885 keV gamma line was measured using two large-volume Ge detectors.

To minimize uncertainties related to release time and transport dynamics of radioactive ions, the unfolding of the activities was performed only with the data obtained when the ISOLDE beam gate was closed, i.e. when ions were no longer collected. As a starting point for unfolding, except for the half-life of  $^{33}\text{Na}$ , I took the half-lives from the published references ( $^{33}\text{Mg}$ : 90(20) ms [Lan84],  $^{33}\text{Al}$ : 40.5(2.8) [Bou91],  $^{32}\text{Mg}$ : 95(16) ms [Aud97],  $^{32}\text{Al}$ : 31.7(8) [Gui84],  $^{31}\text{Mg}$ : 230(20) ms [Lan84],  $^{31}\text{Al}$ : 644(25) ms [Mur82],  $^{33}\text{Si}$ : 6.18 s [Mur82]). The half-life of  $^{33}\text{Na}$  was defined as a free parameter in the fitting procedure. The best solution defined by the minimum of  $\chi^2$ , resulted in a value of 7.9(4)ms for the half-life of  $^{33}\text{Na}$ .

The measured time distribution of  $\beta$ -delayed neutrons of  $^{33}\text{Na}$  is given in Fig. 57(c). Neutrons were measured by the neutron detector array and selected from gammas by *TOF* and pulse-height conditions. The events before being accepted to form a *TOF* distribution, were corrected for intrinsic efficiency of the neutron detector array according to the neutron energy.

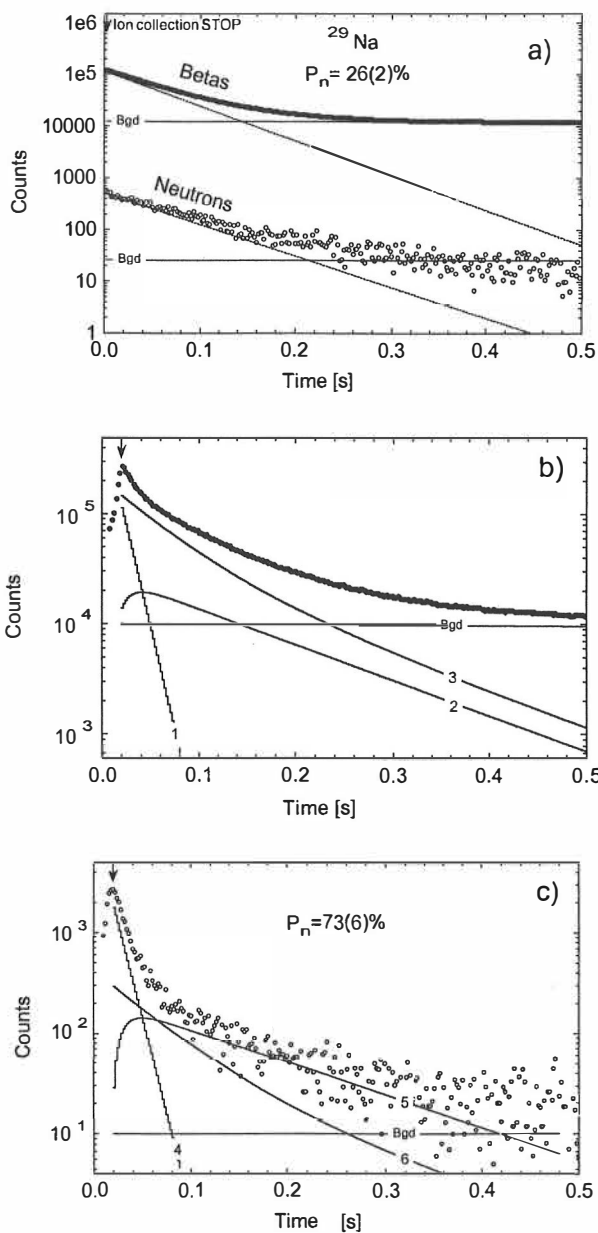


Figure 57. Growth and decay curves of beta and neutron activities. (a) Decay of the on-line calibration source  $^{29}\text{Na}$ . (b) Unfolding of the total beta and (c) neutron activity (intrinsic efficiency corrected) attributed to mass 33. The dots in all figures represent experimental data. The curves 1 and 4 denote the contributions of  $^{33}\text{Na}$  to beta and neutron time spectra, respectively. The curves 2 and 5 are the contribution of  $^{32,33}\text{Mg}$ , respectively. The curves 3 and 6 stand for the contributions of  $^{32,33}\text{Al}$ .  $^{33}\text{Al}$  is also present in the implanted  $A=33$  beam. The lines marked with (Bgd) represent background. The arrows indicate the time of switching-off the radioactive ion beam.

The  $^{33}\text{Na}$  descendants:  $^{33,32,31}\text{Mg}$ ,  $^{33,32}\text{Al}$ , are also significant  $\beta$ -delayed neutron emitters (see Fig. 54) and the unfolding of neutron intensity was done by using all those sources (and their half-lives). Again, I kept the half-life of  $^{33}\text{Na}$  as a free parameter in the fitting procedure. This resulted in additional information about the  $^{33}\text{Na}$  half-life and the relative neutron contribution of  $^{33}\text{Na}$  in the cumulative neutron time-spectrum. The unfolding of the neutron time-spectrum produced a value of 8.0(7) ms for the half-life of  $^{33}\text{Na}$ . The results of all of these half-life measurements using three different techniques are presented the table 5.

$^{33}\text{Na}$	885 keV-gamma line	$\beta$ -unfolding	n-unfolding
Half-life [ms]	8.1(4)	7.9(4)	8.0(7)

Table 5. Half-life of  $^{33}\text{Na}$  as measured by gamma, beta and neutron spectroscopy.

The weighted average of these three measurements by using gamma, beta and neutron spectroscopy resulted a value of 8.0(3) ms for half-life of  $^{33}\text{Na}$  in good agreement with the previous measurements [Thi81] which was 8.2(4) ms.

### 6.2.2 Determination of $P_n$ value

In the case of  $^{33}\text{Na}$ , the emission of one and two neutrons is observed through the related gamma activities. The three-neutron emission probability is predicted to be very small [Tak73] and was not observed in our experiment. The  $P_n$  value of  $^{33}\text{Na}$  was determined from the unfolded decay curves using absolute activities of  $\beta$ -coincident neutrons ( $N^c$ ),  $\beta$ -particles ( $N^\beta$ ) and efficiencies of the neutron array ( $\varepsilon_n(E)$ ) and the beta detector ( $\varepsilon_\beta$ ). The procedure was checked performing unfolding of the beta and neutron activity of the  $^{29}\text{Na}$  calibration source (see Fig. 57(a)). More precisely, the  $P_n$  value is obtained as a sum over all the channel numbers  $i$ , after efficiency correction event-by-event;

$$P_n = \sum_{i=20}^{500\text{ms}} \frac{N_i^n / \varepsilon_n(E_i)}{N_i^\beta / \varepsilon_\beta} = \sum_{i=20}^{500\text{ms}} \frac{N_i^c / \varepsilon_n(E_i)}{N_i^\beta}. \quad (20)$$

The value of 73(6)% for total ( $P_{1n}+2P_{2n}$ ) neutron emission probability of  $^{33}\text{Na}$ , as presented in Fig. 57(b,c) was obtained. By measuring the relative intensities of the

known characteristic 1941 keV and 947 keV gamma transitions of  $^{32}\text{Al}$  and  $^{31}\text{Mg}$  decays, it is possible to evaluate the ratio  $K=P_{1n}/P_{2n}=3.6(9)$ . This ratio can be compared to the theoretically predicted value of  $K=4.3$ , which has been deduced using the formalism of the gross theory of beta decay [Tak73]. The value of  $K=3.6(9)$  leads to  $P_{1n}=47(6)\%$  and  $P_{2n}=13(3)\%$  for one and two neutron emission probability of  $^{33}\text{Na}$ , respectively, in fair agreement with the less accurate previous values reported in ref. [Gui84].

### 6.2.3 Beta delayed neutron energy spectra

Spectroscopy of  $\beta$ -delayed neutrons probes the upper part of the excitation spectrum of the daughters  $^{33,32}\text{Mg}$ . Using the neutron detector array the TOF spectra of  $^{33}\text{Na}$  precursor were determined. Two consecutive time windows (short 5-40 ms and long 40-500 ms) have been used to separate short and longer-lived neutron emitters. The result is displayed in Fig. 58.

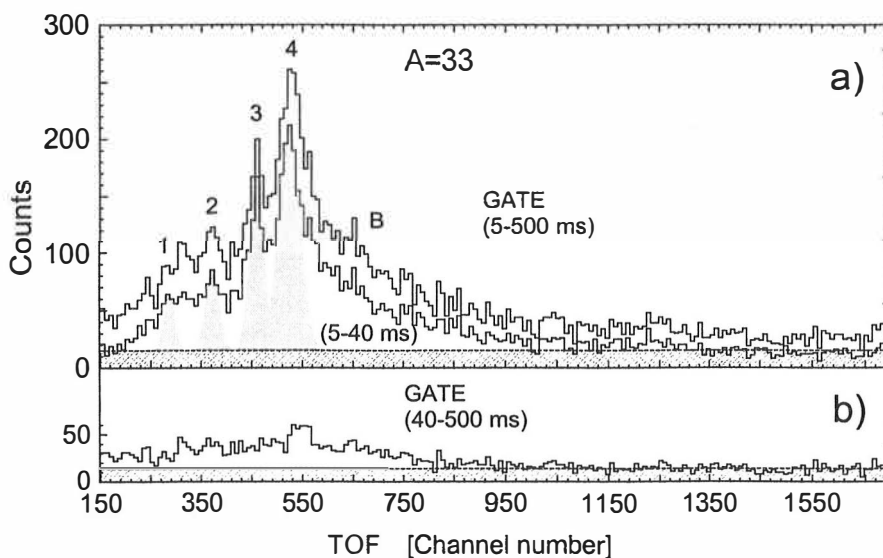


Figure 58. Neutron TOF spectra of  $A=33$  measured with the neutron detector array. (a) The lower curve represents the neutron spectrum in 5-40 ms time gate. The filled areas indicate fits to individual peaks. Neutron groups marked with "B" represent the contribution of  $^{33}\text{Na}$  decay to the spectrum in the region 200-700 keV. (b) The neutron spectrum in 40-500 ms time gate. The area below dashed line represents background.

In Table 6 the neutron peak energies and relative neutron intensities attributed to the  $^{33}\text{Mg}$  emitter are presented.

Peak mark	1	2	3	4	B
Energy (keV)	2830 (360)	1660 (160)	1020 (80)	800 (60)	200-700
Rel. intensity	0.055 (5)	0.072 (6)	0.124 (10)	0.218 (20)	

Table 6. Neutron energy peaks and relative intensities associated with the beta decay of the precursor  $^{33}\text{Na}$ . The neutron intensities are relative to the total number of detected neutrons. For the absolute values they must be multiplied by the factor of 0.73.

The neutron energy range below the threshold (60 keV) of the neutron detector array, was examined using a  $^6\text{Li}$ -glass scintillator detector. The absolute efficiency of the  $^6\text{Li}$  detector is low due to possibility of using only one small module. However, it was clear that there is no evidence of any prominent peak structure at lower neutron energies (4-60 keV) as can be seen in Fig. 59. The group of events marked by (A) is due to an increased efficiency caused by a broad resonance at 150-500 keV of the  $^6\text{Li}(n,\alpha)^3\text{H}$  reaction [Zet66] in the  $^6\text{Li}$ -glass detector.

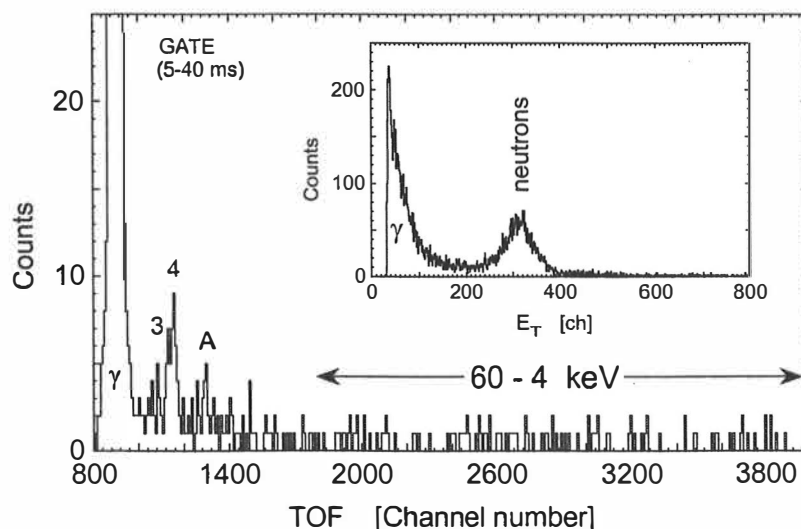


Figure 59. Neutron TOF spectra of  $^{33}\text{Na}$  measured by a small  $^6\text{Li}$ -glass neutron detector. The spectrum is gated by a short time window (5-40 ms) to minimize influence of longer-lived neutron emitters. Peaks with labels 3 and 4 are those identified in Fig. 58. In the inset, an illustration of the neutron-gamma separation using pulse-height discrimination is presented.

The main part of the neutron intensity is observed in the high-energy part of the spectrum using the LTND detector array. Furthermore, the spectrum exhibits a prominent peak structure. It appears that the main peaks at 800(60) and 1020(80) keV are produced in the first time gate (5-40 ms) and thus are assigned to decay of  $^{33}\text{Na}$  although subsequent neutron emitters,  $^{33,32}\text{Mg}$  have also a maximum of their contributions in this energy range (see Fig. 58(b)). The right-side tail (B) which is leaning on the neutron peak 4, definitely contains some fraction of  $^{33}\text{Na}$  neutron peaks in the energy range of 200-700 keV. However, in present experimental conditions they were not clearly separated.

#### 6.2.4 Triple coincidence analysis

In order to determine the cascade relations in the decay scheme,  $\beta$ - $\gamma$ -n triple coincidence analysis was performed. Despite the very small efficiency for triple coincidences, an example analysis for the branch assignment is given in Fig. 60. It is possible to notice the enhancement of the main  $\gamma$  lines following one and two neutron emission processes (see Fig. 60(b)). For the 2n- $\gamma$  events the overall efficiency is increased because of the double chance for a coincidence. Despite of low statistics we compared the ratios of gamma intensities measured by  $\beta$ - $\gamma$ -n triple ( $I_{\beta-\gamma-n}$ ) and  $\beta$ - $\gamma$  coincidences ( $I_{\beta-\gamma}$ ) versus gamma energy (see Fig. 60(c)). One can see that the ratio of the lines, related to the two neutron process (50, 171, 221 keV), are larger and distinguished from the corresponding ratios obtained with the lines related to one neutron emission (885, 1436, 1972, 2152 keV). This ratio can be used in the assignment of unknown gamma lines. In Fig. 61, a second example of triple coincidence analysis is given. The  $\beta$ -delayed neutron *TOF* spectrum of  $^{33}\text{Na}$ , obtained with the short time gate, is represented in Fig. 61(a). The spectrum in Fig. 61(b) represents the neutron *TOF* spectrum gated by the 885 keV gamma line.

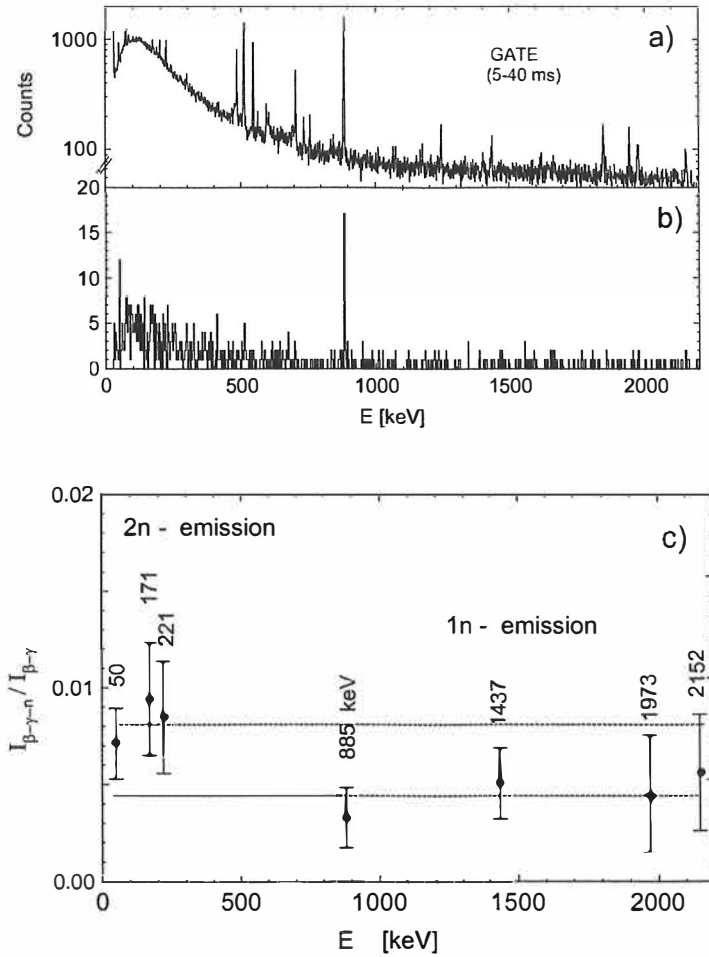


Figure 60. (a) Beta-gated gamma spectrum measured at  $A=33$  and (b) beta-gated gamma spectrum taken in coincidence with neutrons. Both spectra are gated by the 5-40 ms time window. (c) The ratio of the gamma lines  $I_{\beta-\gamma-n}/I_{\beta-\gamma}$  in coincidence with neutrons and only with betas. Note the two groups of events related to 1n and 2n process.

The neutron *TOF* spectrum gated by the  $\gamma$ -lines from the upper part of the cascade (1436, 1973, 2152 and 2551 keV) in  $^{32}\text{Mg}$  is given in Fig. 61(d). An estimate of the method's reliability is given in Fig. 61(c), which demonstrates low background gated by the out-of-range *TOF* signals. It is observed that the two most prominent neutron peaks (3 and 4) appear in coincidence only with the 885 keV  $\gamma$ -line, but not with the gammas from the higher levels (completely disappeared in Fig. 62(d)). This indicates that the most pronounced neutron peaks (3 and 4) are emitted exclusively in the decay process to the first excited state of  $^{32}\text{Mg}$ , therefore level energies and branching in



$^{33}\text{Mg}$  can be obtained. The neutron spectrum obtained in this experiment reveals two main neutron peaks at 800(60) keV and 1020(80) keV. In the gamma spectra, the strongest line is observed at 885 keV which represents 64 % of the  $\beta$ - $\gamma$ -n events [5].

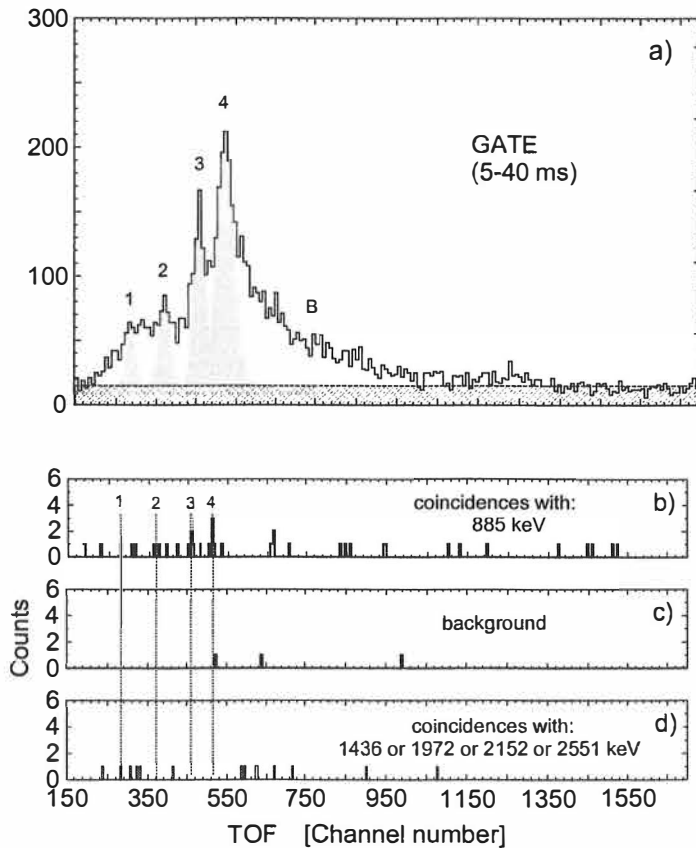


Figure 61. Triple coincidence analysis. (a) Neutron *TOF* spectrum attributed to the  $^{33}\text{Na}$  emitter. (b) Neutrons in coincidence with the 885 keV gamma line. (c) Background estimation. (d) Neutron spectrum in coincidence with the 1436, 1973, 2152 or 2551 keV gamma lines.

From the gamma intensity considerations and triple coincidence analysis, the two strongest neutron peaks do not seem to be connected to the levels above 885 keV in  $^{32}\text{Mg}$ . Consequently, it is possible to assume the population of the 885 keV level in  $^{32}\text{Mg}$  by two main neutron branches originating from levels at 3780 keV and 4000 keV in  $^{33}\text{Mg}$ . These results are displayed in Fig. 63 together with results obtained by

conventional  $\gamma$ -ray spectroscopy [5]. This observation is in agreement with the shell model calculation, which allows predictions of strong beta feedings to levels around 4 MeV as displayed in Fig. 62.

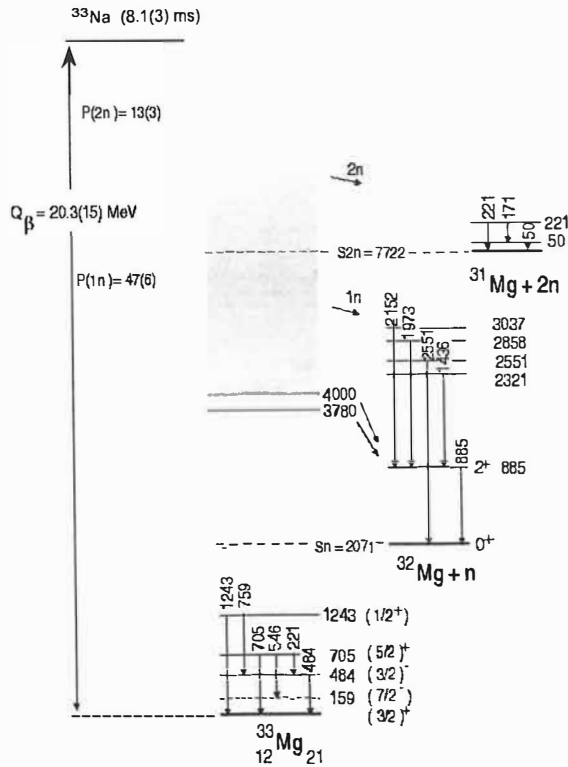


Figure 62. Decay scheme for  $^{33}\text{Na}$  as observed in ISOLDE run at mass 33.

### 6.2.5 Level of accidentals at low neutron counting rates

The accidental rate in the present conditions was studied by especially designed and constructed small neutron detector filled with liquid scintillator NE213. The liquid scintillators offer the possibility for gamma rejection, via pulse-shape analysis leading to a lower level of accidentals. The neutron spectra of  $^{29}\text{Na}$  measured by eight modules of the neutron detector array and one liquid scintillator module, are shown in Fig. 63. The spectra include the same statistics of detected neutrons. An advantage of the used NE213 detector is its position sensitivity along the axis connecting the two

PM allowing for the neutron flight path corrections. The position sensitivity, directly related to the time resolution of the used photomultipliers, can be better than 4 cm. The interaction point is found from time difference of the signals from the two PMs. Afterwards, the exact interaction point for each event is calculated providing means to correct for the length of the flight path.

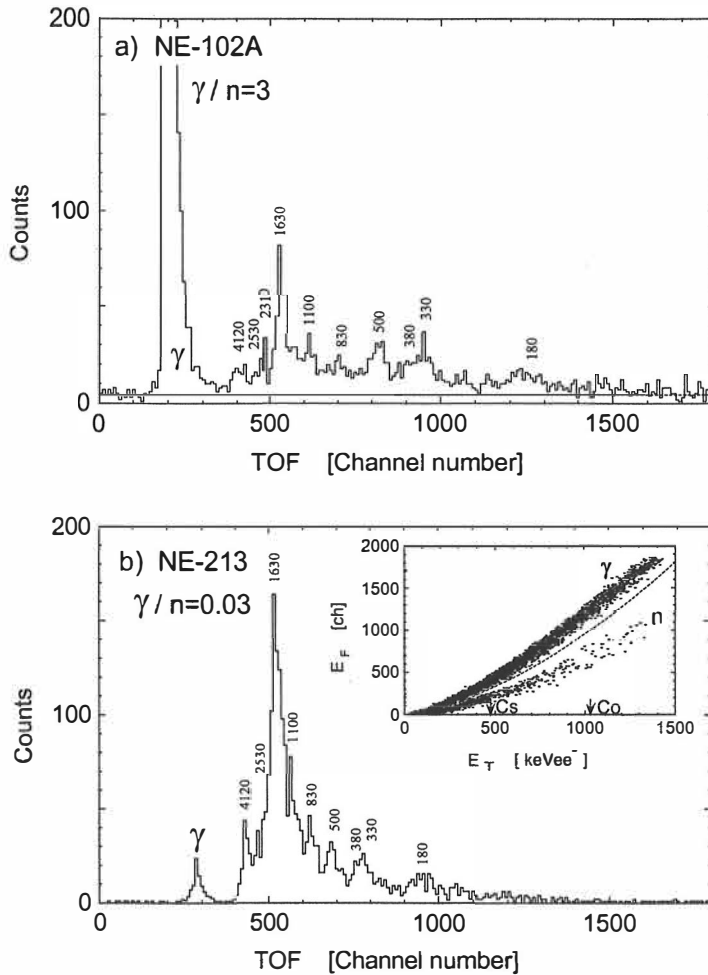


Figure 63. Beta delayed neutron *TOF* spectra of  $^{29}\text{Na}$  measured by (a) eight modules of neutron detector array and (b) one module of NE213 liquid scintillator detector after neutron-gamma separation via pulse shape analysis (shown in the inset).

Neutron-gamma separation was done via the usual pulse-shape discrimination method i.e. comparing the fast  $E_F$  (0-20 ns) and the total  $E_T$  (0-300 ns) integrated PM output signals. The energy calibration for  $E_T$  was done using  $^{137}\text{Cs}$  and  $^{60}\text{Co}$  gamma sources.

Compton edges of the deposited energy are indicated by arrows as shown in the inset of Fig. 63(b). It is clear that neutrons with energies higher than 150 keV are relatively well separated from the gamma-ray events.

In the present experimental conditions the gamma-event reduction via pulse-shaping analysis resulted in easier identification of neutron peaks above the neutron-gamma discrimination threshold. Also, the position sensitivity decreased the flight path uncertainty improving the overall energy resolution of this detector.

## 7. High-efficient systems and further improvements

To provide a neutron spectrometer for high-resolution neutron spectroscopy several variables have to be optimized. The first one is efficiency, then resolution and finally low detection threshold.

$^3\text{He}$  tubes surrounded with thermalizer are suitable for  $P_n$  determination in wide-energy ranges but without thermalizer as spectrometers they are inefficient in low production yield conditions. A significant gain in efficiency might be obtained by using  $^3\text{He}$  as a liquid scintillator in n-TOF or proportional mode, but it demands very low working temperatures and an effort for further research and development.

In the TOF detection systems with high-granularity, efficiency is gained by using a large number of modules but restriction comes from a limited space around the radiation point. In addition, other more speculative projects, such as the search for n-n correlations in decay, are also possible due to high granularity of the system. For the full spectroscopic information  $\beta$ - $\gamma$ -n triple coincidences are recommended and the space around the observation point has to be shared between  $\gamma$ -ray detectors and neutron TOF systems. An example of relatively high-efficient system (TONNERRE array [But00], GANIL) is shown in Fig. 64. This system combines several LTND counters and compact cluster detectors for  $\gamma$ -rays providing means for triple coincidence analysis technique. One module of TONNERRE is constructed of BC400 plastic scintillator (bar 160×20×4 cm), bent to a radius of curvature of 120 cm and viewed at both ends by photo-multipliers. The threshold for neutron detection using TONNERRE is around 300 keV. The intrinsic efficiency as a function of neutron energy is about 30% at 2 MeV and drops to 20% for 10 MeV neutrons. Using 16

modules of TONNERRE type with fixed flight-path of 120 cm, the total efficiency of device is around 5%.

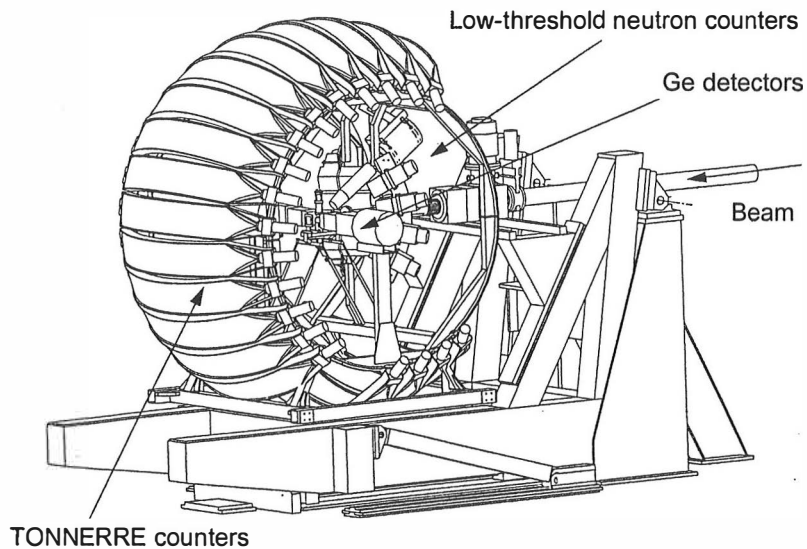


Figure 64. An efficient set-up for beta-delayed neutron spectroscopy and triple  $\beta$ - $\gamma$ -n coincident technique. Two sets of the neutron detector array (TONNERRE and low-threshold counters) for beta delayed neutron spectroscopy are powered by cluster detector(s) for  $\gamma$ -rays.

As shown in Fig. 63, long-term measurements can be improved by taking advantage of using liquid scintillators and n- $\gamma$  separation possibilities to reduce the level of accidentals. These facts suggested that the liquid scintillator based neutron detector like the PSND modules of HENDES type would be very useful. Recently improved time resolution provides neutron energy resolution of 5-10% for neutron energies of 1-10 MeV. The intrinsic efficiency varies between 33% at 2 MeV and drops to 18% for 10 MeV neutrons. Using 5 new PSND modules at 100 cm flight path provides about 3% for total efficiency of the device. Furthermore, I suggest further improvements by temperature cooling (to  $-15\text{ C}^{\circ}$ ) using Peltier electro-cooling unit coupled to the photo-cathode (evaporated on the inner window surface) of a single photomultiplier at the PSND (see Fig. 65). This assembly would further decrease the neutron detection threshold via dark current minimisation to values below 100 keV.

Therefore, proton-recoil scintillator detector equipped with an electro-cooling device may present a good single detector to cover rather broad neutron energy range for beta delayed neutron spectroscopy.

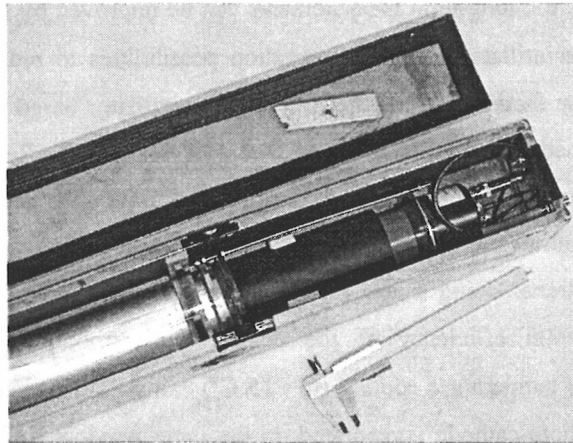
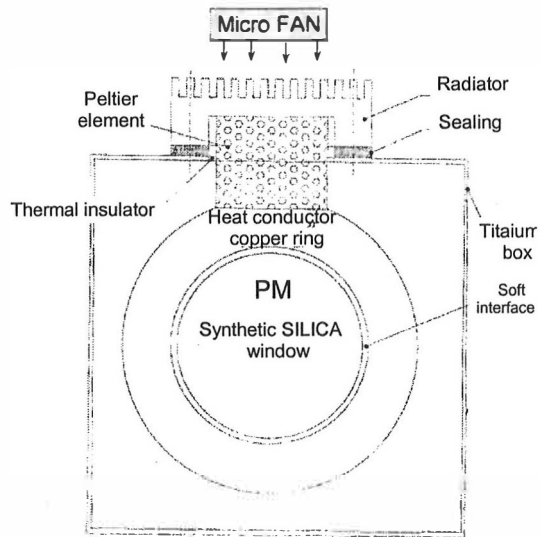


Figure 65. Top: Schematic drawing of Peltier cooling element for photo-multiplier. Bottom: View in the opened PSND and place for cooling device.

A possibility for detecting low-energy neutrons ( $< 1$  keV) is to use a complementary neutron-array constructed of  ${}^6\text{Li}$ -glass scintillator modules operated in *n-TOF* mode.

The  $^6\text{Li}$ -glass array is more efficient at low energies because of the nuclear reaction used for creating light response and the efficiency depends almost exponentially with energy decrease (see Fig. 15). The array might be placed closer to the source ( about 30 cm) to gain solid angle. Assuming 10 modules (bar  $30\times 5\times 2$  cm ) for the  $^6\text{Li}$ -array, the total mean efficiency would be about 3%. The same system (2-3 modules) might be placed very close to the source (to cover high solid angle). It would then serve as an efficient counter with a good timing properties allowing extraction and determination of total  $P_n$  values by means of simultaneous counting of beta and neutron activities.

In some cases, an alternative idea for neutron spectroscopy is velocity measurement of the heavy-recoil in coincidence with neutrons (*r-TOF*) [Pop99]. Fairly high efficiency is obtained due to fact of micro-second ranges for the time-of-flight of recoils (*R*). This long flying time allows relatively short flight-path base of about 4 cm but still having good energy resolution. Also, close geometry provides high solid angle and efficiency. Moreover, one additional advantage of the *r-TOF* spectrometer is possible combination with a set of gamma array detectors where the space around the radiation source is scarce. The set-up consists of micro-channel plate detector (MCP) for registration of the recoils and well shielded (Pb) liquid scintillator neutron detector (N) as schematically presented in Fig. 66. The separated ion beam is decelerated to about 20 eV (via low-voltage ion optics LVO) and *r-TOF* is extracted by measuring time interval between electron, neutron and heavy recoil. The mean efficiency of one N-MCP pair is around 5%.

The simple version of the *r-TOF* spectrometer involves only MCP and a neutron detector. An improved version would introduce position sensitivity of the both detectors (position sensitive PS-MCP and position sensitive PS-N) in combination with a thin position sensitive beta detector (PS-B). This set-up would have improved *r-TOF* energy resolution and would allow the study of the distribution of linear moments and angular correlations among decay products.

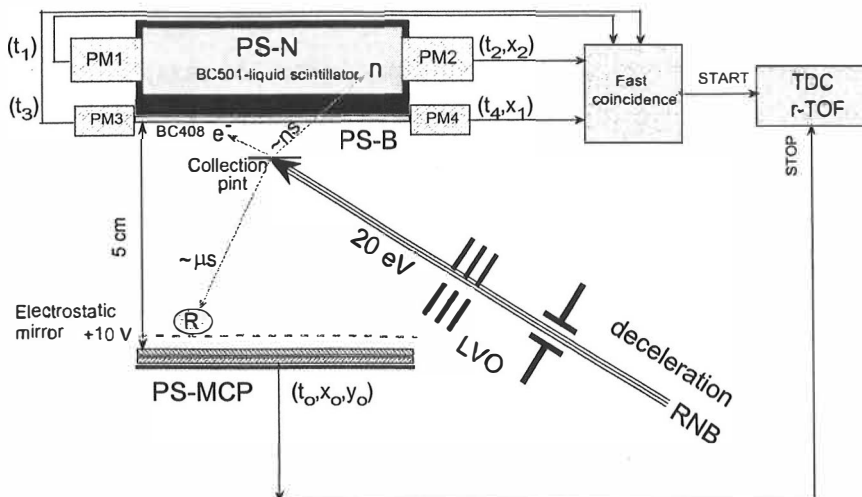


Figure 66. A schematic view of the principles for neutron spectroscopy by recoil time-of-flight (r-TOF) method.

## 8. Conclusions

This thesis is a study of production and spectroscopy of neutron-rich nuclei. In production of n-rich nuclei an alternative way which uses fast neutron induced fission of  $^{238}\text{U}$  was investigated. Precise information of absolute neutron yields emerging from thick targets was obtained in the first step. Furthermore, combination with measurements of fission-fragment mass distributions and mass selected isobars allowed determination of absolute cross-sections for  $^{238}\text{U}$  fission fragments induced by fast neutrons. The spectroscopic part deals with high-resolution beta-delayed neutron spectroscopy of the  $^{33}\text{Na}$  and  $^{94,95}\text{Rb}$  n-rich nuclei. Neutron spectroscopy was used as a powerful tool for characterisation of very n-rich nuclei formed in fission where usual spectroscopy suffers from high background. As in any precise measurement detailed knowledge of the detector properties was very important. Therefore, I have concentrated on examination of crucial neutron detector properties. It has been done by carrying out extensive experimental measurements and Monte-Carlo simulations (EFEN) based on the latest version of the neutron interaction cross-sections libraries. The simulation program has been written especially for the work



described in this thesis. Furthermore, several new detectors have been designed and constructed in order to extend detection possibilities and optimize detection conditions. A very important factor in *TOF* measurements is the start signal. Therefore, I have made special care to design and construct an improved trigger detector for  $\beta$ -delayed measurements. I have also redesigned and modernized position sensitive neutron detectors for HENDES measurements to reach better timing (energy) resolution and give lower detection thresholds. Furthermore, I have experimented with a small NE213 liquid scintillator detector. I have constructed it for testing of spectral possibilities and studies of background minimization. The design phase involved also simulations where all critical parameters were evaluated. Comparative study of results obtained by plastic and liquid scintillator detectors showed that liquid scintillators are superior because of the possibility to minimize background via n- $\gamma$  pulse shape discrimination. I have also investigated detection possibilities for low neutron energies. For that purpose I have constructed a small  $^6\text{Li}$ -glass detector. Nowadays these detectors are installed at several facilities as unique devices.

The neutron measurements with deuteron beam resulted in total yields of 0.109(10) n/d and 0.056(6) n/d for a  $^9\text{Be}$  target at  $E_d=65$  MeV and a  $^{12}\text{C}$  target at  $E_d=50$  MeV, respectively. We observed at least two neutron production processes. The first one includes deuteron stripping process. The neutrons produced in this way are emitted in the forward direction and have a broad energy distribution centered at about half the energy of the incident deuterons. The second detected process is neutron evaporation producing mainly low-energy neutrons emitted more or less isotropically. These measurements together with available data show that the neutron yield for both ( $^9\text{Be}$  and  $^{12}\text{C}$ ) converters at first strongly increases with incident energy (see Fig. 49) until it saturates at energies around 80-100 MeV. According to the ENDF/B-VI data base for fast-neutron induced fission, higher deuteron energies (>100 MeV) will not significantly increase the neutron yield. However, sharper peaking of the emitted neutrons could be obtained by using more energetic deuterons yielding better neutron focusing on the fissile target. Therefore, the deuteron stripping process is the one of interest for the production of n-rich nuclei. It is also well suited to the present design of the compact converter-fissile target assembly (see Fig. 3).

The experiment with 30 MeV proton beam and  $^{13}\text{C}$  target resulted in almost isotropic neutron emission with the total yield of 0.022(3) n/p. Unless the RNB target facility is redesigned, our results indicate that a  $^{13}\text{C}$  target bombarded with 30 MeV proton beam is not the ideal combination because of the weak forward focusing of the neutrons from the  $^{13}\text{C}(p,xn)$  reaction (see Fig. 48). On the other hand, this could be a preferred production mechanism in the case of incineration of nuclear waste. In this case uniformity of neutron angular distribution allows larger space around the neutron source producing a more efficient device. Similar considerations are valid for an Accelerator Driven Nuclear Power Plant system, in which a well-controlled powerful neutron source with uniform angular distribution is of the greatest importance.

Our measurements have shown also that neutrons produced using deuterons on the beryllium target are useful for the purpose of irradiation applications and construction of a powerful neutron source. Beryllium's specific feature is its low neutron separation energy resulting in a high neutron yield. In addition, it has a low Coulomb barrier and no particle-stable excited states resulting in high neutron-to-gamma-ray ratio. This feature provides a possibility to have a very clean neutron source and allows reliable determination of irradiation dose. Our data indicate that using 1  $\mu\text{A}$  deuteron beam it is possible to irradiate samples (for example silicon detectors or semiconductor components placed at forward direction) with a 20 mm diameter up to  $10^{14}$  n/cm<sup>2</sup> with within one hour (see ref. [2]). The  $^{13}\text{C}$  target associated with an intense proton beam provides also a good opportunity for an irradiation facility. In this case because of more isotropic neutron angular distribution many of samples can be placed around the source to gain sample statistics and decrease the total irradiation time. The yield data indicate that using a 1  $\mu\text{A}$  proton beam with a  $^{13}\text{C}$  target it is possible to irradiate samples 20 mm in diameter with  $1.4 \times 10^{13}$  n/cm<sup>2</sup> in one hour with relatively high irradiation uniformity.

Accurate measurements of the neutron yields in combination with measurements of fission-fragment mass distribution resulted in absolute cross-sections for fission of  $^{238}\text{U}$  induced by fast neutrons with an average energy of 20 MeV. Our results have shown that the  $Z$ -distributions are well fitted with a constant width of  $\sigma_Z = 0.7$ . This value is identical to the one adopted for fission induced by protons. The second result is the linear dependence of the most probable  $Z_p(A)$  values over a wide mass range. These features are globally reproduced by model calculations presented in Ref. [4].

Furthermore, when using fast neutrons we observed a shift of 0.8 units in charge distributions towards a larger neutron excess than in proton-induced fission. This favors production of most neutron-rich nuclei. Finally we observed that using a thick targets (conversion and fissile target) yielded a certain amount of low-energy neutrons producing higher peak-to-valley ratio ( $P/V= 2.8$ ) than observed in previous measurements.

Neutrons have been used in production and in spectroscopy of neutron rich nuclei. My thesis includes two cases of high-resolution neutron spectroscopy of exotic nuclei produced in fission. The case of  $^{33}\text{Na}$  beta-delayed neutron spectroscopy illustrates the advantage of correlated neutron and gamma spectroscopy for nuclear structure studies far from stability. The main result obtained from the measurement of the  $\beta$ -delayed neutrons in  $^{33}\text{Na}$  decay is the observation of two sharp maxima at 800(60) and 1020(80) keV. It was possible to extract neutron emission probabilities  $P_{1n}= 47(6)\%$  and  $P_{2n}= 13(3)\%$  by combining simultaneous beta and neutron counting with gamma spectroscopy. Furthermore, half-life values of  $^{33}\text{Na}$  from beta:  $T_{1/2}= 7.9(4)$  ms, and neutron-time spectra:  $T_{1/2}= 8.0(7)$  ms, were obtained by using fast scintillators for beta and neutron counting. Both values are in good agreement with the value,  $T_{1/2}= 8.1(4)$  ms, measured by means of the 885 keV characteristic gamma transitions in the decay of  $^{33}\text{Na}$ . These results, associated with the analysis of the gamma spectra, allow construction of a partial decay scheme for beta decay of  $^{33}\text{Na}$  to unbound levels of  $^{33}\text{Mg}$  as shown in Fig. 62. Implications of these results for shell model description of the Gamow-Teller decay of  $^{33}\text{Na}$  are discussed in ref. [5].

The  $\beta$ -delayed neutron decay of  $^{94,95}\text{Rb}$  has been studied using on-line mass separator IGISOL at Jyväskylä. The case of heavier n-rich nuclei is a bigger challenge in the sense of resolving narrowly spaced neutron emitting levels. The primary goal was testing of the possibilities of time-of-flight technique for  $\beta$ -delayed neutron spectroscopy of mass separated isobars. The sharp peaks in  $\beta$ -delayed neutron energy spectra have not been resolved (see Fig. 41), but the envelopes are very much the same when compared with former results obtained by  $^3\text{He}$  chambers. In addition, half-life and  $P_n$  values have been obtained for  $^{95}\text{Rb}$  precursor by fitting both the neutron and the beta activity curves. The results were in a good agreement with previously reported values and with values based on decay of characteristic  $\gamma$ -rays (see Fig. 40).

Absolute detection efficiency of the whole set-up is a crucial parameter in experiments of studying beta-delayed neutrons. In the case of  $^{33}\text{Na}$  absolute efficiency of the gamma-ray detectors was about 2% for 1 MeV gamma-rays. The LTND neutron detector array had an averaged absolute efficiency of 0.3%. In the case of  $^{33}\text{Na}$  some of triple coincidences were correlated. However, precise location of the other neutron-gamma correlated peaks would demand higher absolute efficiencies for both gamma and neutron detectors. A detection system for the future was discussed in chapter 7 of this work. I have big expectations in respect to on-going developments in cooling and trapping of ions [Sze01] at IGISOL. These developments will allow background reduction and minimization of accidental coincidences bringing new possibilities for  $\beta$ -delayed neutron spectroscopy.

To conclude I would like to stress that fast-neutron induced fission of heavy nuclei at intermediate energies is a promising tool for the production of exotic neutron-rich nuclides. It has also become evident that high-resolution neutron spectroscopy presents a powerful research tool for present and future investigations of exotic nuclei.

For  $\beta$ -decay of nuclei far from stability, it is a convenient approach to treat averages over large numbers of narrowly spaced high-excited states instead of dealing with individual transitions. For this purpose, the general concept of the  $\beta$ -strength  $S_\beta(E)$  and the  $\beta$ -intensity function  $I_\beta(E)$  (relative  $\beta$ -feeding per energy interval) has been employed. These two quantities are connected by

$$I_\beta(E) = \frac{S_\beta(E) f(Z+1, Q_\beta - E)}{\int_0^{Q_\beta} S_\beta(E) f(Z+1, Q_\beta - E) dE} \quad (1)$$

where  $f$  is the integrated Fermi-function. Moreover, the  $S_\beta(E)$  can be determined as the energy distribution of the reciprocal  $fT_{1/2}$  - value [Duk70,Han73]. The experimental quantities to be determined are then the  $\beta$ -decay half-life  $T_{1/2}$ , the  $Q_\beta$  and the relative  $\beta$ -feeding per energy interval  $I_\beta(E)$ :

$$S_\beta(E) = \frac{D (g_V + g_A)^2}{f(Z+1, Q_\beta - E) T_{1/2}} I_\beta(E) \quad (2)$$

where  $D$ ,  $g_V$  and  $g_A$  are constants. The  $\beta$ -strength is strongly influenced by the giant resonance: the isobaric analogue state (IAS) and the Gamow-Teller giant resonance (GTGR). For  $\beta$ -decay of n-rich nuclei, both are situated outside the window of observation. The tail of the latter leads to an enhancement of the intensities of the  $\beta$ -branches to high-lying levels (see Fig. 4). The function  $S_\beta(E)$  is discrete when  $E_s < S_{In}$  and becomes continuous when  $E_s > S_{In}$ . The neutron spectra can be expressed as:

$$I_n(E_n) = const \sum_{J,\pi} \frac{\Gamma_n^j(E_n)}{\Gamma_n^l(E_n) + \Gamma_\gamma} |M_{J\pi}|^2 \rho_{J\pi}(E) f(Z+1, Q_\beta - E), \quad (3)$$

here  $\Gamma_n^l$  is width for the emission of neutrons of wave number  $l$ ,  $\Gamma_\gamma$  gamma width,  $\rho_{J\pi}$  density of levels of spin  $J$  and parity  $\pi$ ,  $|M_{J\pi}|^2$  is the average of the square of the

nuclear matrix elements that govern the  $\beta$ -decay.  $E$  stands for excitation energy of the level fed by the beta particle and  $E_n$  is neutron energy. This equation can be further simplified since, only the energy-dependent component of the factors in the formula is of interest, the spin component of the level density function can be removed. The Fermi function can be approximated by the expression  $f(Z+1, Q_\beta - E) \approx \text{const} (Q_\beta - E)^5$  and the neutron width  $\Gamma_n'$  is taken to be proportional to the neutron transmission coefficients [Bla79]. Earlier studies of  $\beta$ -strength function demonstrate that the nuclear matrix element  $|M_{Jn}|^2$  is approximately energy independent. If we further neglect competition between different neutron branches, the neutron intensity  $I_n(E_n)$  can be expressed as:

$$I_n(E_n) = \sum_l C_l \frac{T_l}{T_l + K_l} \frac{\exp(2\sqrt{a(E - P)})}{(E - P)^{5/4}} (Q_\beta - E)^5, \quad (4)$$

where,  $C_l$  is a normalisation constant,  $T_l$  is the neutron transmission coefficient and  $K_l$  is a constant proportional to the gamma width  $\Gamma_\gamma$ . The parameters  $a$  (level density constant) and  $P$  (pairing energy) are those appearing in the usual form of the level density formula. The sum is taken over the partial waves of importance for neutron emission. Finally, the total neutron emission probability  $P_n$  is given by

$$P_n = \int_{S_n}^{Q_\beta} I_n(E) dE, \quad (5)$$

therefore,  $P_n$  is very sensitive to both the  $S_\beta(E)$  structure and the energies  $Q_\beta$  and  $S_n$ .

The aim of fission fragment data analysis is to determine primary fragment masses ( $m_1, m_2$ ) and velocity vectors ( $V_1, V_2$ ). Fission fragment velocity vectors in zero approximation were determined from time-of-flight and position information. An example of intrinsic PSAC  $X$ - $Y$  coordinate distribution is given in Fig. 34. For the transformation into the laboratory system the mask on PSAC surface is used. More precisely, the plot  $(X-T+c_0)$  versus  $(Y-T+c_0)$  (see Fig. 34) is used where the  $c_0$  is usually a half of the TDC full scale. Knowing the orientation of the mask, and distance between its parts, it is possible to get the position of the PSAC centre, calibration for transformation of channels into centimetres, and the rotation angle needed to correlate electronic  $X$  and  $Y$  coordinates with actual PSAC orientation. Furthermore, calibration and rotation around the centre to get the new coordinates, labelled  $(X_{self}, Y_{self})$  which are associated with PSAC surface is performed. The centre of PSAC becomes point  $(0,0)$ , and the edge of the PSAC is 122 mm away from the centre:  $X_{self}^2 + Y_{self}^2 = (243/2)^2$ . By knowing the experimental geometry, the next step is transformation  $(X_{self}, Y_{self})$  into  $(X_{lab}, Y_{lab})$  – coordinates expressed in cm and associated with the laboratory system. At this stage, the point of interaction of both fragments with the PSACs is known, allowing determination of the folding angle in the lab system (using cosine theorem). The folding angle determined this way is an angle between two vectors in space, and is always less than  $180^\circ$ . For every event (in event-by-event analysis) the angles, at which both fragments fly through the thin target and support foil are thus determined. Knowledge of directions allows more precise corrections for the thickness, “visible” by fragments and corresponding energy losses. The next step is the calibration of the time scale by,  $T_{1,2}[ns] = c_1 (T_{1,2}[ch] - T_{1,20}[ch])$  where  $c_1$  is a time calibration constant determined by time calibrator unit,  $T_{1,20}$  are “zero channels” corresponding to the instant of the reaction. These “zero channels” are first determined from the position of well-known peaks measured by using  $^{252}\text{Cf}$  (light and heavy peaks), and latter adjusted manually. Further, velocities of both fragments are calculated. If we assume that the start detector is in front of PSAC1 then:

$$V_1 = \frac{L_1 + \Delta_{PSAC} / \cos(\alpha_1) - L_{start} / \cos(\alpha_1)}{T_1(ns)} \quad V_2 = \frac{L_2 + \Delta_{PSAC} / \cos(\alpha_2)}{T_2(ns) + L_{start} / \cos(\alpha_2) / V_1}, \quad (1)$$

here,  $L_{1,2}$  are distances from interaction points with PSACs to the target,  $\Delta_{PSAC}$  is flight distance inside PSACs to cathode ( $\approx 5$  mm)  $L_{start}/\cos(\alpha_{1,2})$  is distance to START detector. The first approximation for fragment masses  $m_{1,2}$  is calculated using momentum conservation perpendicular to the beam axis  $m_1 V_1^\perp = m_2 V_2^\perp$  and assuming that the two fragment masses add-up to the mass of the compound system prior to fission or  $m_1 + m_2 = M^{projectile} + M^{target} - M^{pre} = M_{CN}$  where  $M^{pre}$  is the mean total mass of the particles emitted from the compound nucleus before scission. Since neutrons dominate in pre-scission emission,  $M^{pre}$  was assumed to be equal to the neutron pre-scission multiplicity  $M_n^{pre}$ . The operational formulae (2) are used to get the first

$$m_1 = \frac{M_{CN} V_2 \sin(\alpha_2)}{V_1 \sin(\alpha_1) + V_2 \sin(\alpha_2)} \quad m_2 = \frac{M_{CN} V_1 \sin(\alpha_1)}{V_1 \sin(\alpha_1) + V_2 \sin(\alpha_2)}, \quad (2)$$

evaluation of the FF masses where  $M_{CN}$  is mass of the compound nucleus minus total mass of the pre-scission emitted particles. The value of  $M_n^{pre}$  was first taken from theoretical calculations and, at a later stage, substituted with the experimental value. The influence of uncertainty in the  $M^{pre}$  determination turned out to be much smaller than the overall errors determined mostly by the time resolution of the PSACs. Then energies are given as:

$$E_1 = \frac{M_1 V_1^2}{2} \frac{amu}{c^2} \quad E_2 = \frac{M_2 V_2^2}{2} \frac{amu}{c^2}, \quad (3)$$

where,  $amu=931.5$  MeV, and  $c$  is the velocity of light. Non-relativistic approach is valid since  $(V/c)^2$  is of the order of 1% for the fastest elastically scattered particles, and is typically 0.2% for fission fragments. The known fragment mass and energy (from the first approximation) allows one to calculate subsequently the energy losses in the start detector and the target-foil composition. For the energy losses we usually use pre-calculated energy loss matrices  $M_{los}(E,A,Z)$  which are incorporated in the data analysis program (Pacal, Fortran or C). The energy losses are accounted for by adding some energy (velocity) to the fragments, the added amount depending on the fragment's energy and mass. Unfortunately, the HENDES facility is not yet able to detect directly the charge of fragments. It provides information for the masses only.



The most probable charge  $Z_p(A)$ , is calculated from measured masses using the CCR hypothesis [Rao72] for the distribution of charge in the fission process. The CCR rule proposes that the compound nucleus fissions rapidly in such a way that both post-neutron secondary-fragments (light and heavy) have the same neutron-to-proton number as the compound nucleus. The most probable charge  $Z_p(A)$  is calculated using the following equation:

$$Z_p = \frac{Z_f}{A_f - \nu_T} A \quad (4)$$

where  $A_f$  is the mass of the fissioning nucleus and  $\nu_T$  is the total number of prompt neutrons emitted from both fission fragments.

From the corrected values of  $E_{1,2}^i = E_{1,2} + \Delta E^{start} + \Delta E^{target}$  and the old values of fragment masses  $m_{1,2}$ , new values of the fragment velocities in the target are calculated; the above procedure is repeated until it converges or more precisely until changes in velocities become small ( $< 1\%$ ). Usually two to three iterations are sufficient. Using the new extracted values of  $V_{1,2}$  and  $m_{1,2}$  the experimental laboratory velocity of the compound nuclear system  $V_{CN}$ , the fragment velocities in the centre-of-mass (c.m.), and the total kinetic energy  $TKE$  distribution of the fission fragments are calculated according to Viola systematic [Vio85]. In case of heavy ion induced reactions it is assumed that the linear momentum of the projectile is fully transferred to the compound nucleus and  $V_{CN}$  is calculated using the original momentum of the projectile. In case of (d,pf) reaction the  $V_{CN}$  is calculated as a sum of fission fragments' momenta, to the beam direction as:  $V_{CN} = m_1 V_1 \cos(\alpha_1) + m_2 V_2 \cos(\alpha_2)$ . Furthermore, the  $TKE$  is calculated by just adding fragments' energies in c.m. system and in addition calculate angles between fragments in c.m. system which should be centred around  $180^\circ$  and serve as a check-point of the analysis.

The qualitative fission model of  $^{238}\text{U}$  induced by light particles (p or n) at intermediate energies, which has been used for comparison with experimental data is presented in the following. The model is implemented in a simulation programme originally developed by Prof. Valery Rubchenya. The model is being updated by taking advantage of new experimental data in literature and measurements at the JYFL. The program simulates the history of the compound nucleus (CN) formed in collision with a light particle. The two directions in the compound decay are followed with a certain probability. The first one is fission and second is formation of a residue formed via evaporation of light particles and  $\gamma$ -rays. In the fission the nucleus separates into two fragments (light and heavy or with similar size). Fusion-fission process lasts a time of the order of  $10^{-21-19}$  s, when the system evaporates the light particles (pre-scission) or  $\gamma$ -rays until scission when the neck shrinks to zero. Fission fragments fully accelerated by the Coulomb field are still excited and continue with emission of so called post-scission particles [Hil92].

With increasing bombarding energy some of the particles can be emitted in the CN formation process as so called pre-equilibrium particles. They are very energetic and preferably emitted in the forward emission cone. If the CN has not enough time to be equilibrated over all magnitudes of freedom one speaks about quasi-fission process. Along the second decay route the excitation of the CN is not removed by fission but solely by the evaporation of light particles and  $\gamma$ -rays, which stop if the excitation drop below corresponding binding energy (plus Coulomb barrier in case of charged particles). The process of emission of the  $\gamma$ -rays lasts until zero energy and the lowest spins are reached. The primary decay process is followed by successive  $\beta$ -decays until one ends to a stable element of the nuclide chart. Which of the decay routes will take place depends on the mass, excitation energy and angular momentum of the CN.

The compound nucleus formation cross-section for the case of bombarding  $^{238}\text{U}$  by light particles is calculated by the optical model (subroutine in the programme ) taking into account a contribution of the pre-equilibrium emission of protons and neutrons. When the colliding system forms the CN fission occurs with a certain probability without the emission of a particle (first-chance fission). During the fission

in the simulation one, two, etc. neutrons are allowed to be emitted (higher chance fission).

A theoretical calculation of the  $^{238}\text{U}$  fission-fragment formation cross sections at intermediate energy and the gross structure of the fission characteristic (mass and charge distributions) are implemented in the programme in terms of fission modes. The fission modes of  $^{238}\text{U}$  are a result of influence of nuclear shell structure on the potential energy surface (PES) of the  $^{238}\text{U}$  fissioning nucleus [Bro90]. The fission process is guided by the valleys and bifurcation points of the PES from the equilibrium shape to the scission point. It is well known that nuclear shells play an important role in fission mass distribution. For example, the familiar asymmetric mass division, location of the heavier peak position and the presence of “shoulders” etc. are best understood in terms of the influence of shells in fission. The presence the light “shoulder” can be viewed as being due to the possible influence of the  $Z= 28$  proton core, which forces the yields to be higher in this region in much the same way as in the  $N= 82$  neutron core forces the yields to be higher around  $A\approx 132$ . There are suggestions that around these magic numbers the primary fission fragments have low-excitations and consequently emit almost no neutrons because of greater rigidity against distortion from nearly spherical shapes. Therefore, it is very likely that the shoulder on the heavier side is the reflection of the shoulder on the light side of the mass distribution and they are complementary in nature. Furthermore, the influence of the  $Z= 28$  proton shell is obviously much weaker than that of the  $N= 82$  neutron shell. The calculations based on a static scission point model predicts a possibility of "deformed" shells influencing the mass distribution in far asymmetric mass split. From a consideration of deformed stiffness, the heavy fragment resulting from the very asymmetric mass split will be highly deformed while the light fragment may tend to be close spherical. The deformed shells corresponds to  $N= 66, 88, 106$  and  $Z= 38, 44, 66$  [Wil76]

For the calculation of independent fission products cross-sections, the simulation programme uses a theoretical model, which has been suggested and described in ref. [Kar91, Jauh95, Huh97, Rub98]. Shell effects have been introduced in the model accordingly the standard Strutinsky shell correction method [Str68]. Furthermore, the nuclear potential energy has been parameterised according to work [Pas71]. Also, the model incorporates odd-even effects in charge and mass, then

influence of nuclear friction on fission probability and light particle evaporation on the descent from saddle to scission point by a method described in ref. [Hof95].

For the description of the mass distribution envelopes for fission of  $^{238}\text{U}$  at intermediate energies, the model consists of two parts.

(I) Modelling the reaction mechanism to calculate mass, charge, and excitation energy distributions of compound nuclei and, (II) Modelling the fission process itself.

The formation cross section of a fission product with mass number  $A$  and charge number  $Z$  implemented in the programme are expressed in the form

$$\sigma_f(A, Z) = \sum_{A_c Z_c} \int Y_{ind}(A, Z) dE_x \frac{d\sigma_f(A_t, Z_t, A_p, Z_p, E_p, A_c, Z_c, E_x)}{dE_x} \quad (2)$$

where indexes  $t$ ,  $p$  and  $c$  refer to target, projectile and compound nuclei (CN), respectively,  $d\sigma_f/dE_x$  is the partial fission cross-section of the compound nucleus at the excitation energy  $E_x$ . The excitation energy  $E_x$  of the CN in the model, is assumed to be  $E_x = E_{n(p)} + Q - (TKE + E_\gamma)$ , where  $E_{n(p)}$  stands for projectile (neutron or proton) energy in c.m. system,  $Q$  is the  $Q$ -value of the nuclear reaction,  $TKE$  the total kinetic energy and the  $E_\gamma$  energy removed by prompt  $\gamma$ -rays.  $Q$  value is usually estimated by using mass-excess values [Wap77]. Total kinetic energy is calculated accordingly Vola's systematic [Vio85] as  $TKE = 0.119 Z^2/A^{1/3} + 7.3$  MeV and stands for total kinetic energy released in fission as a result of the large Coulomb field between the fragments at scission point.  $Z$  and  $A$  refer to the fissioning nucleus. Furthermore, the average fission kinetic energy is nearly independent of the fissioning nucleus. In other words, most of the heat of the system at scission is converted directly into excitation of the fragments. Thus, measurement of the  $TKE$  can serve as to identify the approximate  $Z^2/A^{1/3}$  value of the fissioning system. It should be noted also that the excess heat possessed by the separating fragments is dissipated primarily by neutron evaporation. The partial fission cross-section in the eq. 2 is calculated in the cascade evaporating time-dependent statistical model including pre-equilibrium neutron emission. The summation (on  $A_c$  and  $Z_c$ ) goes over different fission chances or after no, one or several prompt neutron emission. The  $Y_{ind}(A, Z)$  is the independent yield defined as the yields of fission products after light particle emission from excited primary fragments. In calculations only neutron emission was considered because at

excitation energies up to about 150 MeV, the emission of protons and other charged particles we considered as negligible with respect to the precision of available experimental data.

$$Y_{ind}(A, Z) = \sum_{A_{lcp}, Z_{lcp}} P_{A_{lcp}, Z_{lcp}}(A + A_{lcp}, Z + Z_{lcp}, A_c, Z_c, E_x) \times \quad (3)$$

$$P_{pre}(Z + Z_{lcp}, A + A_{lcp}, A_c, Z_c, E_x) Y_{pre}(A + A_{lcp}, A_c, Z_c, E_x)$$

Here  $P_{A_{lcp}, Z_{lcp}}$  is a probability of emission of  $(A_{lcp}, Z_{lcp})$  light particles from fragment with mass  $A + A_{lcp}$  and charge  $Z + Z_{lcp}$ . The  $P_{pre}$  represents a charge distribution of the  $A + A_{lcp}$  isobaric chain and  $Y_{pre}$  is a primary fission fragment mass distribution.

At low excitation energies, the primary fission fragment mass and charge distributions exhibit odd-even staggering. The primary distributions are presented in the factorised form

$$P_{pre}(Z) = P_{pre}^*(Z) F_{oe}(Z), \quad Y_{pre}(A) = Y_{pre}^*(A) F_{oe}(A) \quad (4)$$

here  $P_{pre}^*(Z)$  and  $Y_{pre}^*(A)$  are smoothed distributions, and functions  $F_{oe}(Z)$  and  $F_{oe}(A)$  describe odd-even staggering. The method of modelling the smoothed mass distribution is based on the multimodal nature of nuclear fission [Bro90]. A smoothed mass distribution is approximated by four fission modes (Symmetric, Standard I, Standard II and Supersymmetric) corresponding to different nuclear shells in fragments. This resulted that measured pre-neutron emission mass distribution in fission of the  $^{238}\text{U}$  can be de-convoluted by superposition of seven Gaussians as:

$$Y_{pre}^*(A) = C_s y_s(A) + C_{a1} y_{a1}(A) + C_{a2} y_{a2}(A) + C_{a3} y_{a3}(A) \quad (5)$$

Here  $y_s$  and  $y_{a1}$ ,  $y_{a2}$ ,  $y_{a3}$ , are symmetric and asymmetric components which presented contributions from different fission modes. Each asymmetric component consists of two Gaussians representing the heavy and light fragment mass groups. The component  $y_{a1}$  describes magicity at  $Z= 50$  and  $N= 82$  in the heavy fragments and the supersymmetric component  $y_{a3}$  is influenced by the nuclear shells  $Z= 28$  and  $N= 50$  in the light fragments. The asymmetric mode  $y_{a2}$  is supposed to be connected with the

"deformed" nuclear shell at  $N= 86-90$ . The competition between fission modes is determined by fission dynamics and the nuclear shells in the fission fragments.

The smoothed pre-neutron emission isobaric chain charge distribution is approximated by a Gaussian distribution, therefore the odd-even structure can be described by a parameter defined as a third difference of the natural logarithms of the fractional yields [Tra72]. The model considers the proton and neutron odd-even effect separately using a function as:

$$F_{oe}(Z) \approx \exp((C_{p1} + C_{p2}) \delta_Z(A_c, Z_c, E_x)) \quad (6)$$

where  $C_{p1}$  and  $C_{p2}$  are defined by the parity of the proton number in the two primary fragments ( $C_p = +1$  if  $Z$  is even and  $C_p = -1$  if  $Z$  is odd). The proton odd-even difference parameter  $\delta_Z(A_c, Z_c, E_x)$  is a function of excitation energy, charge and mass number of the compound nuclei in accordance with experimental data. In the model the proton and neutron odd-even difference parameters are taken to be proportional, i.e.  $\delta_N(A_c, Z_c, E_c) = c \delta_Z(A_c, Z_c, E_c)$  where constant  $c < 1$ . Finally odd-even staggering in the primary mass distribution is described by the combination of proton and neutron odd-even effects.

References:

- [Alk92] I.D. Alkharov et al., JINR Rapid Comm. 6(57)-92, Dubna (1992), p. 80.
- [Aud99] G. Audi et al., Nucl. Phys. A 624(1997)1.
- [Aud97] G. Audi, O. Bersillon, J. Blachot, A.H. Wapstra, Nucl. Phys. A 624 (1997) 1.
- [Äys01] J. Äystö, JYFL Preprint No. 1/2001., to be published in Nucl. Phys. A, 2001.
- [Bab71] S. Baba et al., Nucl. Phys. A 175 (1971) 177.
- [Bau87] P. Baumann et al., Phys. Rev. C 36 (1987) 765.
- [Bau70] P. Baumann, et al., Phys. Rev. C 58 (1998) 1970.
- [Bel98] A. Belyam et al., Nucl. Instr. and Meth. B 134 (1998) 217.
- [Ben98] J. Benlliure et al., ENAM98, Exotic Nuclei and Atomic Masses, edited by  
[Ben98] J. Benlliure et al., ENAM98, Exotic Nuclei and Atomic Masses, edited by  
B.M. Sherill, AIP 1998, p 960.
- [Ben97] "International Workshop on Research with Fission Fragments",  
Benediktbeuern, 1996, edited
- [Bic98] Saint-Gobain Industrial Ceramics, Inc. BICRON-catalogue 1998.
- [Bir72] J.B. Birks and R.W. Pringle, Proc. R. Soc. Edinburgh Sect A 70, 233 (1972).
- [Bla79] M. Blatt and V. Weisskopf, Theoretical Nuclear Physics, New York, chap 8-9  
(1979).
- [Bou91] M. Bounajma et al. in " First European Biennial Workshop on Nuclear  
Physics, Megeve, France, March 25-29 (1991) ", edited by World Scientific  
(1991) p. 227.
- [Bou96] M. Bounajama, Thesis (1996) Strasbourg, CRN 96-43.
- [Bre89] H.J. Brede et al., Nucl. Instr. and Meth. A 274 (1989) 332.
- [Bro90] U. Brosa et al., Phys. Rep. 197 (1990) 167.
- [Bud88] C. Budtz-Jorgensen et al., Nucl. Phys. A, 490 (1988) 307.
- [But00] A. Buta et al., Nucl. Inst. and Meth. A 455(2000)412-423.
- [Cec79] R.A. Cecil, B.D. Anderson and R. Madey, Nuclear Instruments and Methods  
161(1979)439.
- [Cla98] F. Clapier et al., Phys. Rev. Spec. Topics-AB, vol 1, 1998.
- [Cha62] G. Charpak et al., NIM 15(1962)323.
- [Den98] P. Dendooven et al., Workshop on Nuclear Fission and Fission-Product  
Spectroscopy, Seyssins, France, 1998 (AIP 447 Woodbury NY), p.135.
- [Des98] P. Desesquelles, Strasbourg, France, private communication, 1998.

- [Dup00] P. Van Duppen et al., *Hyperfine Interactions* 127(2000)401-408.
- [Dze72] B.S. Dzelepov et al., "Beta processes", 1972. Atom-Izdat, Moscow.
- [Dub99] Yu. E. Penionzkevich et al., "JINR Dubna Annual Report 1999".
- [Duk70] L. Duke et al., *Nucl. Phys. A* 151, 609 (1970).
- [Eng95] Ch. Engelmann et al., *Z. Phys. A* 352(1995)351.
- [Fog92] B. Fogelberg et al., *Nucl. Instr. Meth. B* 70, 137 (1992).
- [Fra77] H. Franz, K.-L. Kratz *et al.*, *Nucl. Inst. and Meth.* 144(1977)253-261.
- [Fuj64] K. Ikeda et al., *Phys. Lett.* 3, 271, 1963.
- [Gad92] E.Gadioli & P.Hodgston "Pre-equilibrium Nuclear Reactions", Clarendon press Oxford, 1992.
- [Gue76] A. Del Guerra, *Nucl. Inst. and Meth.* 135 (1976) 337.
- [Gui84] D. Guillemaud-Mueller, C. Detraz, M. Langevin and F. Naulin, *Nucl. Phys. A* 426 (1984) 37.
- [Ham01] Hamamatsu Photonics K.K., Electron Tube Center, Toyooka-village, Shimokanzo 314-5, Japan.
- [Han73] P.G. Hansen, "The beta strength function", *Adv. Nucl. Phys.* v. 7 (1973) 159.
- [Hil85] N.W. Hill, J.A. Harvey et al., *IEEE Trans. Nucl. Sci.* NS-32, 367 (1985).
- [Hil92] D. Hilscher et al., *Ann. Phys. Fr.* 17(1992)471.
- [Hof95] D.J Hoffman, B.B. Back, and P. Paul, *Phys. Rev. C* 51, 2597, 1995.
- [Huht97] M.Huhta et al., *Phys. Lett.* B405 (1997) 230.
- [Ibr00] F. Ibrahim et al., *IPN-Orsay Annual Report* 21(2000).
- [Ike63] J.I. Fujita et al., *Phys. Rev. B* 133,549, 1964.
- [Jam98] F. James, MINUIT-Reference Manual Version 94.1, CERN Program Library Long Writeup D506 1998., Geneva, Switzerland.
- [Jauh94] P.P. Jauho et al, *Phys. Rev. C* 49, 2036 (1994).
- [Kai97] Previously developed for LANCER; Kai Brinkmann, private communication.
- [Kar91] E. Karttunen et al., *Nucl. Sci. Engin.* 109,350 (1991).
- [Kra81] K.-L. Kratz et al., *Proc. of 4<sup>th</sup> Int. Conf. on Nuc. Far From Stab.*, CERN report 81-09 (1981) p. 17.
- [Kra82] K.-L.Kratz, et al., *Z. Phys. A*, 306,239-257(1982).
- [Kud97] M. Kudo et al., *Nucl. Instr. Meth.* B126(1997)209.
- [Kud98] H. Kudo et al., *Phys. Rev. C* **57**, 17 (1998).



- [Kuz94] A. V. Kuznetsov et al., Nucl. Instr. and Meth. A 345(1994) 259.
- [Lan84] M. Langevin, C. Detraz and D. Guillemaud-Mueller, Nucl. Phys. A 414 (1984) 151.
- [Lan98] LANL Group X-6 SuperLAB Project, Los Alamos National Laboratory 1998.
- [Leb98] L. Lebreton et al., SPIRAL Phase II: PARNe I at Louvain La Neuve, Rapport Annuel CYCLONE 1998, p.44.
- [Lis91] P.W. Lisowski et al., Proc. Specialist “ Meeting on Neutron cross sections for the Energy above 20 MeV”, Uppsala, Sweden (1991), OECD/NEA report NEANDC-305 ‘U’, p. 177.
- [Meh96] T. Mehren et al. Phys. Rev. Lett. 77 3(1996)458.
- [Meu75] J. P. Meulders et al., Phys. Med. Biol. 20 (1975) 235.
- [Mou94] S.Mouatassim, Contribution a la realisation du DEMON, etudes des performances par mesures et simulations, Ph. D. Thesis 1994., Stasbourg.
- [Mur82] M.J. Murphy, T.J.M. Symons, G.D. Westfall and H.J. Crawford, Phys. Rev. Lett. 49 (1982) 455.
- [Nol93] J. Nolen, Proceedings of the 3<sup>rd</sup> International Conference on Radioactive Nuclear Beams, East Lansing, Michigan, USA, May 24-27,1993., p. 111.
- [Nup00] The NuPECC Working Group on Radioactive Nuclear Beam Facilities (Europe, April 2000).
- [Num01] S. Nummela Thesis (2001) Jyväskylä, RR No.6/2001.
- [Numm01] Nummela et al., Phys. Rev. C 63(2001), 044316.
- [Ort93] H.-G. Ortlepp et al., Proc. of Int. School-Seminar on Heavy Ion Physics, Dubna, May 10-15, 1993, eds. Yu. Oganessian et al. (JINR Dubna, 1993), vol. 2, p. 466.
- [Pas71] V.V. Pashkevich, Nucl Phys. A 169 (1971) 275.
- [Pau00] N. Pauwels, PhD, Universite Paris.
- [Pent97] H. Penttila et al., Nucl. Instrum. and Meth. B126 (1997) 213.
- [Phi98] W.R. Philips et al., Eur. Phys. J.A3, 205 (1998).
- [Phi99] Photomultiplier tubes, PHILIPS Photonics 1999.
- [Pop99] A. Popov, Thesis (1999) UDK 593-172, St. Petersburg, Russia.
- [Rao72] S.A. Rao, Phys. Rev. C 5, 171 (1972).
- [Rao79] V.K. Raom et al., Phys. Rev. C19, 1372 (1979).
- [Rav89] H.L.Ravn and B. Allardyce, in *Treatise of Heavy-Ion Science* edited by

- D. Allan Bromley, Vol. 8 (Plenum Press, New York 1989), p. 363.
- [Rad98] Z. Radivojevic, Monte-Carlo Simulation of Neutron Registration by Complex Detection Systems, M.Sc. Thesis 1998., Jyväskylä, Finland.
- [Rad01] Z. Radivojevic et. al., "Numerical Simulation for unfolding of complex activities, in Proceedings of the XXXV annual conference of the Finn. Phys. Soc., March, Jyväskylä.
- [Rid99] D. Ridikas et. al., Phys. Rev. C 59, 1555 (1999).
- [Rub98] V.R. Rubchenya et al., Workshop on Nuclear Fission and Fission-Product Spectroscopy, Seyssins, France, 1998 (AIP 447 Woodbury NY), p.453.
- [Rub98] V.A. Rubchenya et al., Phys. Rev. C58, 1587 (1998).
- [Rub99] V.A. Rubchenya et al., Fission modes in  $^{238}\text{U} + d$  reaction at intermediate energy, 2nd Inter. Conf. on Fission and n-rich Nuclei, June 28 – July 2, 1999, St Andrews, Scotland.
- [Sal76] M.J. Saltmarsh et al., ORNL Report (1976) ORNL/TM-5696.
- [Ser47] R. Serber, Phys. Rev. vol 72, (1947) 1008.
- [Sch00] K.-H. Schmidt et al., Nuc. Phys. A 665(2000)221-267.
- [Sid89] J.L. Sida et al., Nucl. Phys. A502 (1989) 233c.
- [Sie93] R.H. Siemssen et al., Report on the European RNB facilities from the NuPECC study group, Munich, 1993, edited by G.E. Körner.
- [Sob83] I.M. Sobol "Izuchenie metodi Monte-Karlo" Moskva 1983.
- [Str68] V.M. Strutinsky et al., Nucl. Phys. A 122 (1968) 1.
- [Sze01] J. Szerypo et al., Acta Phys. Polonica, No3, Vol. 32 (2001) p. 985
- [Tak69] K. Takahashi et al., "Gross theory of nuclear beta decay", Prog. Theor. Phys. 41, 1470, 1969.
- [Tak72] K. Takahashi et al., Prog. Theor. Phys. 47, 1500, 1972.
- [Tak73] K. Takahashi et al., Nucl. Data Tables 12 (1973) 101.
- [Thi81] C. Thibault, et al., 4<sup>th</sup> International Conference on Nuclei Far From Stability, Helsingør 1981, CERN report 81-09 (1981) p. 365.
- [ToI98] Table of Isotopes, R.B. Firestone 1998. 8th edition.
- [Tök93] J. Töke et al., Nucl. Instr. and Meth. A 334(1993)653.
- [Tra72] B.L. Tracy et al., Phys. Rev. C 5, (1972) 222.
- [Trz95] W.H. Trzaska et al., Proc. of the 15<sup>th</sup> European Physical Society Conference, LEND-95, 17-23 April 1995, St. Petersburg, Russia, p.246.
- [Trz97] W.H. Trzaska, et al., Proc. of the XIV Int. Conference on the Application of

Accelerators in Research and Industry, Denton, Texas, November 6-9, 1996, AIP Conference Proc. 392, edited by J.L.Duggan and I.L.Morgan, AIP Press, New York 1997, page 1059.

- [Tse99] I. Tsekhanovich et al., Nucl. Phys. A 658 (1999) 217.
- [Vio85] V. E. Viola et al., Phys. Rev. C 31 (1985) 1550.
- [Viv00] F. Vives, F.J.Hambsch, H.Bax and S.Oberstedt Nucl.Phys. A **662**, 63 (2000).
- [Wah88] A.C. Wahl, At. Data Nucl. Tables, **9**, 1 (1988).
- [Wan99] J.C.Wang et al., accepted for publication in Phys. Lett. 1999.
- [Wap77] A.H.Wapstra and K.Bos, Atomic Data and Nuclear Data Tables, Vol. 19, No. 3, March 1977.
- [Wat79] F.M. Waterman et al., Med. Phys. 6 (1979) 432.
- [Wil76] D. Wilkins et al., Phys. Rev. C 14, 1832 (1976).
- [Yam65] M. Yamada, "Gross properties of nuclear beta decay", Bull Sci. Eng. res. Lab. Waseda Univ. Tokyo, No. 31/32, 146, 1956.
- [Zie81] W. Ziegert et al., 4<sup>th</sup> International Conference on nuclei far from stability, Helsingør 1981, CERN report 81-09 (1981) p. 327.
- [Zet66] H.-O. Zetterström, S. Schwarz and L.G. Strömberg, Nucl. Inst. and Meth. 42 (1966) 277.
- [Zöl95] C.M. Zöller, et al., "Fission Fragment Properties in the <sup>238</sup>U(n,f) Reaction at Incident Neutron Energies from 1 MeV to 500 MeV" in Proceedings of the Seminar on Fission Pont d'Oye III Castle of Pont d'Oye, Habay-la-Neuve, Belgium, 9-11 May 1995.
- [Zöll95] C.M. Zöller, PhD TU Darmstadt, Germany 1995.